UNDERSTANDING AND DEVELOPMENT OF COST-EFFECTIVE INDUSTRIAL ALUMINUM BACK SURFACE FIELD (Al-BSF) SILICON SOLAR CELLS

by

Nian Chen

A dissertation submitted to the faculty of
The University of North Carolina at Charlotte
in partial fulfillment of the requirements
for the degree of Doctor of Philosophy in
Electrical Engineering

Charlotte

2015

Approved by:

Dr. Abasifreke Ebong

Dr. Yong Zhang

Dr. Edward B Stokes

Dr. M.Yasin Raja

Dr. Tony Schmitz

ABSTRACT

NIAN CHEN. Understanding and development of cost-effective industrial aluminum back surface field (Al-BSF) silicon solar cells. (Under the direction of DR. ABASIFREKE EBONG)

For the long-term strategy of gradual decarbonization of the world's energy supply, high penetration of PV electricity is critical in the future world energy landscape. In order to achieve this, solar electricity with competitive cost to fossil fuel energy is necessary. To be able to obtain high efficiency solar cells, many advanced cell architectures have been developed commercially by PV industry. However, the fabrication of these cells necessitates complex processing steps and high requirements on semiconductor materials, which make it not as cost-effective as the state-of-the-art conventional Al-BSF structure. In order to keep the cost of PV cell low and improve on the efficiency with fewer processing steps, this thesis work focuses on the understanding of the conventional Al-BSF solar cell structure. The research work therefore, focuses on the (i) design, and modeling of front metal electrodes including the use of multi-busbar capable of decreasing the gridline resistance, (ii) fine-line printing and (iii) metal contact co-firing using high belt speed that is not common to the solar industry to achieve ~20% efficient industrial Al-BSF silicon solar cells.

In order to achieve the objectives of this thesis work, firstly, the appropriate Al paste was investigated for lowest back surface recombination velocity (BSRV), which gives high open-circuit voltage (V_{oc}). Secondly, the impact of emitter sheet resistance on solar cell performance was modeled to determine the optimal sheet resistance, and the uniformity of emitter was also investigated. Thirdly, modeling on the front metal electrodes

was carried out to investigate the optimal number of busbars, and determine the optimum number of gridlines and gridline geometries that would result in low series resistance (R_s), high fill factor (FF) and hence high efficiency. Fourthly, the modeled results were experimentally validated through fine-line printing and optimized contact co-firing. By combining each layer to make solar cells, V_{oc} of ~642 mV, J_{sc} of ~38.5 mA/cm^2 and FF of ~80.4% led to average ~19.8% efficient cell. Based on the experimental results, other innovative front grid designs are proposed that can lead to >20% energy conversion efficiency.

ACKNOWLEDGEMENTS

I would like to express my gratitude to a number of individuals who have supported me during my time at UNC Charlotte. First of all, I would like to thank my Ph.D. advisor, Dr. Abasifreke Ebong, who has contributed the most to my research and helped me develop critical thinking. He has not only provided me scientific resources to do high-quality research, but he also spent a great many hours with me for the writing of technical papers and the development of presentation and technical communication skills. Without encouragement and guidance from Dr. Abasifreke Ebong, I would not have made it this far in my doctoral degree.

I am also greatly indebted to Dr. Yong Zhang, Dr. Edward B. Stokes, and Dr. Yasin Raja who were willing to be my committee members and give constructive advices. And special thanks go to Dr. Michael A. Fiddy and Dr. Raphael Tsu for their intuitive teaching in class that motivated me to be an independent thinker. I also would like to thank Dr. Haitao Zhang and Dr. Lou for their helpful trainings on SEM and XRD. Furthermore, I would like to acknowledge the invaluable assistance that I have received from Keith Tate from Georgia Tech for the help with the modeling and IQE measurements, and Ernest Addo from PVCH for the Al work, and also Dr. Ben M. Damiani from xSi for the blue wafers. Additionally, I appreciate much the front Ag pastes from Dupont and Heraeus, and back Al paste from Monocrystal, and also the help from TP Solar for the equipment and maintenance.

I would like to give special thanks to my colleagues, Babar Hussain, Ahrar A. Chowdhury, Veysel Unsur and Yashwanth Ganti, who have been helping me with all the necessities that I need for my experiments and research throughout the years.

Among my friends, Wattaka Sitaputra, Lun Peng, Xun Li and Meng Jia have provided me with joy and support for enrichment of my life during my stay in United States.

I would like to acknowledge the financial, academic and technical support from the graduate school of UNC Charlotte, and also all the members in the Department of Computer and Electrical Engineering. I am especially thankful to the Graduate Coordinator, Dr. Bharat Joshi, Ms. Stephanie LaClair and Ms. Jerri Price, and Mr. Eddie Hill and Mr. Alec Martin for their countless assistances in administrative issues and equipment issues, respectively.

Finally, I am grateful with deepest gratitude to my family in China, as well as my wife and my cousins in United States for their moral support and their constant encouragement through my academic and professional endeavors. And special thanks go to my host family, Lanier and Karen Ellis, for giving me their unyielding love and support for my life in Charlotte, North Carolina.

TABLE OF CONTENTS

LIST OF ABBREVIATIONS

2D	two-dimensional
3-BB	3-busbar
4-BB	4-busbar
5-BB	5-busbar
Ag	silver
Al	aluminum
ARC	antireflection coating
a-Si	amorphous silicon
BBR	busbar to busbar resistance
BOS	balance of system
BSF	back surface field
BSRV	back surface recombination velocity
CdTe	cadmium telluride
CIGS	copper indium gallium selenide
CO_2	carbon dioxide
¢/W	cent per wattage
c-Si	crystalline silicon
CZ	Czochralski
DP	double-printing
EL	electroluminescence
EQE	external quantum efficiency

EWT	emitter wrap through
FBR	front busbar resistance
FF	fill factor
FSF	front surface filed
FSRV	front surface recombination velocity
FZ	float-zone
HIT	heterojunction with intrinsic thin-layer
IBC	interdigitated back contact
IPM	inch per minute
IQE	internal quantum efficiencies
ITO	indium tin oxide
J_L	light-generated current density
J_{o1}	saturation current density
J_{o2}	junction reverse saturation current density
J_{ob}	base saturation current density
J_{oe}	emitter saturation current density
J_{sc}	short-circuit current density
LCOE	levelized cost of electricity
LID	light-induced degradation
LIV	light current voltage
LPS	liquid phase sintering
MIS	metal insulator semiconductor
MWT	metal wrap through

PC1D	Computer program for one dimensional modeling
PC2D	Excel-based computer program for two dimensional modeling
PECVD	Plasma-enhanced chemical vapor deposition
PERC	passivated emitter and rear cell
PERL	passivated emitter with rear locally diffused
PSG	phosphosilicate glass
R_s	series resistance
SEM	scanning electron microscopy
SiN_x	silicon nitride
SiO_2	silicon dioxide
SP	single-printing
SRV	surface recombination velocity
STC	standard test condition
TBW	total busbar width
TCO	transparent conductive oxide
V_{oc}	open-circuit voltage

CHAPTER 1: INDUSTRIAL SILICON SOLAR CELLS – A REVIEW

1.1 Introduction

Photovoltaics (PV), the "carbon-free" clean technology that directly converts solar energy into electricity without generating any polluting byproduct, has grown dramatically in recent years due to the increasingly growing residential and commercial markets. PV cells of single-junction can be categorized as wafer-based, thin films, and emerging technologies, as shown in Figure 1.1.

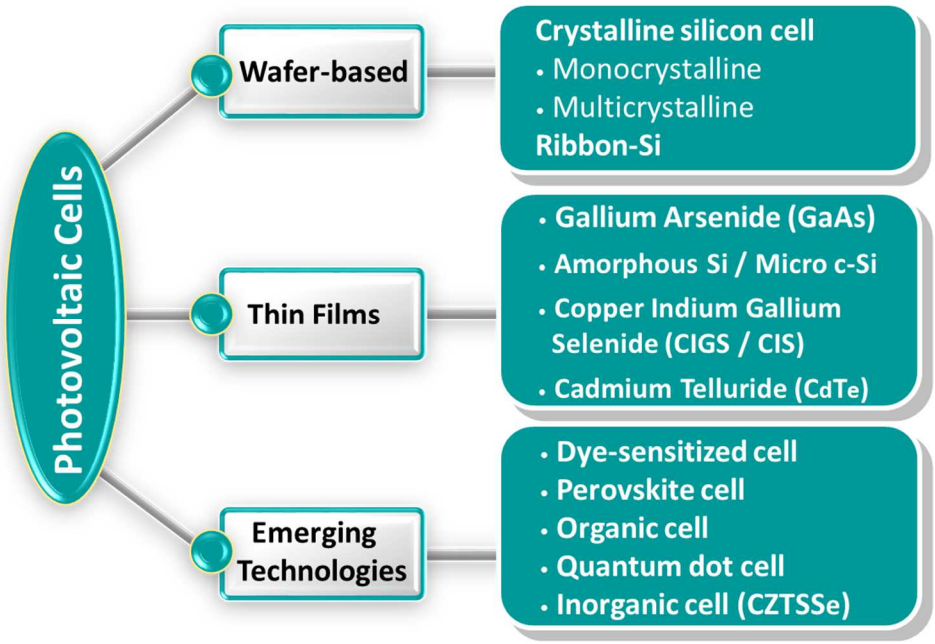

Figure 1.1: Different types of photovoltaic cells based on various technologies.

Wafer-based silicon technologies have been the workhorse of the PV industry for decades. There are two types of wafer-based solar cells in commercial high-volume

production; namely monocrystalline and multicrystalline silicon. Thin film solar cells including a-Si, CIGS and CdTe are also strong contenders. It is worth mentioning that some emerging technologies, such as dye-sensitized, perovskite and organic cells, are playing an increasingly important role in converting sunlight directly into electricity.

These are reviewed in this chapter to set the stage for my thesis work, which mainly focuses on crystalline Si because of its simplicity, reliability, high-throughput and cost-effectiveness.

1.1.1 Solar Cell Structure and Operation Principle

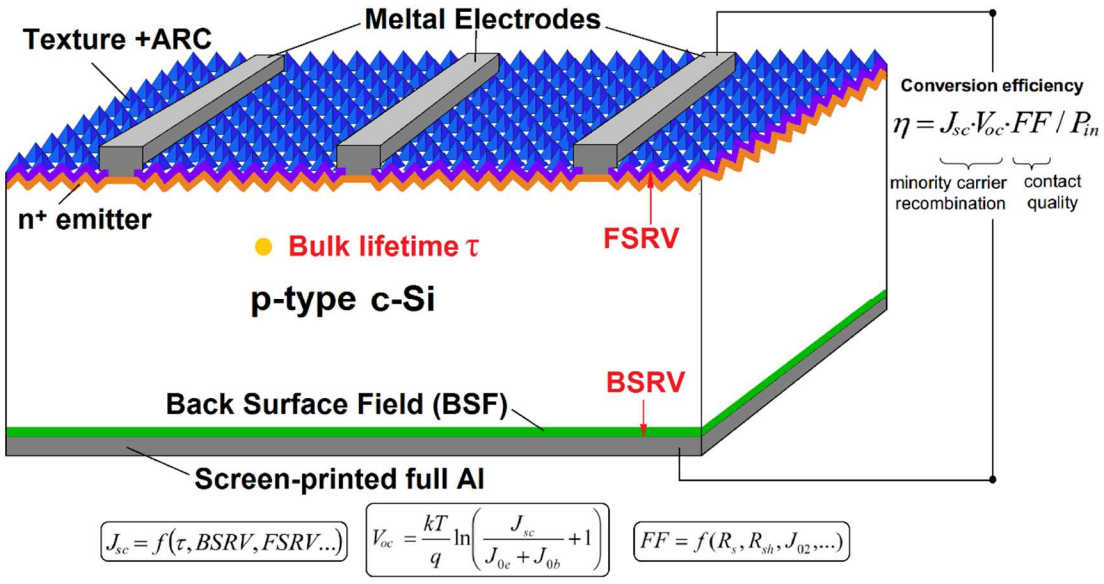

Figure 1.2: Different types of photovoltaic cells based on various technologies and materials.

A typical crystalline solar cell architecture consists of a p-type substrate with n and p metal contacts at the front and backside as shown in Figure 1.2. The internal structure of a solar cell has a p-n junction formed between the n-doped emitter of 0.2-2 μm thick and the p-doped substrate of ~180 μm thick. The front surface is textured and coated with an antireflection coating (ARC) layer to enhance the light absorption. The ARC also provides

passivation to the front side to decrease front surface recombination velocity (FSRV). The back surface field (BSF) formed by the Al alloyed with the substrate reduces recombination at the back side and improves the open-circuit voltage (V_{oc}). Under illumination, electron-hole pairs are first created in the absorber by the absorption of incident photons, which transfer their energy to loose electrons, smashing them off Si atoms. Then electrons as minority carriers diffuse to the space charge region and sweep across the junction by the electric field at the depletion region to reach the n-type emitter, where they become majority carriers. The photo-generated current then can flow through the external circuit if the front and rear metal electrodes are connected together. The parameters very critical to a solar cell are short-circuit current (J_{sc}), V_{oc} and fill factor (FF). And the efficiency of a solar cell is limited by several factors as outlined in the next section.

1.1.2 Factors Affecting the Performance of a Solar Cell

Efficiency is the key metric for a solar cell. It is the product of three parameters, J_{sc}, V_{oc} and FF. Figure 1.3 shows the relationship of how these three parameters interact, the understanding of which is crucial to manufacturing low-cost and high efficiency solar cell. The fabrication of a solar cell starts with the silicon wafer with resistivity range from 0.6-2.6 Ω·cm that influences the bulk resistance, which is one of the six components of the series resistance (R_s). Because of the light induced degradation observed in Czochralski (CZ) silicon, the resistivity of choice is ~2.6 Ω·cm. Therefore, the bulk resistance in most industrial crystalline cell is ~2.6 Ω·cm, and the impact on FF and V_{oc} is fixed. Front surface texturing is the next step, which impacts the front surface reflectance, ARC and the width of the front gridlines. If texturing is not uniform, the front gridlines can be very wide in some region [1] and adds to the total metal shadowing and decrease J_{sc} and V_{oc}. The V_{oc} is

impacted because the emitter dark saturation current density (J_{oe}) underneath the wider gridlines is higher than the narrower gridline counterparts.

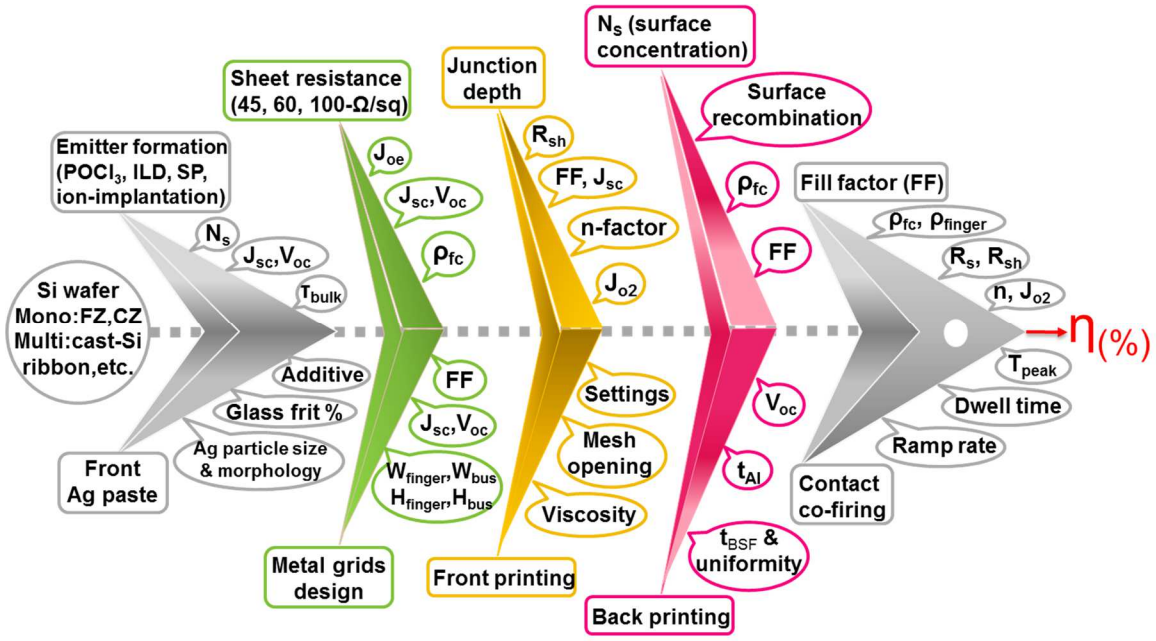

Figure 1.3: Relationship between various factors affecting the efficiency of a commercial solar cell [2].

After texturing, the p-n junction is formed, which involves the diffusion of either phosphorus (p-type substrate) or boron (n-type substrate) into the textured substrates to some depth. The antireflection coating also influences the photon absorption in the layer and bulk. The thickness must be properly designed to avoid absorption in the ARC, which does not contribute to current collection. From Figure 1.3, the emitter formation is linked to sheet resistance, junction depth, surface concentration (N_s), which in turn influence J_{sc}, V_{oc} and the FF. On the other hand, the front Ag and back Al inks, front gridline printing, back Al printing and co-firing (ramp-up and ramp-down rates) can also affect the three parameters. For the commercial solar cell, FF is the most affected of the three parameters, because of the simplicity of the process which require the printed contacts to fire through

the front dielectrics (ARC). Even if the gridlines are narrow, uniform etching of the underlying dielectric is necessary for low contact resistance and the overall R_s to obtain high FF.

1.2 Commercial Crystalline Silicon Solar Cell Technologies

Crystalline silicon solar cell structures include the following: (i) full Al-BSF; (ii) PERC; (iii) EWT; (iv) MWT; (v) IBC; (vi) HIT; (vii) Triex cell; (viii) Pluto cell. In this section, the processing steps for each of the structures would be reviewed along with the performance. This will set a stage for the motivation for this thesis work.

1.2.1 The Full Al-BSF Cell (Conventional Silicon Solar Cell)

The conventional commercialized solar cell structure is mainly characterized by p-type mono-/multi-crystalline silicon wafer, front-side SiN_x passivation/ARC, screen-printed front and rear metal grid, and full aluminum back surface field (Al-BSF). This state-of-the-art structure, which is the focus of this research, is still widely used by many PV manufacturers due to its cost-effective fabrication process.

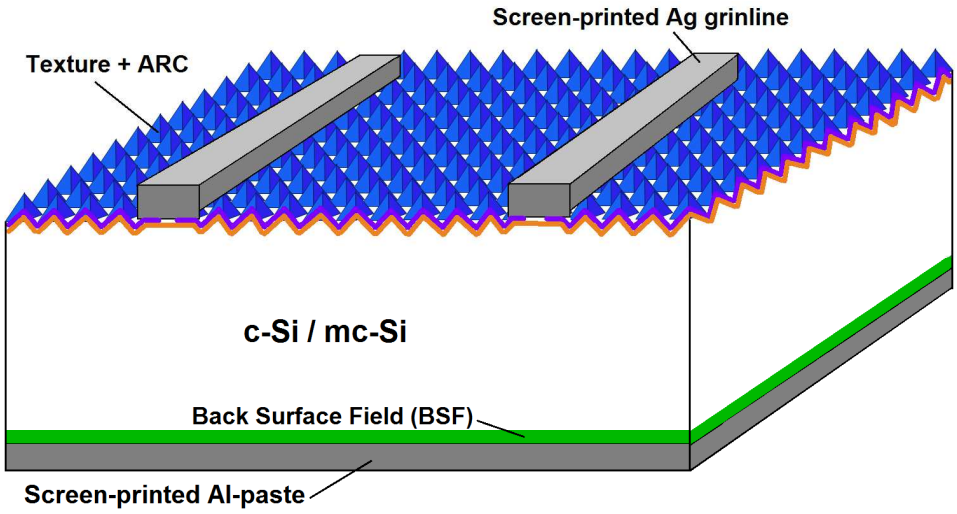

Figure 1.4: A schematic structure for conventional solar cell with full Al-BSF and screen-printed “H” pattern metal grid.

A schematic architecture of the Al-BSF cell, generally known as the H-pattern, is shown in Figure 1.4. The normal cell-processing sequence consists of (i) saw damage removal, chemical texturing and cleaning; (ii) phosphorus diffusion; (iii) phosphorus glass (PSG) removal and edge isolation; (iv) silicon nitride (SiN_x) deposition for front surface AR-coating; (v) front Ag paste screen-printing and drying; (vi) rear Al/Ag screen-printing and drying; (vii) co-firing of screen-printed metal electrodes; (viii) cell light current voltage (LIV) testing and sorting.

A typical industrial Al-BSF cell has V_{oc} in the range of 620-650 mV, J_{sc} in the range of 35-39 mA/cm^2 and FF in the range of 0.76-0.80, which result in cell conversion efficiency of 16-20%. For screen-printed Al-BSF cell with busbar of 1.5 mm width, and gridline of 70-120 μm width with ~2 mm line spacing, the metal shadowing by the front metallization is about 5-8%, and R_s is about 0.6-1.0 Ω·cm^2. The main disadvantages of screen-printed solar cell relates to the front metal shadowing, the high R_s and surface recombination. The concentration in this work is the improving of front metallization by fine-line printing and multi-busbar concept, and the optimization of the firing process to obtain uniform BSF to decrease the back surface recombination velocity (BSRV).

1.2.2 The PERC Cell

The PERC (passivated emitter and rear cell) cell was the first solar cell structure to exceed 20% conversion efficiency under standard test conditions (STC) [3]. Compared with the screen-printed Al-BSF counterpart, the main differences in cell architecture arises at the rear side. The PERC cell uses a thermal SiO_2 layer to electronically passivate most of the rear cell surface, and point-contact is made through holes in the passivating oxide

layer to the low resistivity p-type substrate. A highly reflective planar rear surface (>97%) is also incorporated to strengthen the light-trapping within the cell [4].

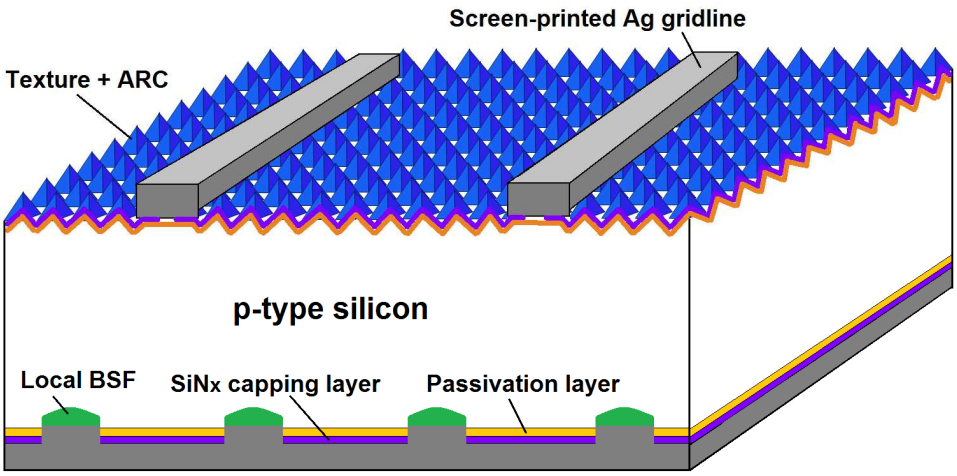

Figure 1.5: Schematic diagram of PERC solar cell.

A schematic diagram of the PERC solar cell is shown in Figure 1.5. The rear surface is passivated by a thin oxide layer. And SiN_x capping layer is stacked with oxide layer to enhance its thermal and radiation stability in fabrication and operation.

1.2.3 The EWT Cell

The initial idea of emitter wrap through (EWT) solar cell came from the Polka Dot solar cell, which has the photo-generated current being collected by both front and rear junctions that are connected in parallel by a multiplicity of small-area interconnect paths [5]. The concept of EWT cell for a back-contact cell was first proposed by James M. Gee et al. in 1993 [6]. The architecture of a typical EWT solar cell is shown in Figure 1.6. It has n-type region defined for the emitter on the rear side interdigitating with p-type region for the base contact. The interconnection of both front-side and rear-side emitters is achieved by laser-drilled holes that have heavy phosphorus diffusion. The screen-printed glass or dielectrics as diffusion barriers have been applied to the base to locally block the

diffusion of phosphorus for the separation of n- and p-type metallization regions on the rear side [7].

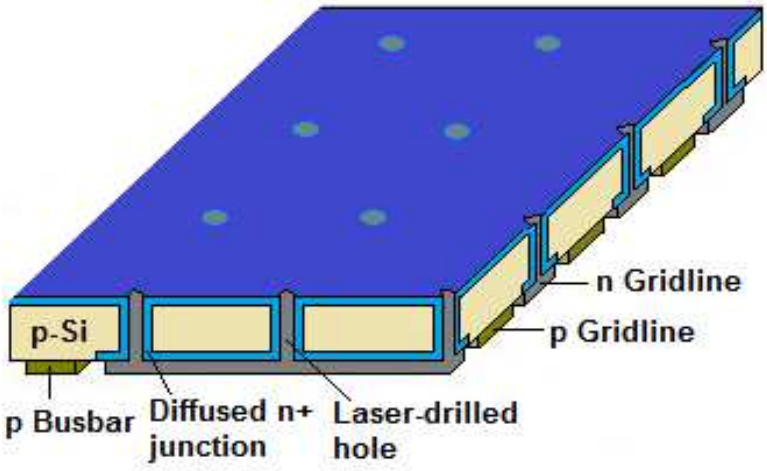

Figure 1.6: Schematic diagram of EWT solar cell.

Compared with conventional Si solar cells, EWT cells can provide enhanced collection of photo-generated carriers with thinner wafers of lower bulk lifetime because of the elimination of the front metal coverage and double-sided collection of current from the bulk, which favors the industrial processing of EWT cells with lower grade mono- and multi-crystalline silicon for low-cost production. In production, median and best efficiency of 18.7% and19.2%, with FF of 0.757 and 0.766, respectively, have been achieved with 239 cm^2 monocrystalline silicon wafers [8]. The main disadvantage of EWT technology is relatively low FF on industrial size cells, which is due to the high R_s in the laser holes connecting the front and rear sides. This leads to the development of metal wrap through (MWT) cells.

1.2.4 The MWT Cell

The metal wrap through (MWT) solar cell is an alternative approach for rear contact cell. Optimized interconnection by metal filling through the via-holes is critical to obtain

low R_s and good fill factor [9]. Compared to the EWT cell, the MWT technology requires a relatively lower density of via-holes to direct the photo-generated carriers to the rear surface through metal electrodes and n-doped emitters, while the EWT cells need a large number of densely spaced via-holes (some tens per 1 cm^2) to direct the photo-generated carriers to the rear only through n-doped emitters [10-11].

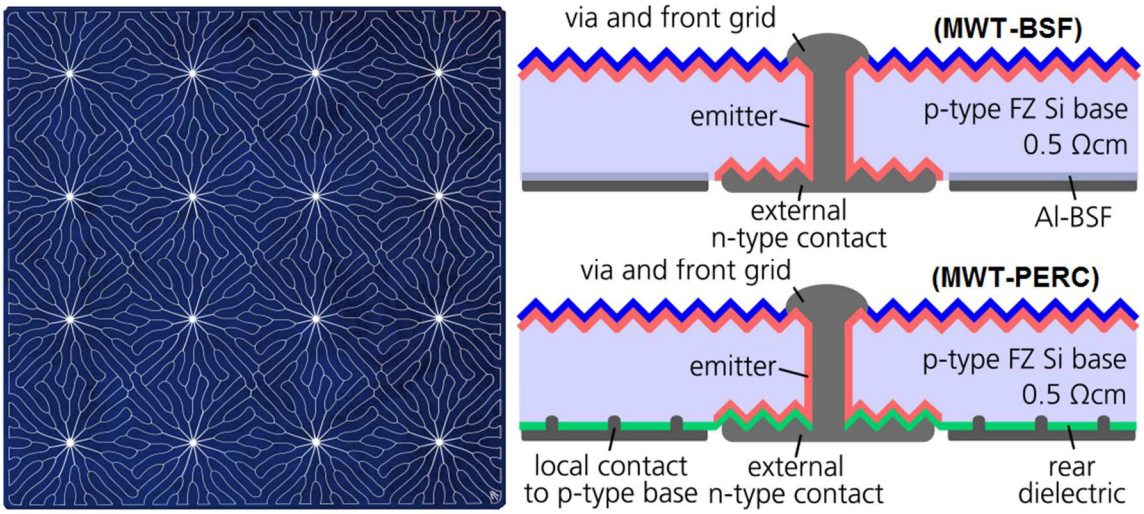

Figure 1.7: MWT technology with unique metallization pattern on the front side (Solland's Sunweb Technology).

The MWT cell structure is shown on the right of Figure 1.7. Unlike the EWT cells, it has metallization grid on both surfaces. The top grid pattern connects via holes in the cell to the rear contact with appropriate polarity. Compared to the conventional "H" grid pattern cells, the current gain of MWT cell is higher due to the elimination of metal busbars. To further enhance solar cell performance, the MWT technology can also be implemented with the PERC technology to make the MWT-PERC (Metal wrap through passivated emitter and rear cell) cells, which have proven to further increase the efficiencies of MWT-BSF (MWT cell with BSF rear side) cells to over 20% [12-13].

1.2.5 The IBC Cell

The IBC (interdigitated back contact) cell was originally developed by Dr. Swanson together with NASA in 1973. First designs of IBC cells were investigated by Lammert and Schwartz [14]. Afterwards, Sun Power Corporation (San Jose, CA; started operation in 1990) took advantage of the design concept, and redefined the world's standard for industrial high-efficiency solar cells by the Gen-series cells with its revolutionary Maxeon^{TM} solar cell technology.

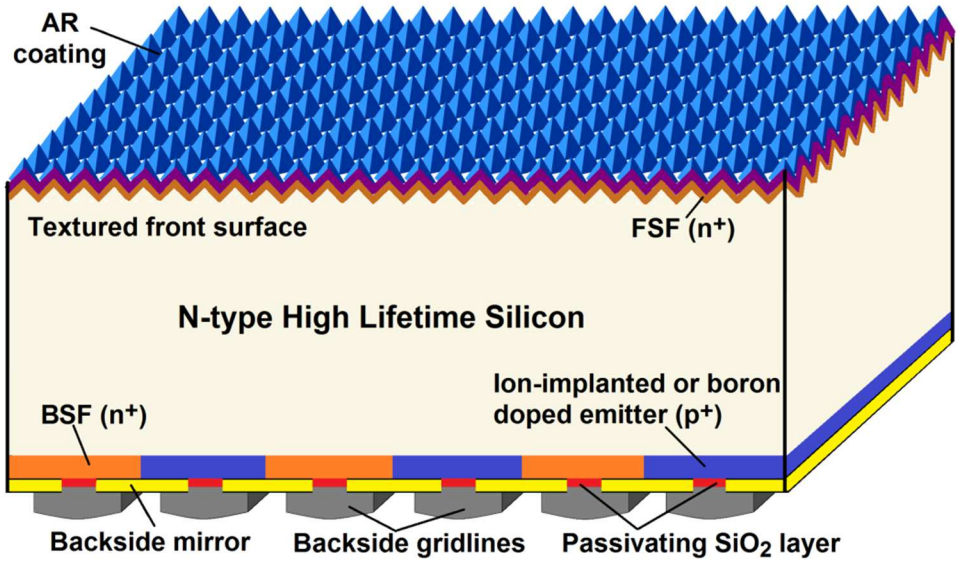

Figure 1.8: Schematic of the SunPower Generation 3 solar cell.

Sun Power's IBC cell architecture is schematically depicted in Figure 1.8. The advanced design concept brings low recombination, high generation and low parasitics to the cell due to [14-16]: (i) Zero grid obscuration on the front side that brings substantial enhancement in J_{sc}; (ii) Significantly reduced surface recombination with dielectrics and metal contact due to BSF and lightly doped front surface field (FSF), as well as passivating SiO_2 layer underneath rear n- and p-type metal contacts; (iii) Reduced resistive loss with high localized metal coverage and point arrangement of p/n-junctions; (iv) Good internal

optics due to enhanced back light reflection by backside mirror [17]; (v) N-type monocrystalline Si with high minority carrier lifetime ($\tau_{bulk} > 2$ ms is required for front $J_o < 10$ fAcm^{-2}) [18].

With advanced back-contact cell technologies, Sun Power has been the leader in commercialized cell and module efficiencies since early in the first decade of this century (see Figure 1.12 and 1.13). The company has been achieving consistent improvement in cell efficiency and also translating the gains in module efficiency. The generation 3 cells currently in high-volume production reached record high efficiency of 24.2% in 2010 [18] and average efficiency of 23.6% was achieved in 2012 [19].

1.2.6 The HIT Cell

Based on experience with hydrogenated amorphous silicon as passivation films and corresponding junction fabrication process for solar cells, Sanyo firstly developed the a-Si/c-Si heterojunction structure — HIT (heterojunction with intrinsic thin-layer) early in 1990s, which features a very thin intrinsic a-Si layer inserted between p-type a-Si and n-type c-Si [20-22]. In 2014, Panasonic (merged Sanyo in 2009) reached a new world record efficiency of 25.6% using HIT structure of practical cell size at 101.8 cm^2 and 98 um thickness from its former announced record of 23.7%, extremely high V_{oc} and fill factor (FF) of 750 mV and 0.832 were achieved, respectively [23].

A schematic structure of the HIT cell is demonstrated in Figure 1.9. The cell composes of a textured n-type c-Si wafer sandwiched between intrinsic a-Si (i-type a-Si) thin films. On the illumination side, p-type a-Si layer was grown on top of i-type a-Si to form a p-n junction, while on the rear side n-type a-Si layer was deposited to form a BSF. Transparent conductive oxide (TCO) layers, which are usually made of indium tin oxide

(ITO) [21], were also applied to both sides of the doped a-Si layers, followed by metal electrode formation for current collection. The most distinctive characteristic of the HIT solar cell includes: (i) excellent surface passivation of c-Si surfaces (SRV <10 cm/s) by the deposition of thin high quality i-type a-Si layers [20-21], which also brings reduction of interface trap density (D_{it}) by terminating the dangling bonds at the hetero-interface and hence increase of minority carrier lifetime [24]; (ii) good ohmic contact formed between grid electrode and silicon due to the high transparent TCO layer, which has high mobility to maintain sufficiently high conductivity and enable good spectrum response at the long-wavelength region [25]; (iii) the use of n-type CZ c-Si with its high minority carrier lifetime with good stability when exposed to sun light [26].

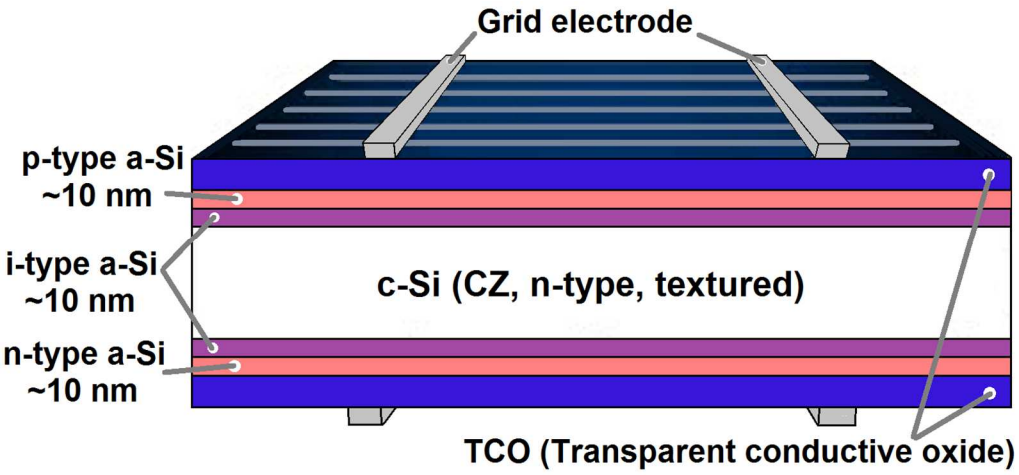

Figure 1.9: Schematic diagram of the HIT Solar Cell (Sanyo Electric).

The fabrication of HIT cells can be completed under low-temperature processes (< 200°C), which favors the industrial production to bring down the processing cost by saving thermal budget. The symmetrical HIT architecture and its low temperature processing reduce both thermal and mechanical stress within the device during fabrication processes, which is beneficial for the implementation of thin (<100 μm) wafers. The reduced

temperature coefficient (-0.33%/°C for conventional HIT cells [27] and -0.25%/°C for HIT cells made with new process [28]) is beneficial for high performance at high temperature.

1.2.7 The Triex Cell

The design concept of the Triex cell evolved from the experimental work with silicon metal insulator semiconductor (MIS) solar cells carried out by two distinguished scientists, M.A. Green and R.B. Godfrey, from UNSW in the late 1970s, which encompasses thin oxide tunneling layer (10-15 Å) coupled with an inversion layer and rear collecting junction in the cell architecture [29-30]. The Triex cell uses hybrid technology that combines the elements of conventional c-Si solar cells and elements of thin film solar cells. The technologies of Triex solar cell were developed with the growth of Silevo (Fremont, California; founded in 2007 and acquired by Solar City in 2014), who firstly commercialized the Triex cell, also known as the 'tunneling junction' solar cell. Early in 2012, high conversion efficiency of 22.1% had been achieved by Silevo for a 145 cm^2 solar cell using Silevo's complete cell pilot line [31].

Silevo's proprietary technologies to achieve high efficiency couples the best attributes of three different materials – n-type c-Si substrate, thin a-Si film for passivation and semiconductor oxide for optimal cell and module performance – which enable the tunneling junction cells to achieve high conversion efficiency (> 21%) and higher energy harvest with competitive cost compared with today's c-Si PV leaders [32].

A schematic architecture of Silevo's tunneling junction solar cell is shown in Figure 1.10. The hybrid architecture of Silevo's Triex^{TM} device is distinctly characterized by (i) copper-based metal electrodes to enhance performance and cost reduction by elimination of expensive silver, (ii) TCO current collector to allow wider gridline pitch, (iii) thin a-Si

passivation films and oxide tunneling layers to enable high V_{oc} and provide excellent junction quality for extremely low SRV, (iv) n-type CZ c-Si for high minority carrier lifetime and elimination of light-induced degradation (LID). The tunneling oxide interface layer is also beneficial for excellent world class temperature coefficient (-0.22%/°C), which would result in 5-12% additional power generation in arid climates [32].

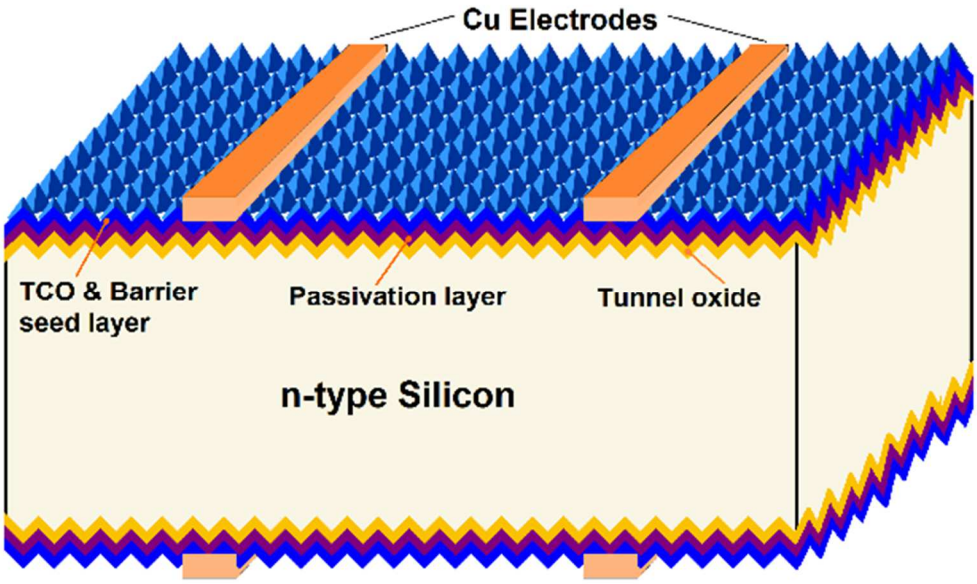

Figure 1.10: Schematic of the Silevo's tunneling junction solar cell (Triex^{TM} device).

1.2.8 The Pluto Cell

The Pluto cell architecture is based on the PERL cell design concept developed at UNSW, where the world record efficiency of 25% was achieved on a 4 cm^2 FZ p-type silicon wafer [33]. With several years of intensive joint research and technical exchange with UNSW, Suntech (Wuxi, China; found in 2001) commercialized the Pluto cell in 2009. Compared with the conventional screen-printed cell, the Pluto cell showed 1.2% increase in efficiency and particularly 2.2 mA/cm^2 increase in J_{sc} due to its advanced metallization scheme [34]. A schematic structure of the Pluto cell is shown in Figure 1.11.

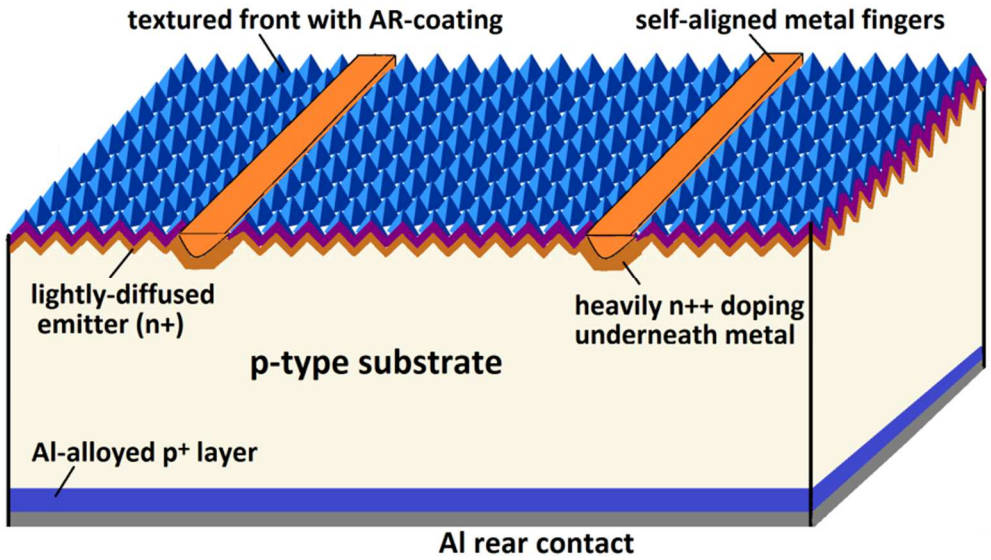

Figure 1.11: Schematic structure of the first-generation Pluto solar cell (Suntech). The next generation Pluto cell replaced full Al rear contact with localized rear contacts.

As the technology converted from the PERL cell, the Pluto^{TM} technology has made several cost improvements to enable the industrial feasibility of the Pluto cell. These improvements includes: (i) Substitute FZ silicon wafer with solar grade p-type CZ wafer; (ii) Use single-layer antireflection-coating (SLAR) (SiN_x) instead of double-layer antireflection-coating (DLAR) (SiO_2/ZnS/MgF); (iii) Replace photolithographic texturing with industrial texturing process; (iv) Replace the expensive and complex metal electrode formation process using thermal evaporation with self-aligned metallization using electroless nickel and copper plating. Compared with standard cells, the unique features of the Pluto^{TM} technology encompasses high-sheet resistance, selective emitter and ultra-narrow metal gridlines with a line width of 25-30 μm, which bring the Pluto cell enhanced J_{sc} and higher efficiency due to improved short wavelength spectral response, decreased metal coverage and contact resistance [35]. In addition, the Pluto cells are contacted with copper rather than printed silver paste, which drives down the metallization cost.

1.3 Efficiencies of PV by Technologies

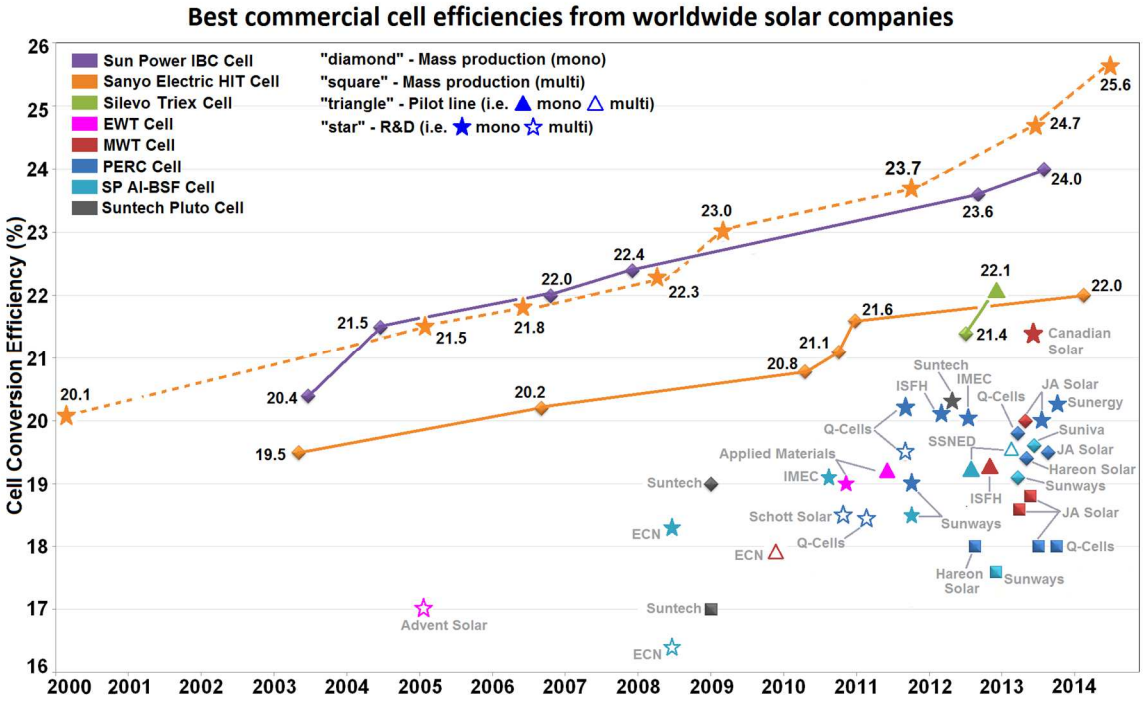

Figure 1.12: Evolution of PV penetration and total PV installed capacity from 2005 to 2013.

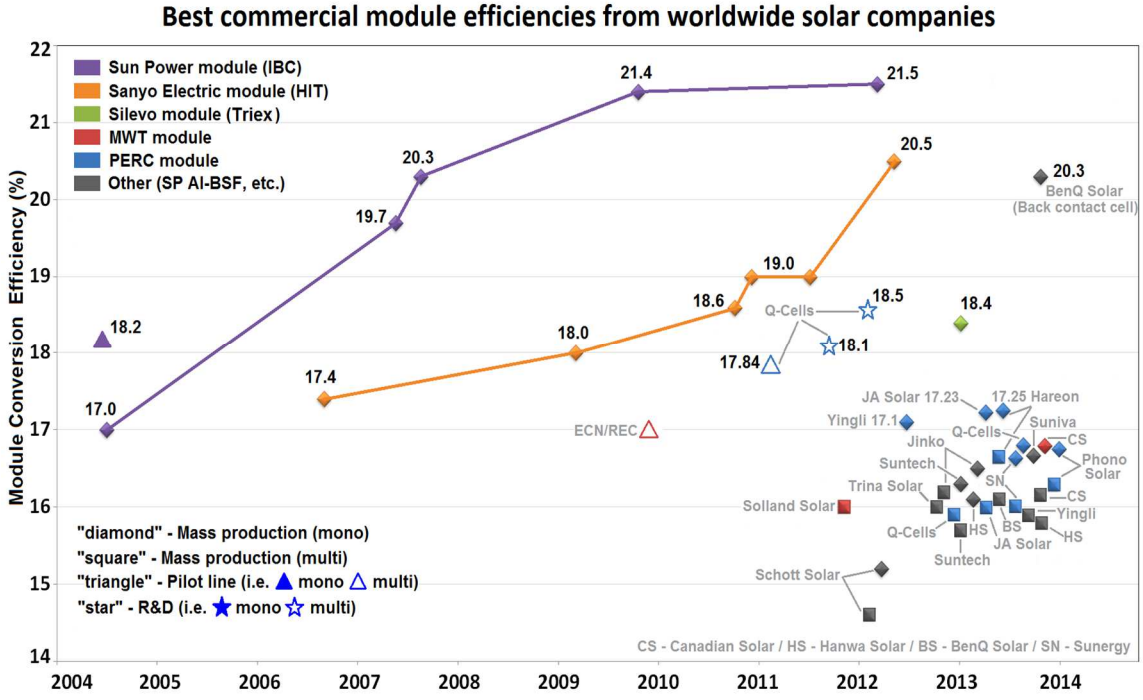

Figure 1.13: Evolution of PV penetration and total PV installed capacity from 2005 to 2013.

Figure 1.12 and Figure 1.13 demonstrate the best commercial cell and module efficiencies achieved by competitive solar manufacturers in the worldwide PV arena. It is shown that most of the manufacturers are differentiated by the technologies they use, and the cell conversion efficiency they have achieved. At cell and module level, Sun Power and Sanyo have been the major competitors in terms of efficiency with their advanced cell structures, IBC and HIT, respectively. It is worth mentioning that by 2013, high median efficiencies of 23.6% (best cells over 24%) and 21.7% had been achieved by Sun Power at cell and module levels, respectively, from its production lines [19], which strengthened Sun Power's dominance in high-efficiency PV technologies over other solar manufacturers. And at cell level, Panasonic (merged Sanyo in 2009) had achieved astonishing high efficiency of 25.6% with their heterojunction cell architecture in 2014 [23]. However, the annual shipment of PV modules are still dominated by the relative lower cost PV technologies such as MWT, PERC and Al-BSF cells, etc. Particularly, the Al-BSF cell, as the concentrated technology in this work, is still popular with a lot of PV manufacturers in the world due to its cost-effectiveness and the simplicity in processing, although the conversion efficiency of this technology is lower than the more advanced counterparts.

1.4 Commercial Status of Photovoltaic

Bell Labs announced the invention of the first modern silicon solar cell in 1954 [36]. Since then Hoffman Electronics firstly commercialized silicon solar cells with efficiencies up to 10% in the 1950s [37]. From the 1950s onwards, the rapidly expanding photovoltaic industry has been dominated by mono- and multi-crystalline silicon solar cells, particularly in the last 30 years due to the maturity of microelectronics industry. Although the dominance is now being challenged by thin films technologies with decreasing market

share, it still represents more than 90% of the global PV market capacity and production capacity in 2014, as shown in Figure 1.14 [38]. And the predominance of c-Si technology is expected to maintain its market share above 80% in the next ten years because of (i) the maturity of the technology developed from microelectronics industry, (ii) the rise of PV industries in Asia-Pacific region (e.g. China, Japan, Korea and Australia, etc.) that favor silicon wafer-based technologies, and (iii) the safety of silicon and the abundance of silicon resources on earth.

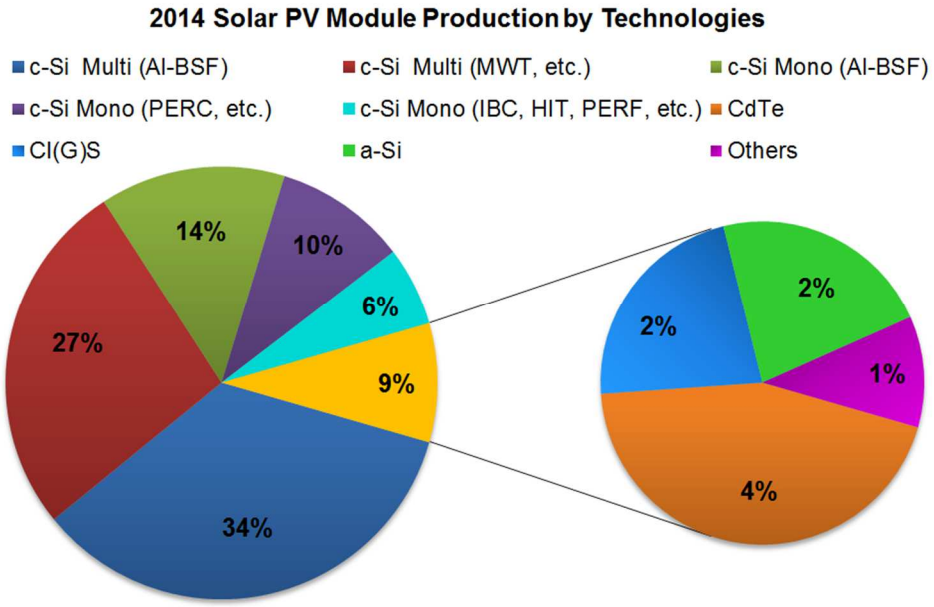

Figure 1.14: PV module production capacity share based on technologies in 2014 [38].

In 2013, the world's cumulative installed PV capacity had reached 138.9 GW, which means at least 160 TWh of solar electricity can be generated by PV every year. And this represents about 0.8% of electricity demand and roughly 1.6% of peak power demand globally [39]. The last decade has seen a continuous average annual growth of more than 40% for the world PV penetration, as shown in Figure 1.15 [39]. However, to be able to reshape the world energy landscape in the next few decades with solar electricity taking

the leading role in the energy supply, the technological advancement and cost-effectiveness of PV production still need to be further pursued. And compared with fossil fuel energy resources, the competitiveness of solar electricity will determine if the wide-spread impact of PV will happen in the days yet to come.

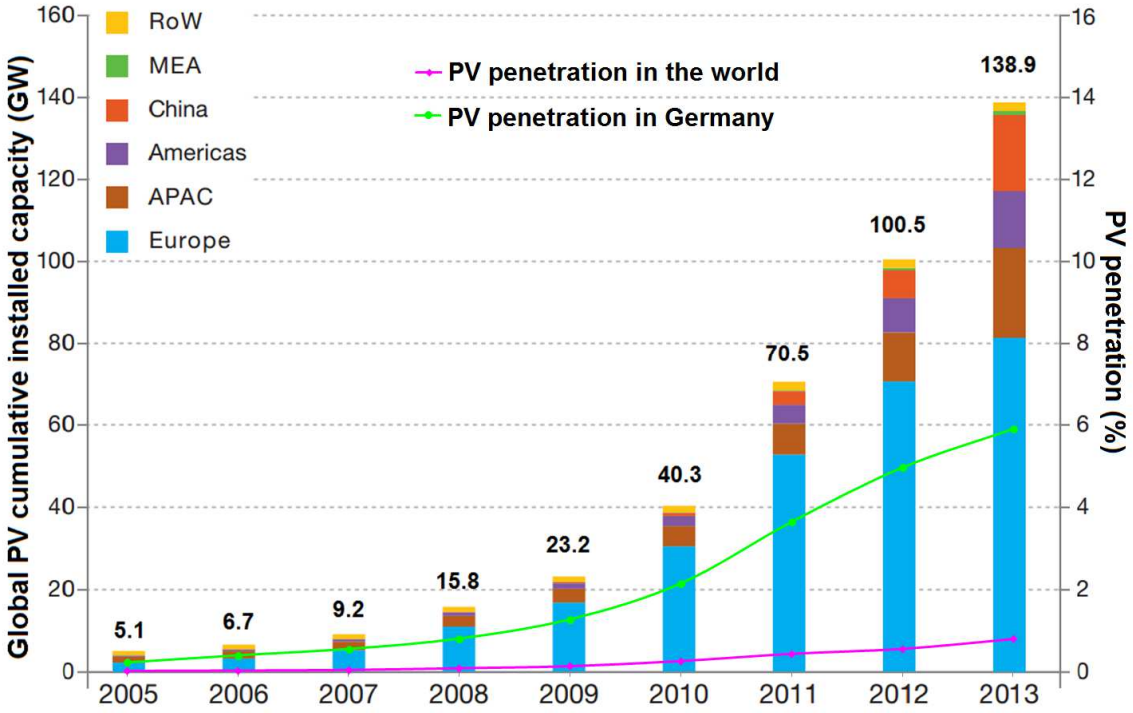

Figure 1.15: Evolution of PV penetration and PV installed capacity, 2005-2013 [39].

1.5 Statement of the Problem and Motivation

As the title of this thesis----"Understanding and Development of Cost-effective Industrial Aluminum Back Surface Field Silicon Solar Cells"----indicates, my work will address the solar cell device, which converts solar energy into electricity without any polluting byproduct in a cost-effective fashion with improved energy conversion efficiency. This will be done through (i) design, (ii) modeling, (iii) characterization, (iv) fabrication and (v) analysis of the commercial technologies and processes.

According to the fifth IPCC-Report [40], carbon dioxide (CO_2) is the most important anthropogenic greenhouse gas produced by combustion of fossil fuel. Emission of CO_2 from fossil fuel combustion and industrial process contributed about 78% of the total greenhouse gas emission increase from 1970 to 2010, with larger absolute increases from 2000 to 2010. For the long-term strategy of gradual decarbonization of the world's energy supply, high penetration of PV electricity in both residential and commercial applications with competitive cost will be required in the future world energy landscape. This is why the understanding and development of cost-effective PV cells is very critical to sustain solar electricity.

Critical aspects for the dissemination of PV include the market price ($\$/W_p$) for solar module and levelized cost of electricity (LCOE) from solar systems. To render solar technologies economically competitive, module price $<\$1/W_p$ and LCOE <10 ¢/kWh are required to achieve grid parity [41-42]. The challenges to obtain commercial cost-effective solar electricity includes (i) manufacture of high-quality large area crystalline silicon wafers at low cost; (ii) further reduction of wafer thickness without negative impact on solar cell conversion efficiency; (iii) reducing the weight of silver pastes printed per cell or replacing silver pastes with other contacting materials without losing efficiency and stability; (iv) implementation of simple and low-cost processing in conjunction with advanced cell architectures to achieve high efficiency (≥22%) [2].

Today, manufacture cost of PV panel can be broken down into ~40% for silicon, ~25% for solar cell processing, and ~35% for making solar modules [43]. The highest impact on the reduction of PV manufacturing costs is achieved by improving the conversion efficiency of solar cells. The technological development of the processing of

silicon solar cells enables manufacturing more advanced and highly-efficient (≥22%) cells. In industrial mass production of the solar cells for one-sun application, IBC cell of ~24% has been achieved by Sun Power [19] by using back contact back junction design concept in the cell architecture, and HIT cell of ~22% has been achieved by Panasonic [44] by implementing heterojunction cell structure. However since these cell designs are complex, their fabrication are challenging due to the creation of small feature size by masking, and involves more processing steps than the commercial Al-BSF cell, as shown in Figure 1.16. Also, high quality starting wafers (lifetime of ~1 ms) are required for these high efficiency cell, which further increases the cost of solar cells and modules.

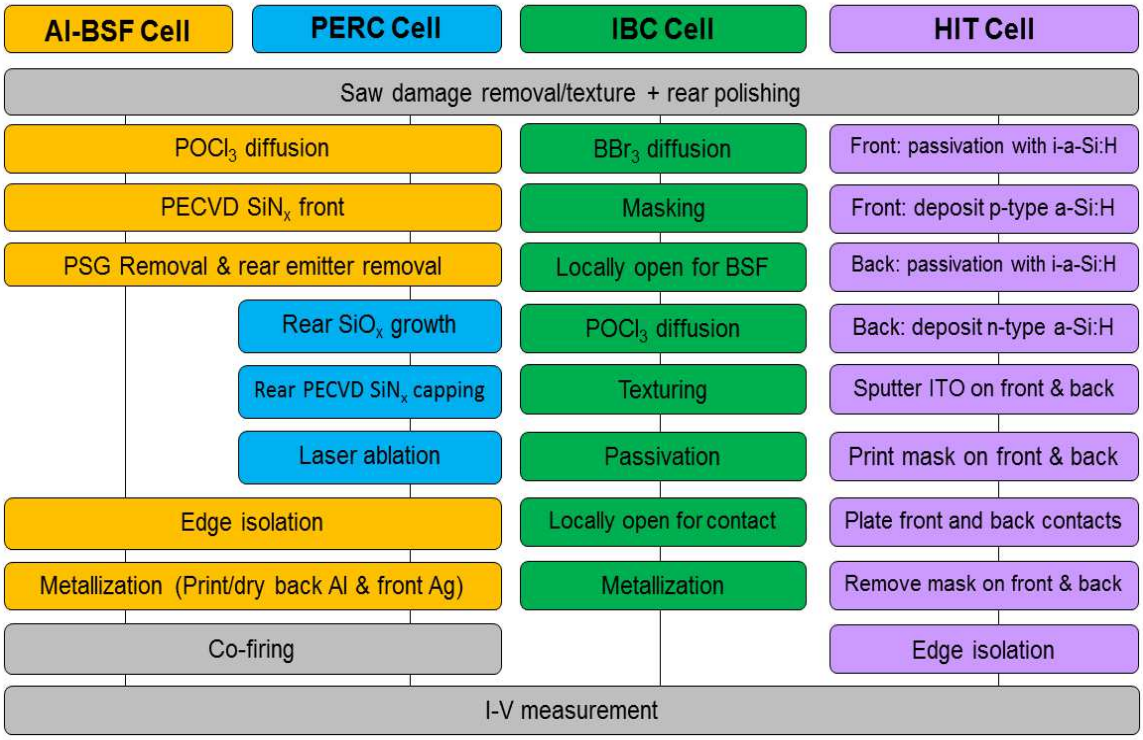

Figure 1.16: Processing steps for different industrial silicon solar cell technologies.

However, the Al-BSF cell has the potential of giving low-cost with improved conversion efficiency. But it needs to be designed with particular attention to the following

details: (a) Front metal gridline width to decrease shading loss; (b) Less amount of Ag per cell; (c) Improved emitter sheet resistance; (d) Understand screen-printing and contact firing; (e) Paste composition in relation to the solar cell parameters; (f) Reduction in total R_s, which includes the use of more busbars. My thesis, therefore, will be focusing on these issues to achieve ~20% efficient Al-BSF silicon solar cell.

1.6 Chapter Summary

In this chapter, the fundamentals of the working principle of a solar cell and all the factors that affect the conversion efficiency were discussed. In addition to the advantages and disadvantages of the conventional Al-BSF technology, some more advanced solar cell architectures suitable for commercialization were also reviewed, which includes PERC, EWT, MWT, IBC, HIT, Triex Cell and Pluto Cell. However, taking into account the material and cell fabrication cost, the simplicity and low-cost of the Al-BSF cell fulfills the increasing demands of cost-effective solar electricity. Thus in this thesis, the understanding and development of innovative front metallization concept was based on the Al-BSF cell. A highly efficient Al-BSF cell is characterized by (i) thick and uniform rear BSF, (ii) uniform emitter with optimal sheet resistance, (iii) excellent front surface passivation, (iv) uniform front fine-line printing with high precision, and (v) optimized contact co-firing to enable low R_s.

Chapter 2 discusses the impact of BSF on solar cell performance. PC1D device modeling was used to investigate the relationship among BSF thickness, BSRV, V_{oc} and efficiency, and the minimum BSF thickness was identified for high-efficiency Al-BSF cells. To further understand the Al BSF, the Al particle morphology and printed thickness as well

as the peak firing temperature were studied experimentally by using three different Al pastes for the back printing.

Chapter 3 analyzed the impact of emitter sheet resistance on solar cell performance. The advantages and disadvantages of high sheet resistance emitters were discussed, and the optimal sheet resistance for Al-BSF cell was identified based on a generalized calculation model. The model is useful in determining optimum solar cell front design including emitter sheet resistance and the number of gridlines that can achieve the best conversion efficiency.

Chapter 4 assessed the benefits of using multiple busbars in different metallization schemes, and the optimal number of busbars was investigated based on computer modeling. According to the selected gridline geometries and the number of busbars and gridlines, R_s were calculated to determine the modeled I-V data and metallization cost. The great benefit of 5-busbar (5-BB) cell was shown in efficiency enhancement and cost saving.

Chapter 5 experimentally validated the predictions of high efficiency 5-BB cell by solar cell modeling. The 3-, 4- and 5-BB Al-BSF cell were made from the same stock of Motech wafers. The screen-printing process was completed with the same process settings, the same commercial paste by Herareus, and the same screen mesh openings of 40 μm. And the contact co-firing for cells from all groups was performed under the same firing condition. The advantages of 4- and 5-BB cells were explicitly shown in the I-V measurements.

Chapter 6 investigated some promising front grid metallization patterns to further increase the conversion efficiency of the 5-BB Al-BSF cells. In the front metallization design, grid segmentations and uneven busbars were introduced. To accurately evaluate

the effect of various grid patterns, a comprehensive empirical grid model was established. And the path to achieve >20% efficiency was shown theoretically with the new designs.

CHAPTER 2: UNDERSTANDING AND QUANTIFYING THE IMPACT OF BACK SURFACE FIELD ON SOLAR CELL PERFORMANCE

2.1 Introduction

Solar cell efficiency depends on the quality of the bulk material, the front and back surface recombination velocities and the contacts. For conventional solar cells with full Al back, the BSRV depends on the material bulk resistivity and the effectiveness of the Al BSF. To achieve a low BSRV, the deep Al-doped p^+ regions and uniform junctions of BSF are required in the formation process [45]. The Al BSF can vary, depending on the thickness and uniformity of the printed Al. Thicker printed Al correlates with improved cell performance, particularly the V_{oc} and J_{sc} [46]. The Al melt has great surface tension at a high alloying temperature, leading to the formation of surface bumpers because of the melt accumulation and depletion, which causes non-uniformity of the BSF thickness [47-48]. The melt contraction can be alleviated by carefully choosing adequate alloying conditions with optimal ramp-rate, peak temperature and dwell time to enable a higher quality BSF [48].

Theoretically, surface recombination requires the presence of electrons, holes and the defect states. And surface recombination velocity (SRV) is proportional to the density of surface state, and the concentration of electrons and holes, particularly similar concentration of both of them [49]. For p-type Si substrate, the BSF works as field-effect passivation layer that creates a high-low junction at the back surface, as shown in Figure

2.1, which significantly reduce the concentration of holes. The thicker and more uniform the BSF, the more effectively the passivation works. The thickness of BSF is a function of the printed amount of Al and the peak firing temperature [50].

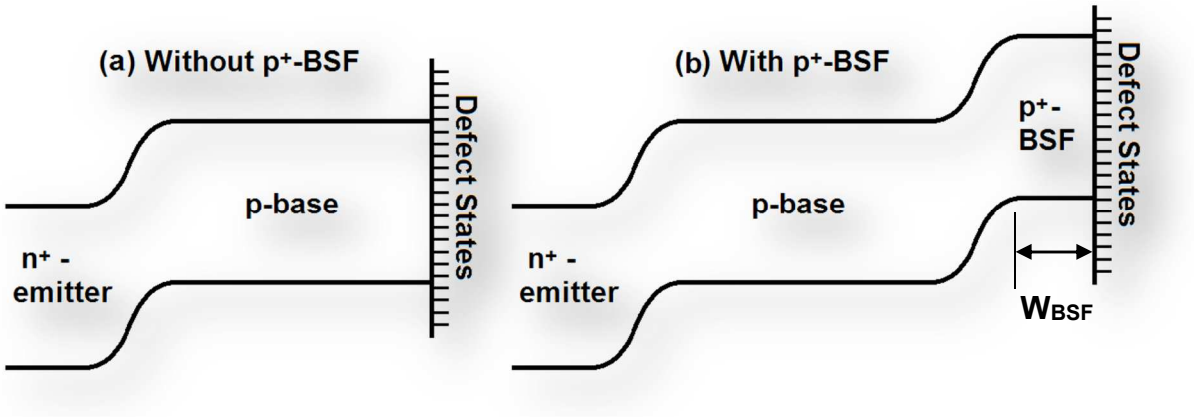

Figure 2.1: Band diagrams illustrating band-bending caused by Al BSF.

However, for increasing amount of printed aluminum, a saturation of the Al-doped p^+-layer thickness was found to be 10 mg/cm^2 [51]. As more aluminum paste continues to be deposited, the thickness of the eutectic layer and aluminum residuals will keep changing while the thickness of BSF region remains nearly constant. As reported by Meemongkolkiat et al [50], a screen-printed Al thickness of 60 μm is needed to achieve a BSRV of 100 cm/s so as to obtain high V_{oc}. Such Al thickness will require >890 °C peak firing temperature for the formation of BSF, which is not compatible with the front contact formation. The wafer will bow so much that the stress on the wafers will outweigh the potential benefits of such thick BSF. More so, as thinner wafers are in use to reduce material costs, it will be challenging to fabricate cells that can be interconnected in the modules. In the light of these challenges, several Al pastes manufacturers have looked into formulating pastes that can provide good dopant concentration for effective BSF and good ohmic contact with negligible bowing. The screen-printed B/Al mixture metallization film

technique has shown increased carrier concentration in BSF and decreased BSRV at low firing temperature (<800°C) with relatively thin Al [52].

With all these Al pastes in the market, a systematic study has not been carried out to understand the contributions of the Al-BSF alone. Such study is important to answer questions such as: (i) Is BSF thickness or uniformity or both critical in reducing BSRV? (ii) Is the improvement in V_{oc} seen in some production lines, when a certain Al is used, due to wafer resistivity or quality? In this study these questions are addressed by using screen-printed Al pastes from three major paste manufacturers and the screen mesh commonly used in the industrial production of solar cells. To exclude any variation from the front contacts, a commercial Ag paste was used and cells were co-fired at optimized peak temperature for the front Ag paste. To understand the impact of temperature on the different Al pastes, three other temperatures were investigated. Finally, PC1D and PC2D were used to evaluate the recombination parameters of the cells.

2.2 Alloying of Aluminum to Form Back Surface Field

Following the printing of Al paste on the back side of the cell, the cell will firstly be dried at ~200°C to evaporate all the solvents in the paste. After the front printing of Ag paste, the cell with printed metal contacts will be transferred to an IR-belt furnace for a three-step co-firing process: burn-out, firing and cooling, as demonstrated in Figure 2.2. And the formation of Al-BSF by the alloying of Al on silicon substrate occurs based on the mechanism as follows [47, 50]: (i) At 300-400°C, the organic binders are burnt out; (ii) Above the Al-Si eutectic temperature (577°C), the alloying of Al and Si starts to take place whereby Si dissolves into the Al-Si melt, leading to a homogeneously distributed liquid phase; (iii) In the cooling down process, silicon is rejected from the Al-Si melt and

epitaxially recrystallizes at the interface of Al/Si, leading to the growth of Al doped p^+ BSF. When the alloying temperature is reduced to the eutectic temperature, the final solidification of the residual Al-Si melt happens, creating a compact Al-Si layer of eutectic composition above the Al-p^+ region with 12.6 Wt% Si.

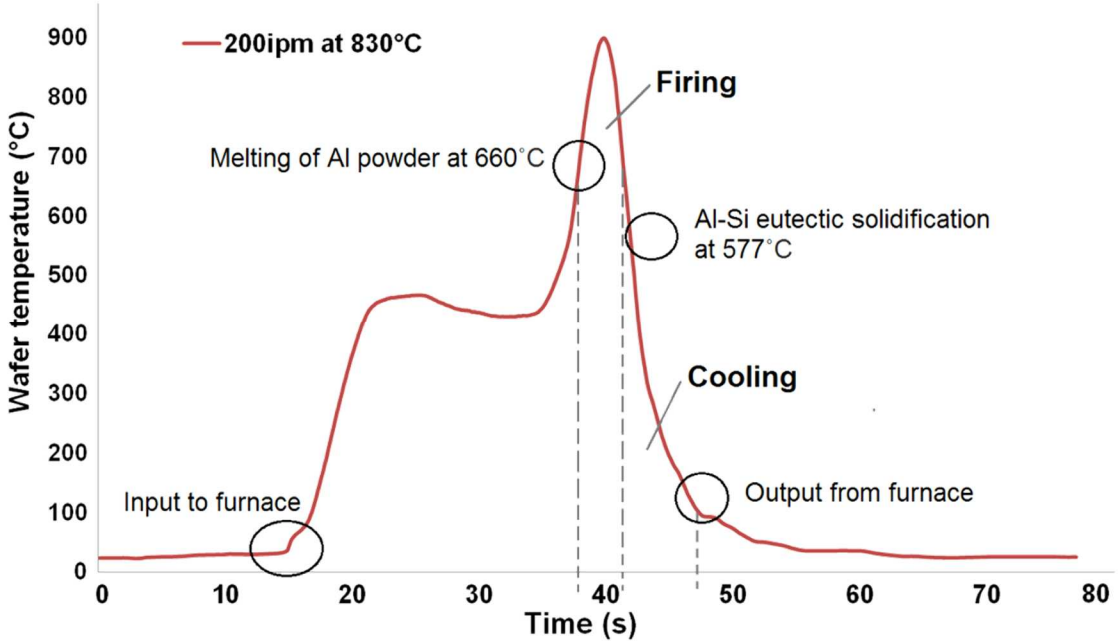

Figure 2.2: The three-step firing process of back Al.

Generally, the quality of BSF has a strong dependence on the amount of deposited Al paste and the firing condition such as the ramp-rate, the peak temperature and the dwell time [45-46, 50]. The thickness of the regrown Al doped silicon layer is determined by the amount of aluminum paste used [45] and the amount of Si dissolved into the melt at peak firing temperature [47, 51]. The thickness ($d_{Si,dis}$) and weight ($m_{Si,dis}$) of dissolved silicon can be calculated with the corresponding relationship according to [53],

$$d_{Si,dis} = \frac{m_{Si,dis}}{A \cdot \rho_{Si}} = \frac{m_{Al}}{A \cdot \rho_{Si}} \times \frac{F(T_{peak})}{1 - F(T_{peak})} \tag{2.1}$$

where A is the screen-printed total area, ρ_{Si} the density of Si and $F(T_{peak})$ the atomic weight percentage of Si in the molten phase at the peak alloying temperature.

Since the percentage of Al in the Al doped p^+ layer is negligible, the volume of Al paste particles after final solidification can be assumed to be the same as deposited. Therefore the thickness of the eutectic layer ($d_{Si,eut}$) corresponds to the weight percentage of Si in the eutectic layer, which can be calculated as:

$$d_{Si,eut} = \frac{m_{Al}}{A \cdot \rho_{Si}} \times \frac{F(T_{eut})}{1 - F(T_{eut})} \tag{2.2}$$

The BSF thickness (W_{BSF}) is thus obtained by subtracting $d_{Si,eut}$ from $d_{Si,dis}$:

$$W_{BSF} = \frac{t_{Al} \cdot \rho_{Al}}{\rho_{Si}} \left(\frac{F(T_{peak})}{1 - F(T_{peak})} - \frac{F(T_{eut})}{1 - F(T_{eut})} \right) \tag{2.3}$$

where t_{Al} represents the thickness of screen-printed Al layer, ρ_{Al} the density of Al.

From Eq. (2.3), we can see that the quality of Al-BSF depends on the thickness of deposited aluminum and the peak alloying temperature, and W_{BSF} can be improved by increasing t_{Al} or T_{peak}. However, a critical temperature exists for a given screen-printed thickness. This critical temperature decreases with increased amount of printed Al paste [50]. Al melt has a large surface tension and tends to ball up during the firing step, especially when the firing temperature exceeds the critical temperature, resulting in serious lateral thickness inhomogeneity of BSF [48].

On the other hand, the higher the peak alloying temperature, the more heavily Al-doped p^+ region will be obtained. For the peak alloying temperatures ranging from 740-900°C, the Al-doped p^+ layer have a peak concentration in the range of $1\text{-}3\times10^{18}$ cm^{-3}, while in most p-type silicon wafers, the base doping concentration is lower than 2×10^{16} cm^{-3}, resulting in a high-low junction from the difference in doping concentration [50]. The electric field created in between the high and low doped region introduces a barrier that

keeps the minority carriers away from high recombination rear contact, which reduces BSRV.

2.3 Modeling of Back Surface Field on Solar Cell Performance

In order to better understand the effect of Al BSF on solar cell performance, the PC1D device-modeling program was used to quantitatively investigate the impact of BSF thickness on BSRV, V_{oc} and efficiency. Table 2.1 shows the key material and device inputs used in the PC1D modeling [54]. Note that PC1D is a one-dimensional model, therefore the BSF was assumed to be uniform for any given thickness.

Table 2.1: Modeling parameters for the n^+-p-n^+ solar cells.

Device Parameter	**PC1D Input**	**Device Parameter**	**PC1D Input**
Cell thickness	300 μm	Lifetime (τ)	60 μs
Base resistivity	2.0 Ω·cm	Series resistance (R_s)	0.6 Ω·cm^2
Front grid shading	6.0%	Shunt resistance (R_{sh})	3333 Ω·cm^2
Rear internal reflectance	45%	Front doping	75 Ω/□
FSRV	60000 cm/s	Junction reverse saturation current density (J_{o2})	8 nA/cm^2
Front texture depth	3 μm	n_2	2.5

2.3.1 Impact of BSF Thickness on BSRV

The model calculations in Figure 2.3 show that the thickness of BSF is very critical in achieving low BSRV and hence high V_{oc}. As BSF thickness approaches zero, BSRV increases dramatically to a very high value, which will consequently impact V_{oc} and the cell conversion efficiency. It is worth mentioning that to obtain BSRV <200 cm/s, the minimum BSF thickness of 6 μm is required. More so, for BSF thickness of >6 μm, BSRV does not gain significant improvement as the BSF thickness increases. This suggests that the printed amount of Al on the back side of the cell should be optimized for the optimal thickness of BSF, in order to achieve cost-effective solar electricity.

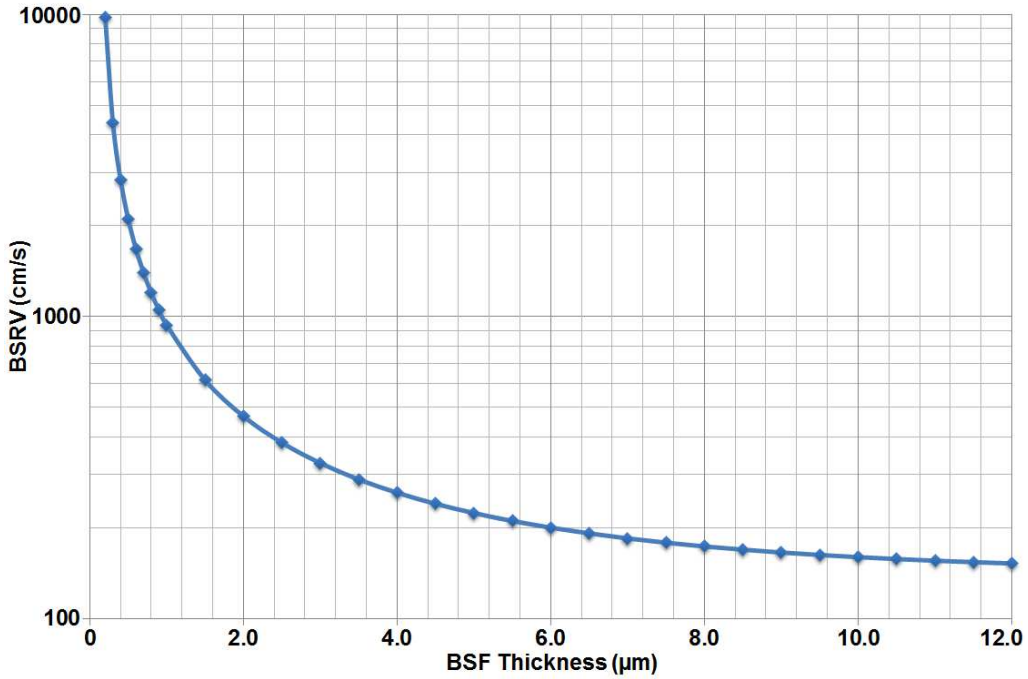

Figure 2.3: BSRV plotted as a function of BSF thickness.

2.3.2 Impact of BSRV on V_{oc} and Efficiency

To further investigate the effect of Al BSF on solar cell performance, the impact of BSRV on V_{oc} and cell efficiency was modeled and plotted in Figure 2.4 and 2.5, respectively. In Figure 2.4, V_{oc} increases as BSRV decreases, and V_{oc} of >638 mV can be achieved for BSRV <200 cm/s. Within this range, very small variation of V_{oc} was found as BSRV approaches zero, indicating that the V_{oc} becomes limited by J_{oe} rather than J_{ob} for very low BSRV. While in Figure 2.5, the cell efficiency shows similar variation curve as a function of BSRV. To achieve >19% efficiency, the BSRV needs to be maintained at <500 cm/s. And with BSRV <200 cm/s, the device conversion efficiency can be further increased to >19.3%. Therefore, to achieve high V_{oc} and high efficiency, BSF thickness of 6 μm with great uniformity is required.

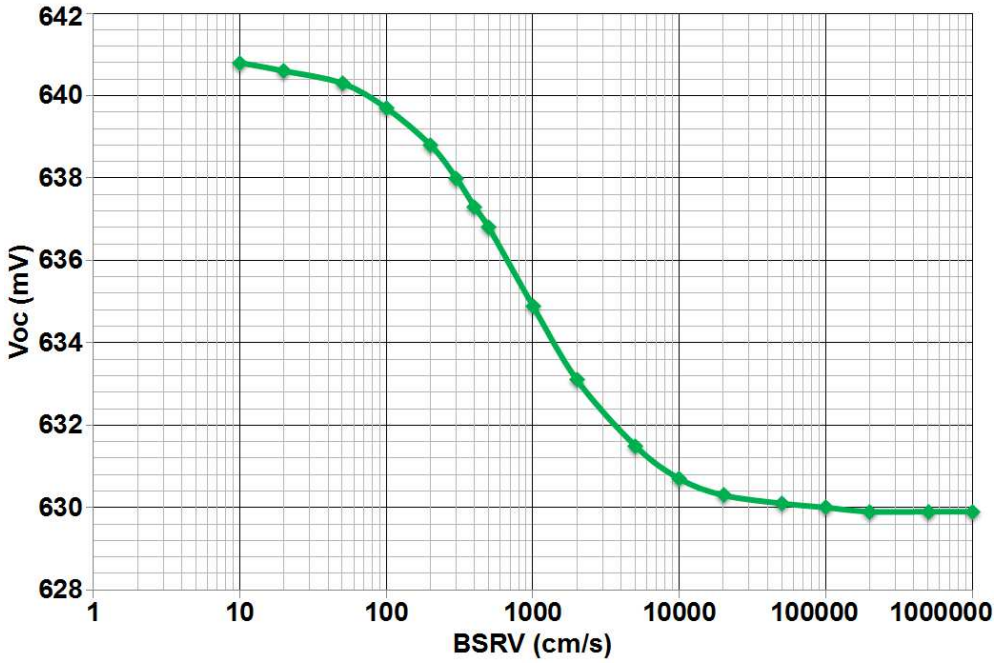

Figure 2.4: Voc plotted as a function of BSF thickness.

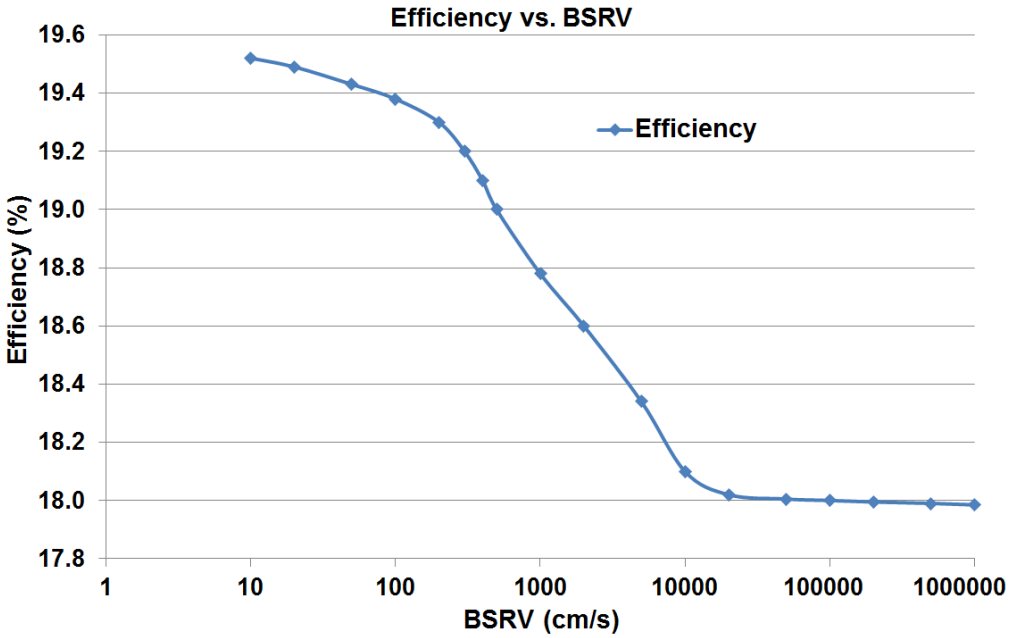

Figure 2.5: Efficiency plotted as a function of BSF thickness.

2.4 The Impact of Al Pastes on Al BSF

The Al paste consists of Al particles that are either spheres or flakes in morphology or a combination thereof in addition to the organic binders and additives. The V_{oc} of a solar

cell is function of the Al BSF thickness as well as the Al paste constituents. The thickness of the printed Al dictates the peak firing temperature and the BSF thickness, which impacts the V_{oc}. To understand the impact of the Al constituents on the performance of a solar cell, three different Al pastes were investigated.

2.4.1 Experimental

Large area (239 cm^2) p-type CZ 2.6 Ω·cm cells were fabricated on commercial 65 Ω/□ emitter using Al pastes from three different manufacturers A, B and C, and the three different Al pastes were printed on 10 wafers each. The cells were fired at optimized peak temperature of 744°C. After the light current voltage (LIV) measurements of the fired cells, some of the cells were cut for SEM study to establish the BSF depths and uniformity. The IQE on the best cells was also carried out to investigate the differentiators in the three Al pastes.

2.4.2 Results and Discussion

2.4.2.1 Best Cells Electrical Properties Comparison

Table 2.2: Light I-V data comparison for best cells with different Al pastes fired at 744°C.

Paste	V_{oc} (mV)	J_{sc} (mA/cm^2)	FF (%)	η (%)	R_s (Ω-cm^2)	BSF thickness (μm)
A	636	37.3	76.7	18.2	1.158	6.84
B	635	37.2	77.6	18.3	1.016	5.49
C	637	37.2	78.3	18.6	0.931	6.93

LIV measurements were carried out on fully processed cells. Table 2.2 shows the results of the best cells fired at optimized peak firing temperature depending on the composition of commercial front Ag paste. Note that the variation in FF and efficiency (η)

for the cells with the three sets of Al pastes may be due to variation in front Ag printing rather than the Al.

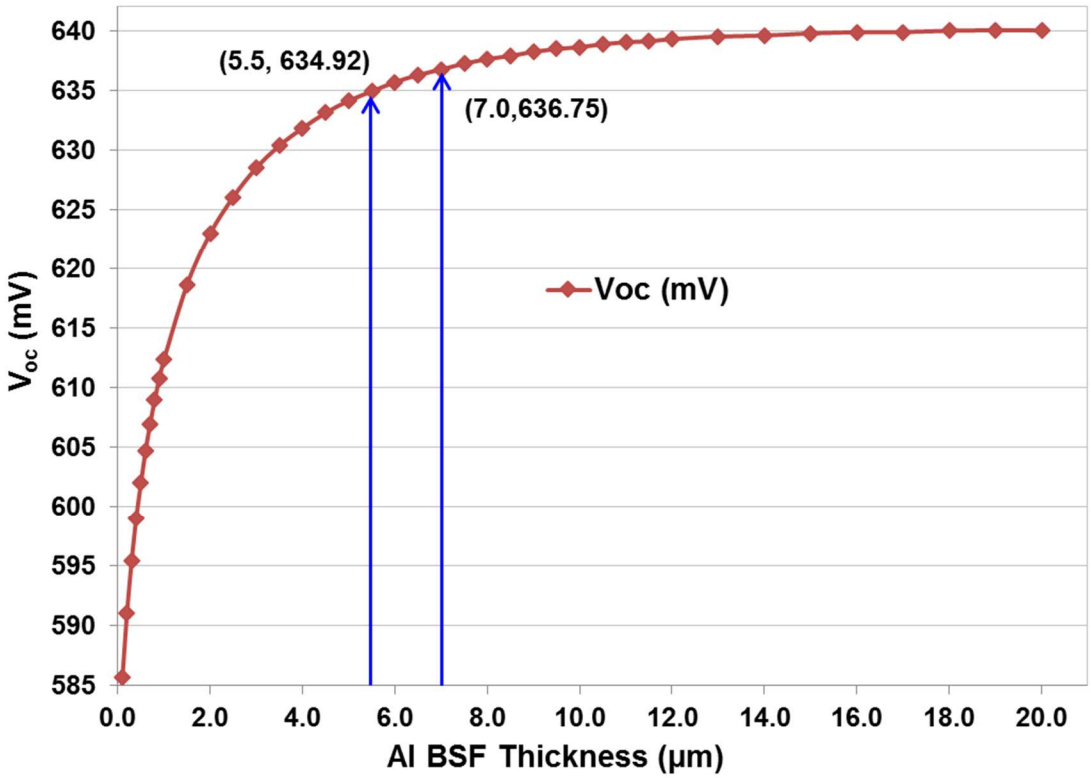

Figure 2.6: Variation of V_{oc} with Al-BSF thickness

Table 2.2 shows a 2 mV difference in V_{oc} for cells that had Al pastes B and C; and 1 mV between cells with A and B, and A and C. The ΔV_{oc} of 2 mV for cell with Al paste B is not necessarily due to thinner BSF by paste B, but may suggest a non-uniform thickness across the backside. However, a change in BSF thickness from 5.49 µm to 6.93 µm can produce a 2 mV change in V_{oc} as shown in Figure 2.6, the variation of V_{oc} with Al-BSF thickness, which assumes uniform Al-BSF. Whereas, the ΔV_{oc} of 1 mV between cells with Al paste A and C cannot be accounted for since the BSF thicknesses are so close to each other. The difference in V_{oc} may come from other factors such as the BSF uniformity.

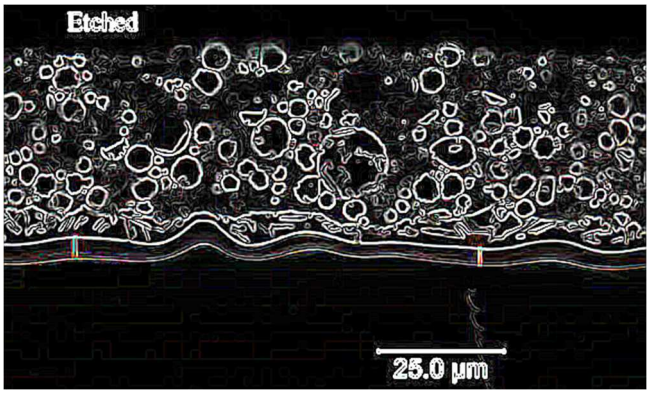

Figure 2.7 (a): SEM micrograph of Al-paste A.

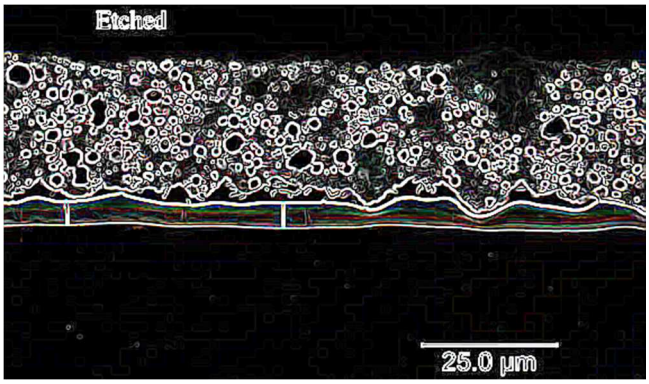

Figure 2.7 (b): SEM micrograph of Al-paste B.

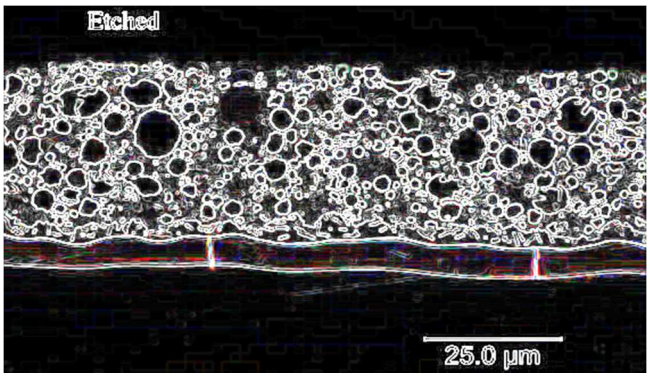

Figure 2.7 (c): SEM micrograph of Al-paste C.

The non-uniformity in the Al-BSF for pastes A and B can be attributed to Al morphology as shown in Figures 2.7 (a) to 2.7 (c) for the three commercial pastes. The Al particle size is different for each Al paste. Possibly the viscosity will be different and so the rheology of the three pastes, and hence different printed thickness. The printed Al thickness varied from 27.3 µm for paste B and 34.1 µm for A to 34.5 µm for paste C.

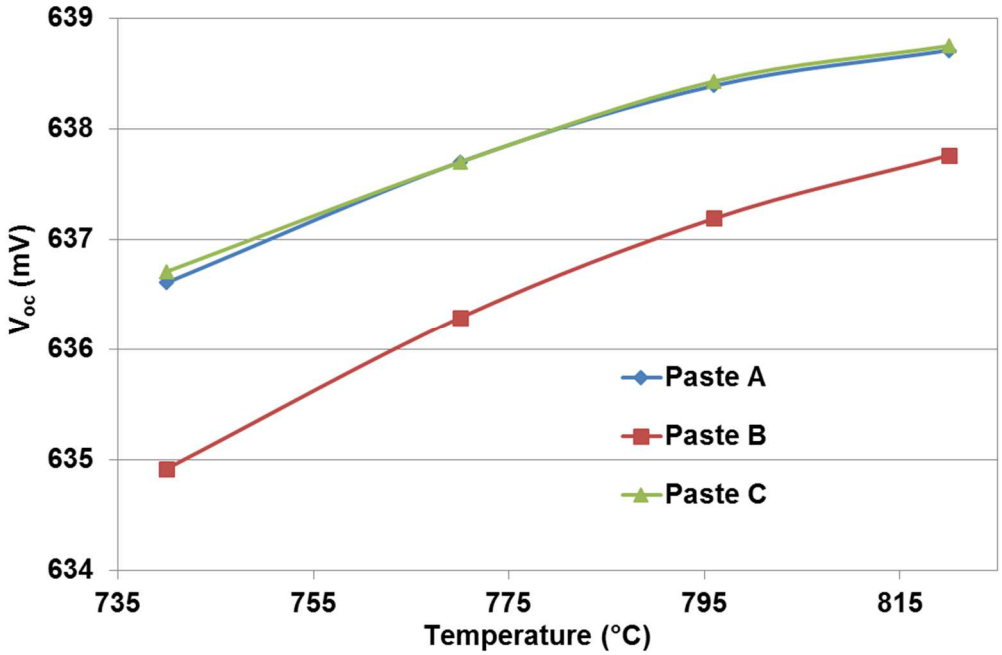

Figure 2.8: V_{oc} as a function of peak firing temperature for Al pastes A, B and C.

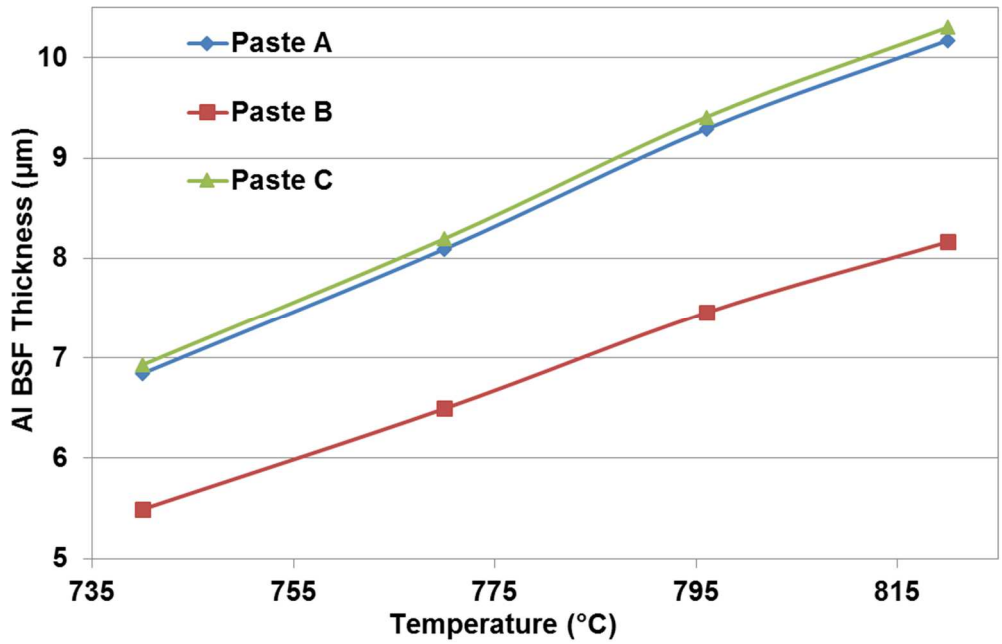

Figure 2.9: Al BSF thickness calculated from Eq. (3) for cells with Al pastes A, B, C and modeled at different temperatures (744°C, 770°C, 796°C and 820°C).

It can also be possible that the peak firing temperature of 744°C was not suitable to all the three pastes; therefore, more work was carried out to vary the temperature. Figure

2.8 shows the V_{oc} as a function of the peak firing temperature for the three pastes. It can be noticed that by changing the temperature from 740-820°C did not make much difference in V_{oc}. Only a modest increment of 2 mV in V_{oc} was obtained, indicates that peak firing temperature does not significantly affect the V_{oc}. Therefore, the lower peak firing temperature was adequate and confirms that the three commercial Al pastes are applicable to multicrystalline silicon solar cell, which favors lower firing temperature. Note that, although the BSF thickness increases with increased peak firing temperature, as shown in Figure 2.9, no significant change occurred in V_{oc}.

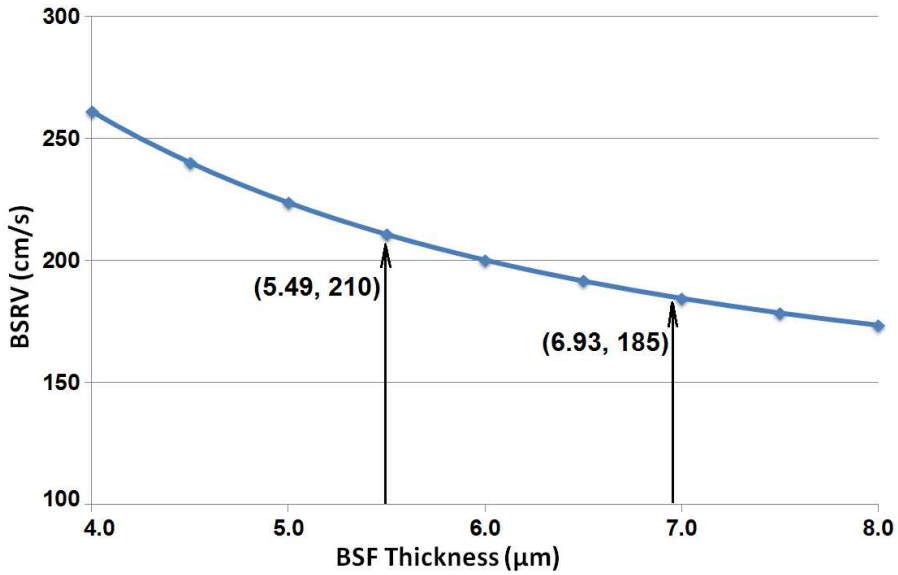

Figure 2.10: BSRV as function of BSF thickness.

The difference in V_{oc} could also be attributed to BSRV due to non-uniform BSF. Figure 2.10, which shows BSRV as a function of BSF thickness, demonstrates a modest ΔBSRV of 25 cm/s between BSF thickness of 5.49 µm and 6.93 µm.

The variation in efficiency for the three set of cells is due mainly to the R_s, which resulted FF of ~0.767 for cells with paste A, 0.776 for B-cell and 0.783 for C-cell. It should be noted that for full Al-BSF cell, the R_s component from back contact is very small as to

be negligible. Thus the different Al will not make any difference in the R_s. The difference in the R_s must have come from the front metal contact. The line width and height for the different cells must have been different. Also, line breakage could have been responsible for such difference. The same number of gridlines was used so the emitter resistance may not cause the difference in FF. The fact that J_{sc} are similar indicates the gridline width is the same.

2.4.2.2 Electroluminescence (EL) Analysis

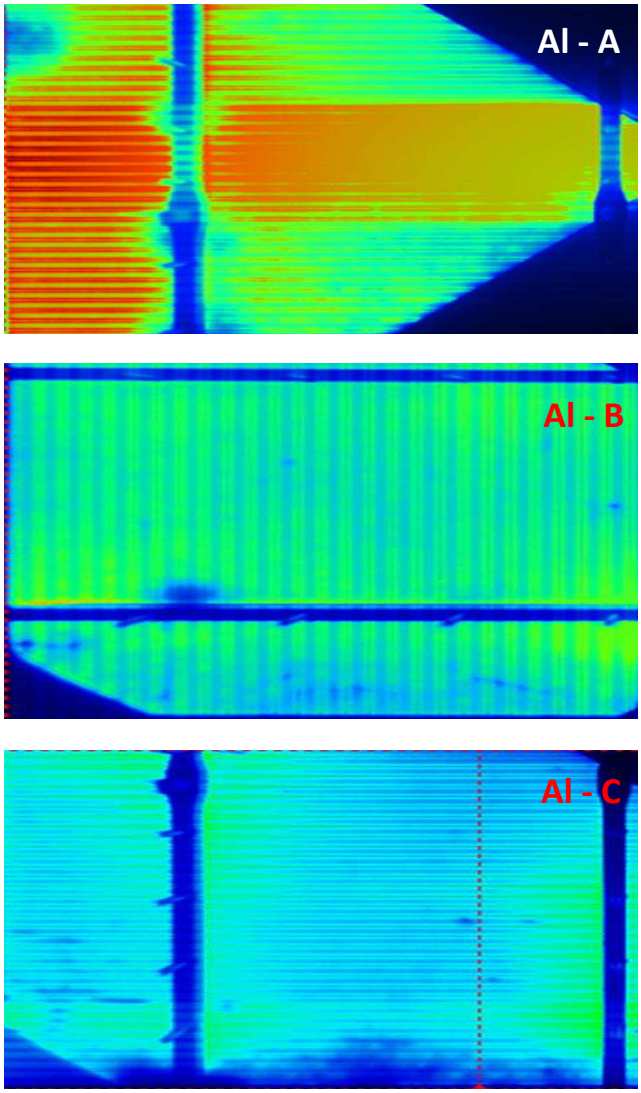

Figure 2.11: Comparative EL analysis of front contacts for cells made with Al paste A, B, and C, respectively.

In order to understand the FF difference observed in the cells made with Al paste A, B and C, the EL measurement was carried out; the images are shown in Figure 2.11. For cell with Al paste A, the front contact shows some non-uniformity, which suggests broken gridlines and hence the high total R_s and hence the lowest FF. The other two samples are similar and that is why the R_s values are close.

2.4.2.3 IQE Analysis

Figure 2.12 illustrates the measured internal quantum efficiencies (IQE) in the wavelength range of 300-1200 nm. As can be seen from the plot, the three IQE curves are in good agreement with each other. Particularly in the long wavelength range of 900-1200 nm that is very sensitive to BSRV [50, 55], the solar cells fabricated with pastes A and C have perfect matches of IQE with each other, while the IQE for cell with paste B is slightly below IQE for paste A and C cells. This explains why the V_{oc} for paste B cell is 1mV and 2mV lower than paste A and paste C cell, respectively.

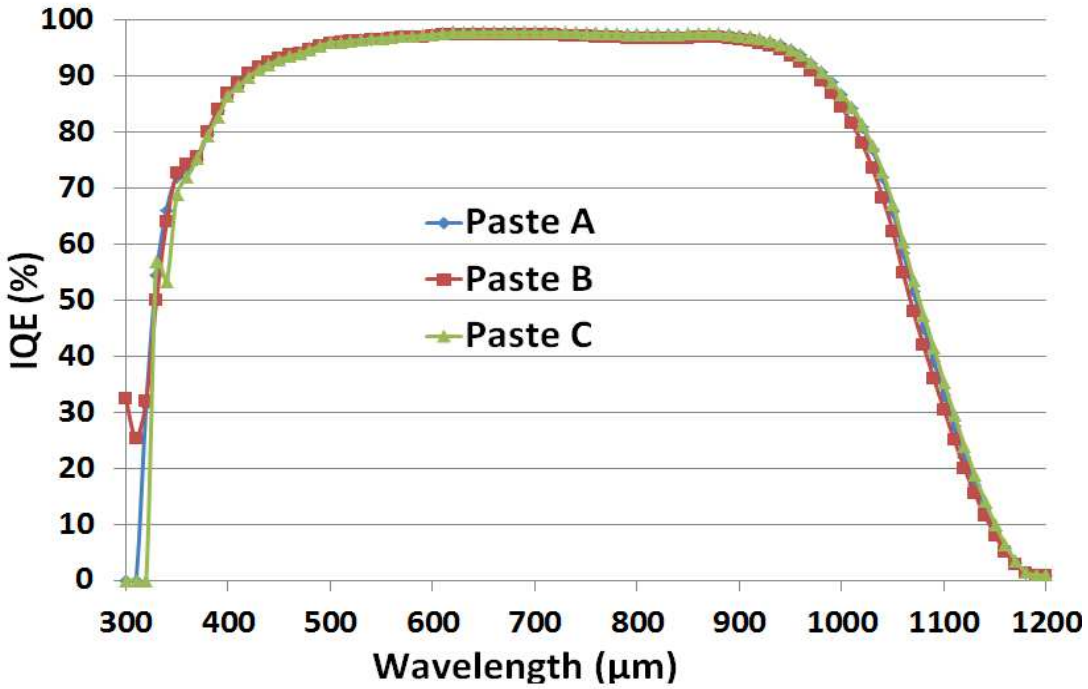

Figure 2.12: IQE analysis for best cells with vendors A, B and C Al-paste.

2.4.2.4 PC2D Simulation

To further investigate the variation in cell performance due to different Al pastes, PC2D simulation was employed to model the cell performance. Modeling for paste A cell were assigned a J_{o1} value of 0.923 pA/cm^2 for metal contacts, and 157 fA/cm^2 for doped surfaces with a sheet resistance of 65 Ω/□. Similarly, J_{o1} of 0.921 pA/cm^2 under metal contacts and 132 fA/cm^2 for doped surface were assigned to paste B cell, and Jo1 of 0.924 pA/cm^2 under metal contacts and 178 fA/cm^2 were assigned to paste C cell. All p-n junctions are assumed to contribute a J_{o2} component of 1 nA/cm^2 [56]. Parameters for specific doping profile and surface treatment can be obtained using PC1D simulation with the experimental measured data. Illumination for each simulation is monochromatic light in the range of 300-1200 nm with 50nm increment when the program was on the run, and the intensity is 0.1 W/cm^2. The same value of 0.4 Ω-cm^2 and 1 mS/cm^2 for extrinsic R_s and shunt conductance were used for each type of cell. By matching the simulated External Quantum Efficiency (EQE) curves with the experimentally measured ones as illustrated in Figure 2.13, we found similar performance of the cells metallized with different Al pastes from Vendor A, B and C as shown in Table 2.3.

Table 2.3: PC2D I-V curve output and calculated FF and efficiency

Paste	V_{oc} (mV)	J_{sc} (mA/cm^2)	FF (%)	η (%)
A	635	37.2	77.47	18.3
B	638	37.1	77.74	18.4
C	635	37.0	77.46	18.2

Compared with the measured data in Table 2.2, the simulated results match the experimental data with the variation of V_{oc} in the range of ± 3 mV and J_{sc} in the range of ± 0.2mA/cm^2. This further supports the experimental result that the Al paste from different

vendors gives similar performance. Thus, provided a uniform Al-BSF of ≥5.49 μm thickness is formed, and cells fabricated under the same condition, V_{oc} >635 mV should be achieved irrespective of the type of Al paste that is used.

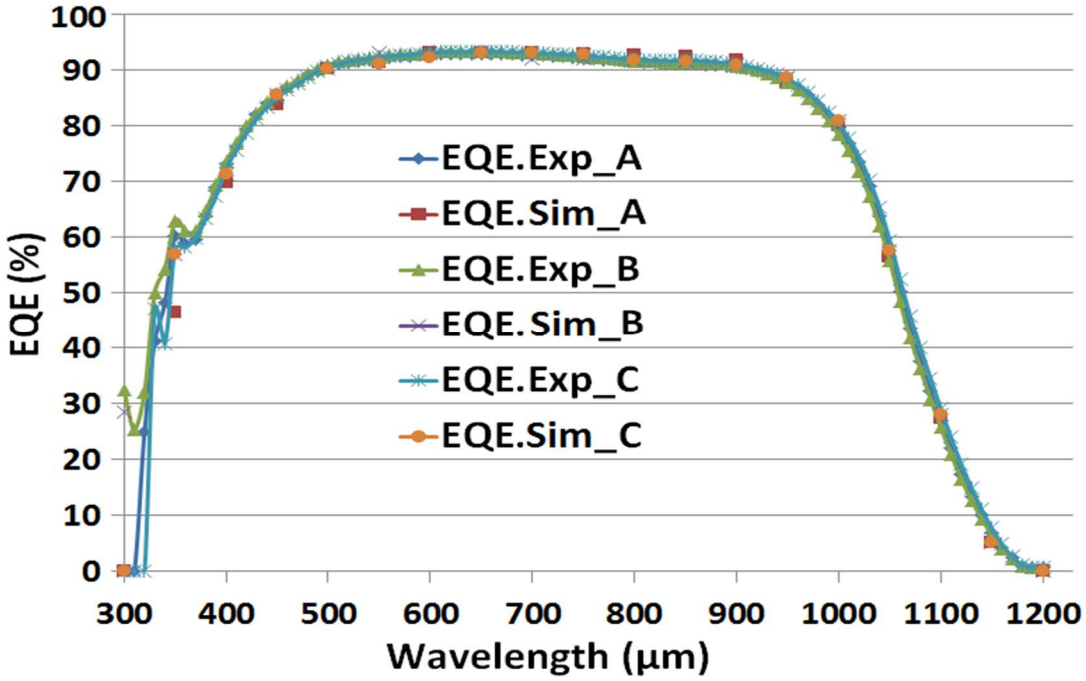

Figure 2.13: Matching of simulated and experimental EQE curve for Cells with Al paste A, B and C.

2.5 Summary and Conclusion

Uniform and thick BSF introduced by Al paste are the key features of a high efficiency conventional Al-BSF silicon solar cell. In this chapter, in order to understand the impact of Al BSF on solar cell performance, the working principle of BSF to help reduce rear recombination was firstly introduced, followed by the review of the mechanism of Al BSF formation by the alloying of Al with Si substrate under high temperature. The relationship of BSF thickness, BSRV, V_{oc} and cell efficiency was evaluated by the PC1D device modeling to show the requirements on solar cell design. It was found that to achieve

V_{oc} >638 mV and efficiency >19.3%, BSRV <200 cm/s and BSF thickness ≥6 μm are needed. To further understand the Al BSF, the Al particle morphology and printed thickness as well as the peak firing temperature were studied by experimentally implementing three different commercial Al pastes from different vendors A, B and C. And the effect of BSF was quantified by investigating the thickness and uniformity of Al BSF and BSRV. It was found that The V_{oc} for the best cells made with the back Al pastes from the three different vendors were similar. However, slight variation in V_{oc} was consistent with theoretical difference in BSF thickness and uniformity. The peak firing temperature did not make much difference in V_{oc} even though the BSF thickness increases with increasing temperature. The J_{sc} for the best cells with vendors A, B and C pastes were very close. The result was also confirmed by SEM, IQE and EL analysis, and PC2D simulation. The measured IQE and PC2D modeled EQE for the three best cells in the short and long wavelength response did not show any remarkable difference. EL analysis showed some broken lines for cell made with paste A and that was responsible for the lowest FF. However, despite the variation in BSF thickness, the cells performance was similar. This suggests that provided the BSF is uniform and has thickness greater than 5.49 μm, V_{oc} ≥635 mV can be achieved.

CHAPTER 3: GENERALIZED ANALYSIS OF THE IMPACT OF EMITTER SHEET RESISTANCE ON SILICON SOLAR CELL PERFORMANCE

Emitter sheet resistance contributes significantly to the distributed series resistance (R_s) of a solar cell. The R_s impacts the FF and in turn affects the J_{sc} and hence the efficiency. It is therefore, imperative to understand the properties of the emitter in order to achieve excellent ohmic contact. In this study, an analytical modeling of the dependence of V_{oc}, J_{sc}, FF and efficiency of a silicon solar cell on emitter sheet resistance was carried out. The impact of sheet resistance on solar cell performance was quantified to determine the optimal sheet resistance in solar cell designs.

3.1 Introduction

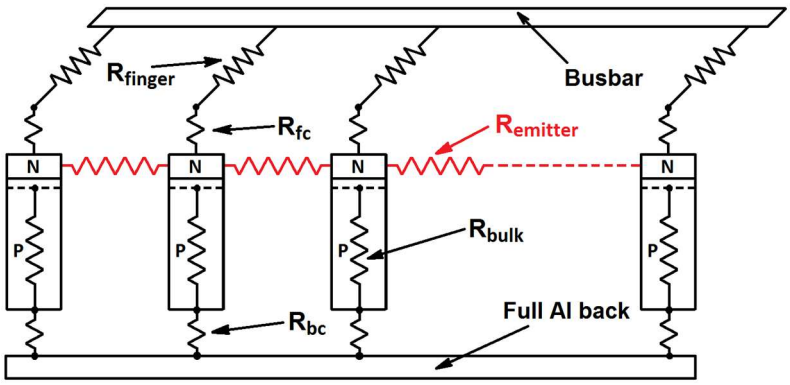

Figure 3.1: Different components of series resistance with the distributed series resistance contributed by emitter sheet resistance - $R_{emitter}$.

Emitter sheet resistance influences the total R_s of a solar cell by contributing to the distributed series resistance interconnecting gridlines, as shown in Figure 3.1. Emitter resistive power loss ($P_{emitter}$) has a linear relationship with sheet resistance (R_{sheet}), as shown

in Eq. (3.1) [57], where J_L is the light-generated current density. Therefore, to overcome the high power loss due to the high series resistance associated with the emitter sheet resistance (80-100 Ω/□), narrower gridline separation (s) is usually required.

$$P_{emitter} = \frac{1}{3} J_L^2 s^2 R_{sheet}\,, \tag{3.1}$$

Screen-printed solar cells of the 1980s to early 2000 utilized emitters with low sheet resistance (40-55 Ω/□) to achieve low contact resistance. However, the low sheet resistance resulted in the loss of blue response and hence low J_{sc} and V_{oc}. The efficiency was in the 16-17% range. Since mid-2000, the use of high sheet resistance (60-100 Ω/□) was on the rise in order to improve the blue response, J_{sc}, V_{oc} and hence the efficiency. However, that has been very challenging for the screen-printed technology because the contact resistance and the emitter resistances must be reduced to achieve good FF.

Some of the issues associated with high sheet resistance emitter include [58-59]: (i) non-uniform emitter, especially using the gaseous diffusion and (ii) shunting associated with shallow junction, and (iii) high contact resistance between metal gridline and silicon. The non-uniform emitter usually causes high contact resistance at local points, which normally controls the total series resistance of the cell [60-61]. The shallow junction depth affects the cell's shunting which may stem from over-firing of the metal contacts.

In spite of these challenges, the benefits of using high sheet resistance are enormous. This includes: (i) enhanced blue (<400 nm) response because the emitter is transparent (ii) lower emitter saturation current density (J_{oe}) accompanied by V_{oc}, provided that an effective emitter surface passivation is achieved [62-64]. Furthermore, PC1D modeling shows efficiency enhancement is a function of base contact resistance, front surface recombination velocity (FSRV), back surface recombination velocity (BSRV) and

minority carrier lifetime. However, the advantage of high sheet resistance emitter will be lost if the base contact resistance and FSRV cannot be controlled at a decent level (e.g. base contact resistance >1 $\Omega \cdot cm^2$ or FSRV >10^5 cm/s).

In order to assess the impact of emitter sheet resistance on solar cell performance, an analytical model was built to investigate the variation of different cell parameters including (i) R_s, (ii) J_{sc}, (iii) V_{oc}, (iv) FF, and (v) efficiency. For any given emitter sheet resistance, optimal metal grid design was determined based on conversion efficiency. And optimal emitter sheet resistance was suggested in conjunction with the number of gridlines, for any fixed gridline geometry.

3.2 Simulation Methodology

The modeling started by using the measured electrical output parameters (Table 3.1) from industrial size (156×156 mm^2), 3-BB monocrystalline silicon solar cell. The cell was fabricated on a 2.5 Ω·cm, p-type, and 180-μm-thick substrate with a full-area Al-BSF. The important electrical and optical parameters are shown in Table 3.1.

Table 3.1: Parameters extracted from reference cell for modeling.

Parameter	**Value**	**Parameter**	**Value**
V_{oc}	630.5 mV	J_{sc}	37.30 mA/cm^2
V_{mp}	521.6 mV	J_{mp}	35.19 mA/cm^2
Efficiency	18.46%	R_s	0.6822 Ω·cm^2
Emitter sheet resistance	80 Ω/□	R_{sh}	2704 Ω·cm^2
Specific contact resistance	3 mΩ·cm^2	FF	0.785
Front metal shadowing	7.59%	n factor	1.03

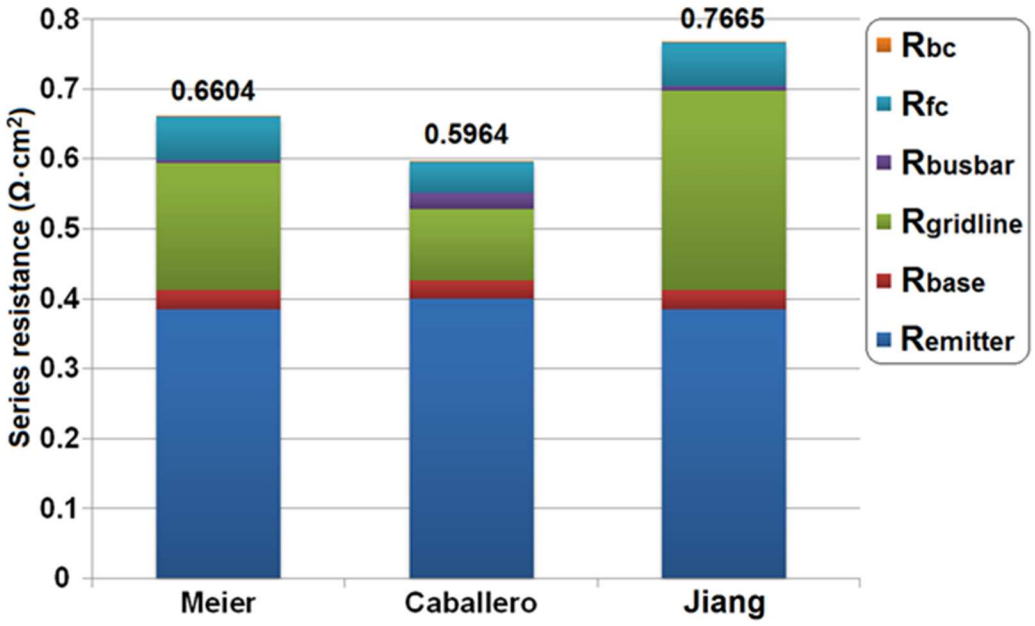

Figure 3.2: Assessment of series resistance with different grid models introduced by Jiang et al. [65], Caballero et al. [66] and Meier et al. [67].

Three grid models, as reported by Jiang et al. [65], Caballero et al. [66] and Meier et al. [67-68], were used to investigate the resistive power losses in the reference cell and Meier et al.'s model best matched the experimentally measured R_s as shown in Figure 3.2. However, Caballero et al. underestimated the gridline resistance by taking the cross section of the practical gridline as a rectangle. While Jiang et al. implemented the Gaussian shape to simulate the practical screen-printed gridline shape to improve the accuracy of the calculation. But because of the non-uniform screen-printed gridlines and the uncertainty in the assumptions, Lin's Gaussian shape grid model still deviated from the measured value. Meier therefore, used the measured busbar-to-busbar resistance (BBR) and front-busbar-resistance (FBR) to circumvent the uncertainties of the non-uniform printed gridlines and the uneven cross sections. As shown in Figure 3.2, this methodology provides a better accuracy in the calculation of R_s. Meier's grid model was therefore, incorporated in our simulation to evaluate the R_s.

It is well known that the specific contact resistivity (ρ_c), is a strong function of the surface doping concentration (N_s). Because ρ_c has an exponential relationship with $1/\sqrt{N_s}$ according to Goetzberger [69], as given by

$$\rho_c = \frac{k}{qTA^*} \cdot \exp\left(\frac{4\pi\sqrt{\varepsilon_{Si} m^*}}{h} \cdot \frac{\Phi_{Bn}}{\sqrt{N_s}}\right), \tag{3.2}$$

where k is the Boltzmann constant, q is the elementary charge, T is the temperature in K, A^* is the effective Richardson constant, ε_{si} is the permittivity of silicon, m^* is the effective mass of the charge carriers, h is the Planck constant, and Φ_{Bn} is the barrier height between metal and silicon.

However, Schubert et al. [70-71] and Hilali et al. [72-74] showed also that ρ_c is a process-dependent parameter, especially during contact firing step, which impact, (i) the density and the size of silver crystallites grown into the emitter, (ii) the contact area between silver crystallites and emitter, and (iii) the shape of pyramids introduced by surface texturing. To make the model of ρ_c more quantifiable, the calculation of ρ_c was established as N_s-dependent.

The saturation current density (J_{o1}) was determined by the emitter saturation current density (J_{oe}) and the base saturation current density (J_{ob}) [75], as given by

$$J_{o1} = J_{oe} + J_{ob} = qn_i^2 \left[\frac{D_n}{N_A L_n} \cdot F_P + \frac{D_p}{N_D L_p} \cdot F_N\right], \tag{3.3}$$

where

$$F_p = \frac{BSRV + \frac{D_n}{L_n} \cdot \tanh(\frac{W_p}{L_n})}{\frac{D_n}{L_n} + BSRV \cdot \tanh(\frac{W_p}{L_n})}, \tag{3.4}$$

$$F_n = \frac{FSRV + \frac{D_p}{L_p} \cdot \tanh(\frac{W_n}{L_p})}{\frac{D_p}{L_p} + FSRV \cdot \tanh(\frac{W_n}{L_p})} \quad . \tag{3.5}$$

Here, q is the elementary charge, n_i is the effective intrinsic carrier density, N_A and N_D are the acceptor carrier density and donor carrier density, respectively. D_n and L_n are the diffusivity and diffusion length of minority carriers for the emitter, and D_p and L_p are for the bulk. W_p and W_n are the thickness of semiconductor materials. The surface effect for both p-type (F_p) and n-type (F_n) are calculated based on back surface recombination velocity (BSRV) and front surface recombination velocity (FSRV), respectively. Some other well established models were adopted to improve the reliability of calculation. These include (i) the bandgap narrowing model [76] to account for n_i, (ii) the resistivity-dopant density relationship model for p- and n-doped silicon [77-78], (iii) the mobility model [79-80] to calculate the sheet resistance from the electrically active doping profiles, etc.

With J_{o1} being determined by the emitter and bulk properties, V_{oc} was calculated as

$$V_{oc} = \frac{kT}{q} \ln\left(\frac{J_{sc}}{J_{o1}} + 1\right), \tag{3.6}$$

where J_{sc} was calculated from the modeled IQE curve and the spectral reflectance with regards to the measured reference values. For different metal electrode designs in terms of the variations of the number of gridlines and gridline width, J_{sc} was also adjusted based on the shadowing loss due to the metal grid coverage. In this work no consideration was made of the potential reflection of sunlight from the top of gridlines. Therefore, the shadowing was directly set as the metallization area on the front surface. In the electrical power loss analysis, the emitter was assumed homogeneous across the whole surface area of the cell,

and gridlines were assumed to be uniform in thickness and width along the gridline and from gridline to gridline, in order to facilitate the calculations in the model.

In the presence of modeled R_s, ideality factor (n) and V_{oc}, FF was estimated according to the method introduced by Green [81], as given by Eqs. (3.7) and (3.8), presuming that the parasitic resistance does not change with different solar cell design in terms of metal electrodes and sheet resistance:

$$\mathrm{FF}_{nS} = \frac{v_{oc} - \ln(v_{oc} + 0.72)}{v_{oc} + 1}(1 - 1.1r_S) + \frac{r_S^2}{5.4}\ , \tag{3.7}$$

$$\mathrm{FF} = \mathrm{FF}_{nS} \cdot \left(1 - \frac{v_{oc} + 0.7}{v_{oc}} \cdot \frac{FF_{nS}}{r_{SH}}\right), \tag{3.8}$$

where FF_{nS} takes into account the effect of n and R_s, while FF also considers the effect of shunting (R_{sh}) in addition to n and R_S. The solar cell conversion efficiency was thus determined by FF in conjunction with V_{oc} and J_{sc} under STC.

3.3 Results and Discussion

3.3.1 Impact of Sheet Resistance and Gridline Width on the Optimum Grid Design

Figure 3.3 demonstrates the variation of the target number of gridline, which gives the best efficiency, based on different sheet resistance and gridline width. It is apparent that as the sheet resistance increases, more gridlines are required in solar cell design to decrease the series resistance due to emitter resistance. For any given sheet resistance, the target number of gridlines also increases with reduced gridline width. This suggests that the gridline resistance, as an important component of the R_s, needs to be optimized for the best efficiency as well. The simulated target number of gridlines was done assuming gridline height of 25 μm. It is shown that, for a sheet resistance of 75-80 Ω/□ and gridline width of 70 μm, the target number of gridlines is 97.

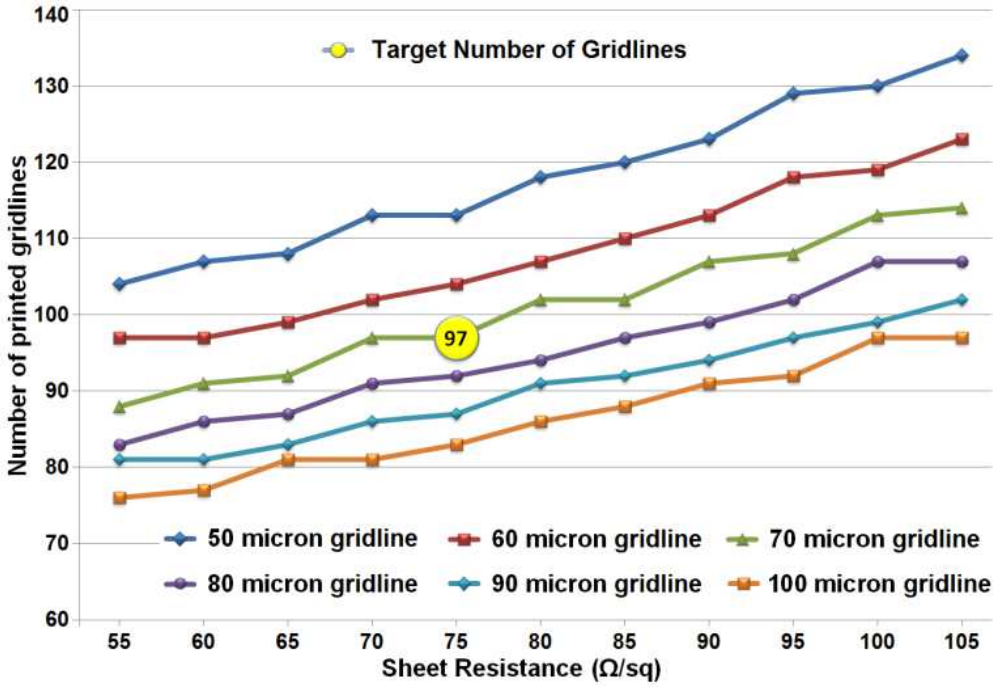

Figure 3.3: Target number of gridlines associated with highest efficiency for different sheet resistance and gridline geometry (e.g., target 91 gridlines gives the best efficiency with emitter resistance of 80 Ω/□ and gridline width of 90 μm and height of 25 μm).

3.3.2 Impact of Sheet Resistance on J_{sc} and V_{oc}

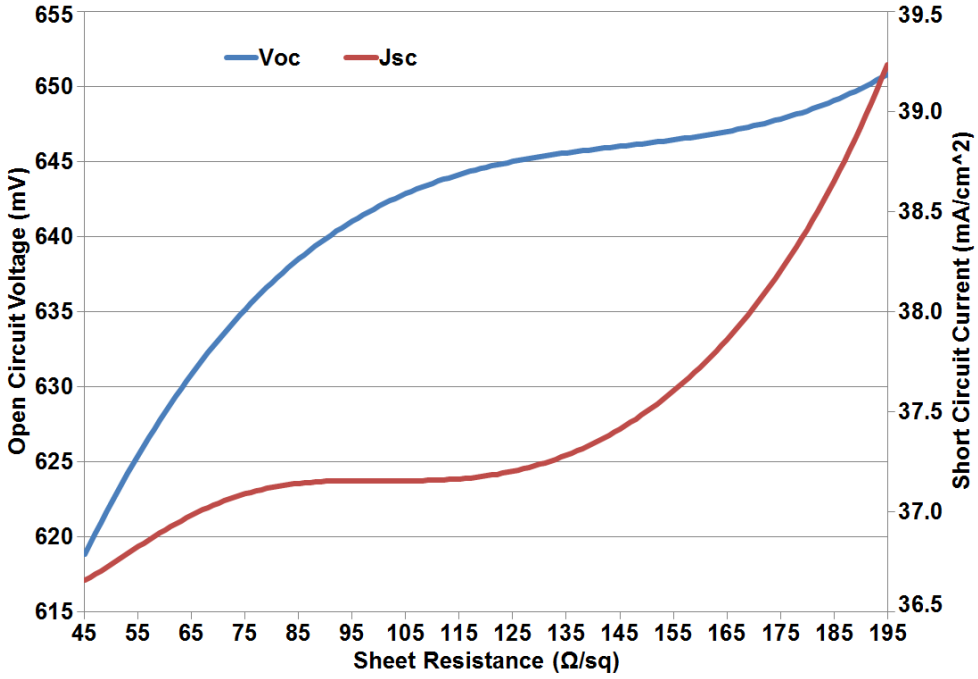

Figure 3.4: Evaluation of open-circuit voltage (V_{oc}) and short-circuit current (J_{sc}) with variation of sheet resistance.

Figure 3.4 shows the curves for V_{oc} and J_{sc} as a function of sheet resistance. Both V_{oc} and J_{sc} improves with increasing sheet resistance. This is due to an improved blue response and reduced FSRV for high sheet resistance emitter. It should be noted that the sheet resistance has little impact on J_{sc} as it varies from ~75 to 115 Ω/□, while V_{oc} increases rapidly within this range. This suggests that J_{oe} has a strong impact cells with emitter sheet resistance ≤115 Ω/□.

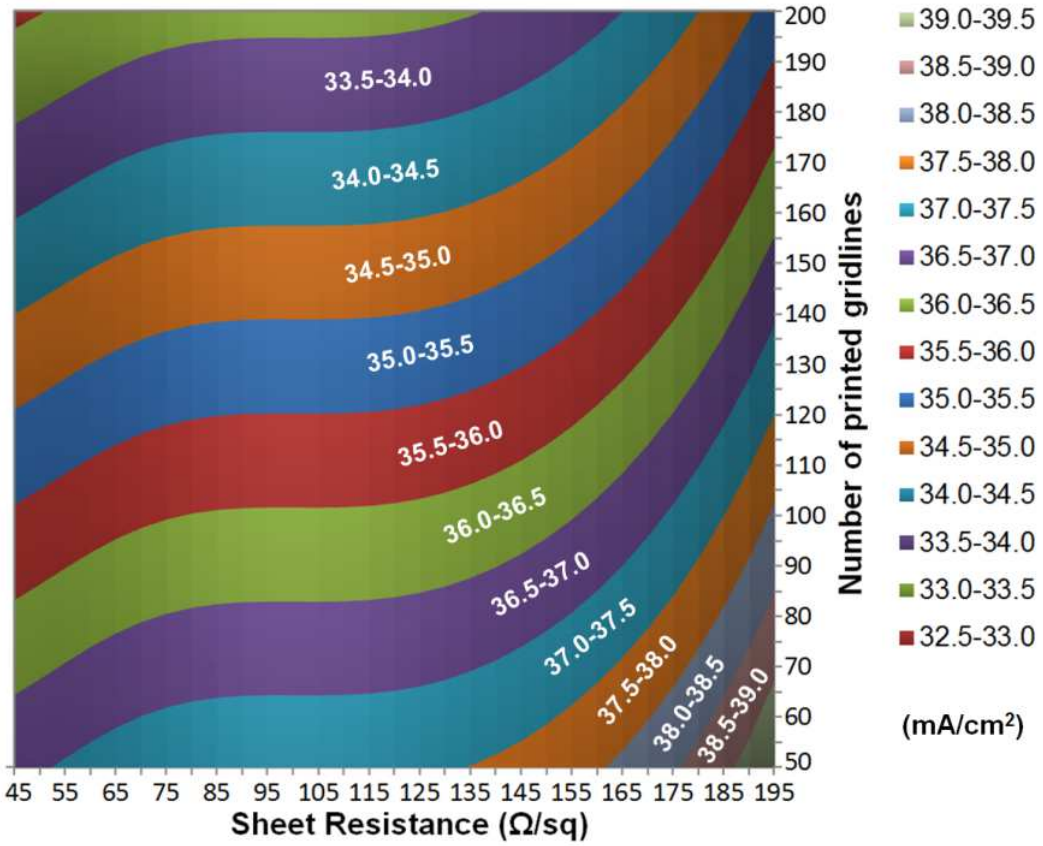

Figure 3.5: Mapping of solar cell short-circuit current (J_{sc}) with varying sheet resistance and number of printed gridlines.

Figure 3.5 illustrates the effect of number of gridlines on J_{sc} with different sheet resistance. As the number of gridline increases, J_{sc} decreases for any given sheet resistance. This is because the metal shadowing loss increases as more gridlines are added. The resistive loss on the hand loss decreases due to improved R_s. This suggests that shadowing

and resistive losses must be balanced, so that the benefit of increased FF due to decreased resistive loss can lead to higher efficiency.

3.3.3 FF vs. Sheet Resistance and Number of Gridlines

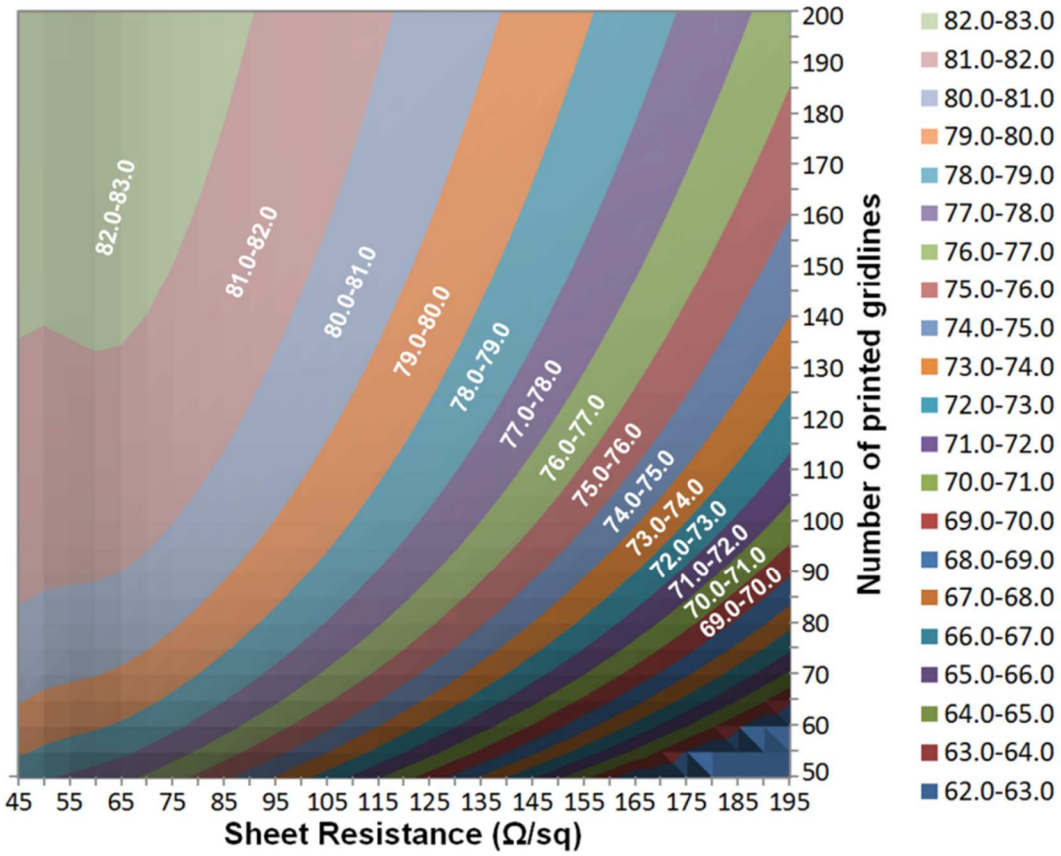

Figure 3.6: Mapping of solar cell fill factor (%) as a function of emitter sheet resistance and printed number of gridlines (gridline width = 100 µm).

Figure 3.6 demonstrates a two-dimensional (2D) contour map of FF vs. sheet resistance and number of gridlines. It should be noted that FF is strongly influenced by the series resistance, which is mainly determined by emitter and gridline resistances. Thus for high sheet resistance emitter and same number of printed gridlines, the emitter resistance dominates and hence the lower FF. This explains the relatively lower FF as sheet resistance increases from 45 to 195 Ω/□, and number of gridlines drops from 200 to 50. Apparently, low sheet resistance and more gridlines are preferred to obtain low R_s of ~0.4 Ω·cm^2, which

will result in high FF of ~0.81. However, low surface recombination and low shading fraction also need to be taken into account for high efficiency solar cells. For 75 Ω/□ emitter, the FF map shows that ~80 gridlines would provide both high FF of ~0.81 and low front shadowing of ~7.81%, and thus high energy conversion efficiency.

3.3.4 Efficiency vs. Emitter Sheet Resistance and Number of Gridlines

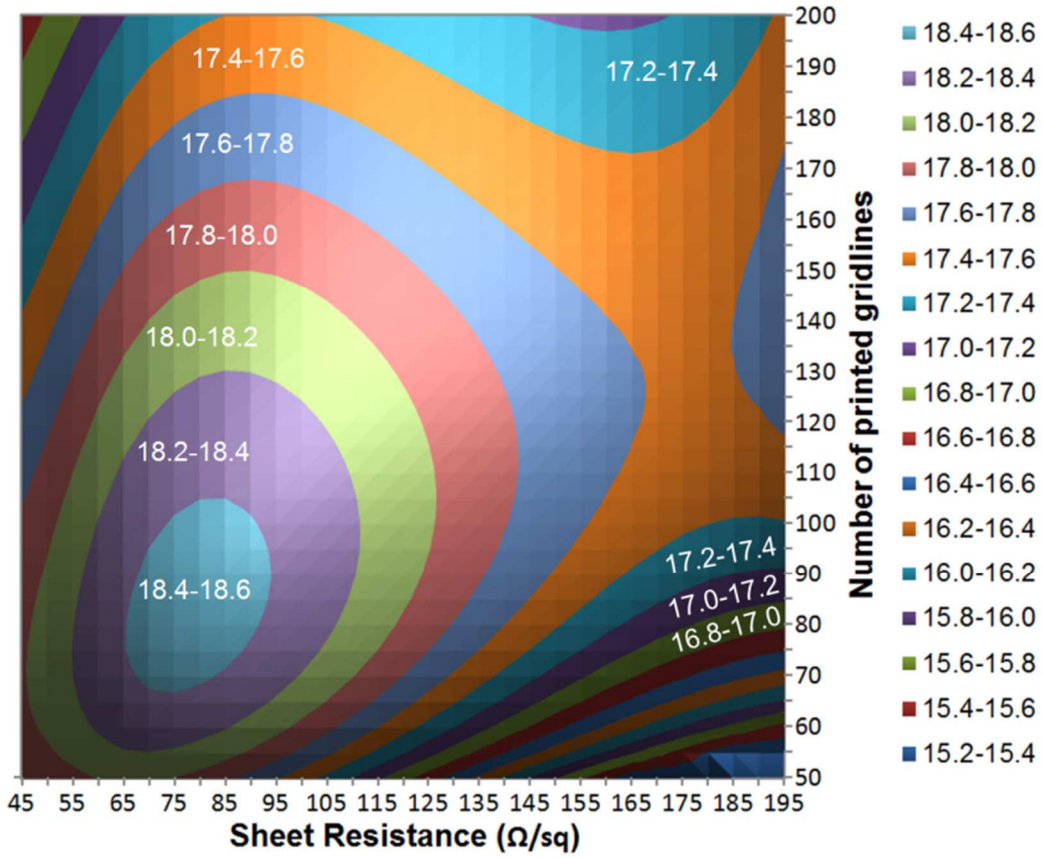

Figure 3.7: 2D contour map of solar cell efficiency (%) as a function of emitter sheet resistance and printed number of gridlines (gridline width = 100 μm).

Figure 3.7 illustrates the corresponding efficiency as sheet resistance and number of gridlines change. The figure shows that, the efficiency range of 18.4-18.6%, correspond to the emitter sheet resistance of ~70 to ~90 Ω/□, and ~65-105 gridlines. It should be noted that the model efficiency is based on the input parameter of the reference cell and higher efficiencies can be obtained as with the reference.

3.3.5 Breakdown of Series Resistance for Different Grid Designs

To understand and quantify the impact of changing gridline spacing, R_s was broken down into different components based on the grid model. Figure 3.8 shows an illustration of two different solar cell designs indicating each component of R_s. In order to get rid of the influence of metal shadowing, the metal coverage was kept the same for the two designs. R_s is most affected by emitter resistance, gridline resistance and contact resistance, whereas, components arising from busbars and substrate are minimal. For grid design with 64 gridlines and 110 µm width, the emitter sheet resistance dominates the total series resistance as shown in Figure 3.8. While for the other design with 88 gridline and 80 µm width, the emitter resistance shrinks by almost half. This indicates that more gridlines, which corresponds to decreased gridline spacing, would effectively enhance the solar cell performance provided the metal shadowing is not increased.

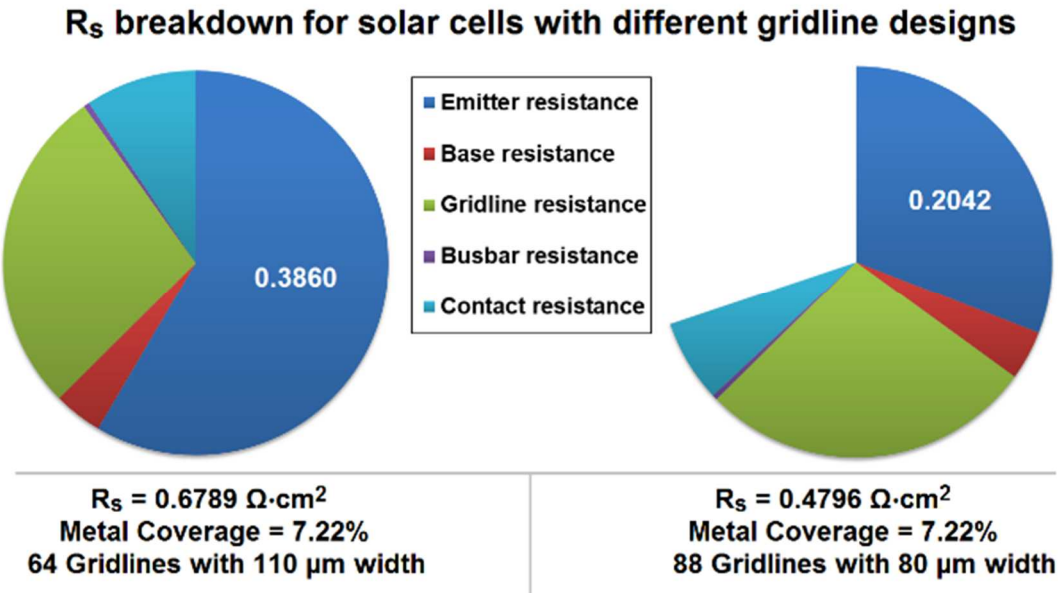

Figure 3.8: Series resistance components for cells with different metal grid designs.

3.4 Experimental Verification of the Modeling Results

In addition to the determination of the optimal emitter sheet resistance in the design of Al-BSF cell, the uniformity of sheet resistance is also critical to achieve low contact resistance for solar cells with consistent high efficiencies [64]. In order to validate the uniformity of the emitter for the Motech monocrystalline wafers used in the experiment, 15 wafers were picked from the same stock of wafers. Based on the modeled the results, all the wafers were doped with ~80 Ω/□ emitter, which is within the optimum range of sheet resistance for high solar cell efficiency. And the front metal electrode was made with a 3-BB and 89-gridline (mesh opening – 70 μm) screen by screen-printing, which resulted in about 80-90 μm gridline width. After contact co-firing, the I-V data for the 15 cells was summarized in Table 3.2.

Table 3.2: I-V data for the 15 cells printed with 70 μm mesh opening screen.

Cell Number	**n-factor**	**V_{oc} (mV)**	**J_{sc} (A/cm^2)**	**FF**	**η (%)**
Motech-Mono-3bb-01	1.06	639.8	37.88	0.7892	19.12
Motech-Mono-3bb-02	1.07	637.6	37.82	0.7957	19.19
Motech-Mono-3bb-03	1.06	638.5	37.90	0.7961	19.26
Motech-Mono-3bb-04	1.06	638.8	37.77	0.7971	19.23
Motech-Mono-3bb-05	1.06	637.3	37.76	0.7924	19.07
Motech-Mono-3bb-06	1.06	638.9	37.80	0.7931	19.16
Motech-Mono-3bb-07	1.07	639.6	37.88	0.7930	19.21
Motech-Mono-3bb-08	1.07	637.6	37.82	0.7959	19.19
Motech-Mono-3bb-09	1.06	637.4	37.76	0.7970	19.18
Motech-Mono-3bb-10	1.06	637.4	37.71	0.7963	19.14
Motech-Mono-3bb-11	1.06	638.3	37.81	0.7930	19.14
Motech-Mono-3bb-12	1.05	638.5	37.80	0.7927	19.13
Motech-Mono-3bb-13	1.07	639.6	37.82	0.7905	19.12
Motech-Mono-3bb-14	1.05	639.7	38.00	0.7861	19.11
Motech-Mono-3bb-15	1.06	639.0	37.82	0.7915	19.13
AVERAGE	**1.06**	**638.5**	**37.82**	**0.7933**	**19.16**
Standard Deviation	**0.005**	**0.87**	**0.066**	**0.0030**	**0.051**

Table 3.2 shows the mean and maximum efficiencies of 19.16% and 19.26%. The average efficiency of 19.16% with a standard deviation of only 0.051 supports the good uniformity of the emitter on the Motech wafers used in this study. The uniformity is also confirmed by the average FF of 0.7933, V_{oc} of 638.5, J_{sc} of 37.82, and n-factor of 1.06 with very small deviation, which are consistent with the uniform emitter across the cell and from cell to cell. This suggests that provided the front printing is uniform and contact firing is optimized, the Motech wafers should give reliable and reproducible good results.

3.5 Chapter Summary and Conclusions

In this Chapter, a generalized calculation model was built to determine the number of gridlines required for a range of sheet resistance. This model is particularly useful in that the emitter resistance is never a single value for every cell, especially, when homogeneous high sheet resistance emitter is explored. The model is useful in determining optimum solar cell design including emitter sheet resistance and the number of gridlines that can achieve the highest efficiency.

In order to better evaluate R_s based on various metal grid designs, different grid models were implemented to investigate the resistive losses. And the one having the best match with the reference cell was incorporated in the simulation. It was found that for a typical 3-BB screen-printed silicon solar cell, the optimal emitter sheet resistance should be in the 70-90 Ω/□ range to achieve the best cell efficiency. Particularly, for sheet resistance of ~75 Ω/□, ~90 gridlines should be incorporated in the design of front metal grid pattern to strike for the best balance between emitter resistive loss and front metal shadowing loss.

CHAPTER 4: INNOVATIVE METALLIZATION PATTERN DESIGNS FOR HIGHER EFFICIENCY AL-BSF CRYSTALLINE SILICON SOLAR CELLS

4.1 Introduction

Key to improving the efficiency of a crystalline cell is to reduce shading loss, increase J_{sc}, V_{oc} without sacrificing the FF. One way of decreasing the shading is the use of narrower gridlines, which is very difficult to print continuous lines without breakages. In order to benefit from the narrow gridlines, even with many breakages, multiple busbars can be introduced, which can also curtail the gridline resistance and improve the FF. In this chapter, the innovation in metallization includes multi-busbar design (Figure 4.1) concept and fine-line printing.

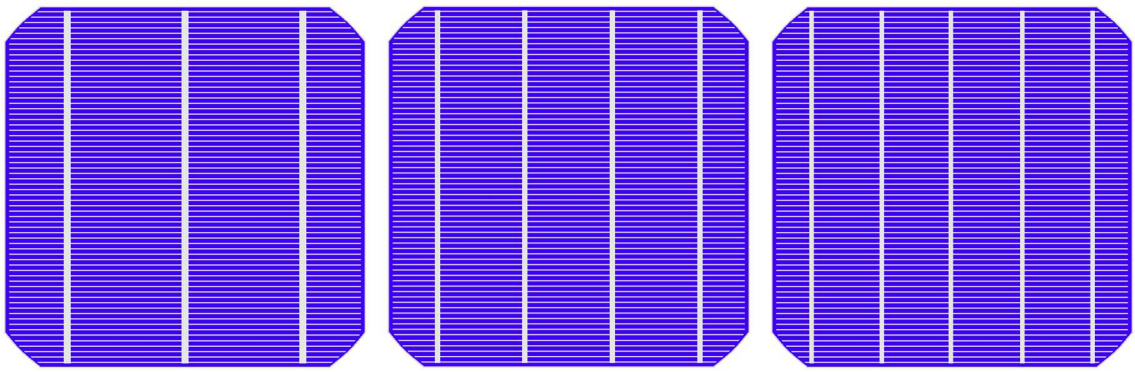

Figure 4.1: Design patterns with different number of busbars.

As the energy landscape changes the solar electricity is becoming more important to augment the conventional sources (coal, natural gas, etc.) of electricity. With decreasing module and balance of system (BOS) cost, the grid parity [41-42] is imminent for wide-spread use of PV electricity for both residential and commercial.

However, the challenges to obtain cost-effective solar electricity include (i) manufacture of high-quality large area crystalline silicon wafers at low cost; (ii) further reduction of wafer thickness without negative impact on solar cell conversion efficiency; (iii) reducing the weight of silver pastes printed per cell or replacing silver pastes with other contacting materials without losing efficiency and stability; (iv) implementation of simple and low-cost processing in conjunction with advanced cell architectures to achieve high efficiency (~22%). All these challenges have been or are still under investigation to decrease the cost of solar electricity in order to attain grid parity.

The quality of silicon wafer has improved remarkably in the last 10-years and the PV industry has been experiencing an increasing surface-to-volume ratio. This is evident in use of thin wafers with very little or no loss in yield and efficiency via improving surface passivation. The metallization of solar cell with alternative metal or reduction in the amount of silver used has been pursued vigorously. This has led to the redesigning and improvement on screens and printing technologies. At the same time the alternative to conventional screen-printing, such as fine-line double printing [82] and digital inkjet printing [83-85] have made great strides.

It is known that metallization impacts the performance of a silicon solar cell optically and electrically, as shown in Figure 4.2. Optically, the front metal gridline coverage contributes to shadowing loss, which directly influences the J_{sc}. Electrically, the resistance of the front metal gridlines, the contact between the metal and silicon, and the associated emitter resistance influence the total R_s. These shadowing losses and resistive losses have been extensively studied in the past [57, 81, 86-89]. Depending on the design and printing quality of the metal electrodes, the gridline geometry (width, height, continuity

and line spacing) can dominate the cell performance. This geometry and the metallization cost are functions of metallization technology such as lithographically defined, buried contact, or printing technology (both impact and non-impact). For example, the gridline of a typical screen-printed solar cell has ~80 μm width and ~20 μm height, compared to the fine-line printed width and height of ~50 and ~15 μm, respectively. It has been demonstrated that fine-line printing (gridline width ≤ 50 μm) is beneficial in silver paste savings and efficiency enhancement [89-90]. In addition, the gridline geometry and metallization cost are also functions of metal grid patterns, the design of which should minimize the metal shadowing loss without impacting the R_s to achieve cost-effective high-efficiency solar cells.

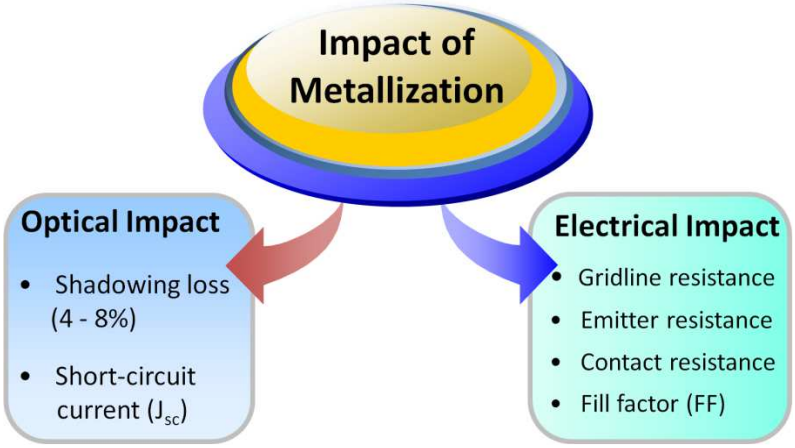

Figure 4.2: Optical and electrical impact of metallization.

For the conventional screen-printed silicon solar cells, the front metal coverage is about 5-8%. And <5% shadowing loss can be achieved when fine-line printing (gridline width <50 μm) is implemented in the metallization process. Decreased shadowing loss may cause increased R_s due to higher contact and gridline resistances associated with decreased contact area and shrunk gridline width. Therefore, printed gridlines require a uniform gridline profile from busbar to busbar in conjunction with a high aspect ratio. However, to

obtain cost-effective solar cell, metallization cost also must be taken into account. Computer modeling shows that for a given number of busbars, the gridline height would have negligible impact on the cell efficiency after being increased to a certain value [91]. This indicates that the aspect ratio of gridlines should be optimized to obtain cost-effective solar cell. It is therefore, crucial to find an optimum metal grid design that is compatible with screen-printing to reduce metallization cost and increase cell efficiency. This will be carried out by the investigation of (i) optimum number of gridlines with fixed gridline width, (ii) the impact of the number of busbars with fixed total busbar width (TBW) (defined as number of busbar * busbar width), (iii) the impact of gridline height, (iv) metallization cost (¢/W).

4.2 Simulation Process

Table 4.1: Parameters extracted from reference cell for modeling.

Parameter	**Value**	**Parameter**	**Value**
Specific contact resistance	3.3 mΩ·cm^2	Efficiency	19.07%
Emitter sheet resistance	80 Ω/□	V_{oc}	641 mV
Gridline width	80 μm	J_{sc}	37.80 mA/cm^2
Gridline height	20 μm	FF	0.7869
Busbar to busbar resistance	0.0721 Ω	R_{sh}	4370 Ω·cm^2
Front busbar resistance	0.1048 Ω	n factor	1.01

The simulation input used the experimentally measured electrical parameters from an industrial size (239 cm^2), 3-BB monocrystalline Al-BSF silicon solar cell. The important inputs, as shown in Table 4.1, were parameters of front electrodes (number of gridlines and busbars and their geometries, gridline and busbar resistances) and recombination (metal, emitter and bulk). Using the above inputs, the metal coverage and series resistance were

calculated. These values were then used to determine the modeled I-V data. The metallization cost was also calculated based on the estimated silver paste consumption, price of silver and power of the cell. The outcome of the modeled 3-, 4- and 5-BB solar cells is presented in Table 4.2.

Table 4.2: I-V data for reference cell and modeled 3-BB and 5-BB cells ($W_{gridline}$ – gridline width, $N_{gridline}$ – number of gridlines).

Cell	V_{oc} (mV)	J_{sc} (A/cm^2)	FF	η (%)	$W_{gridline}$	$N_{gridline}$
Ref. cell	641	0.0378	0.787	19.07	80	74
3-BB cell	640.8	0.0379	0.794	19.29	60	92
4-BB cell	640.8	0.0379	0.805	19.55	60	92
5-BB cell	640.8	0.0379	0.810	19.67	60	92

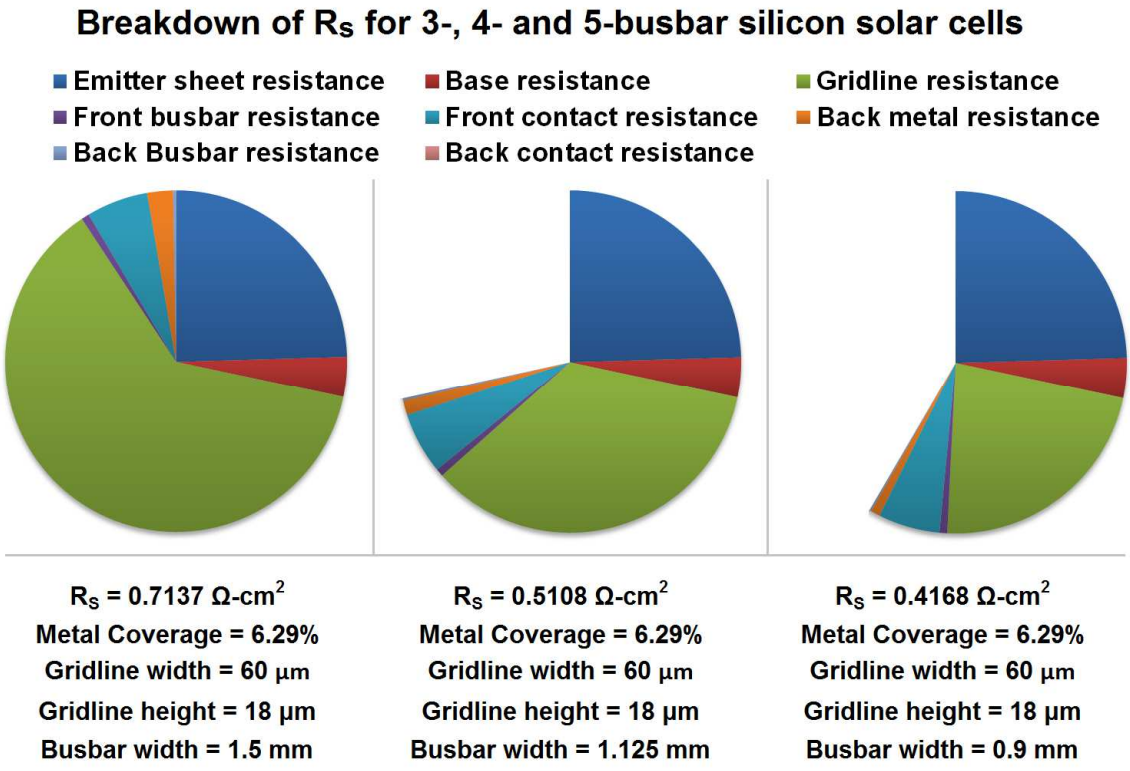

Figure 4.3: Breakdown of series resistance (R_s) for 3-, 4- and 5-BB cells.

In Figure 4.3, the breakdown of R_s for both 3-, 4- and 5-BB grid design signifies that 4- and 5-BB grid designs are superior to 3-BB counterpart, because the gridline

resistance for 4- and 5-BB cell is ~1/2 and ~1/3 of the 3-BB counterpart, respectively. This explains why the FF and efficiency increase as the number of busbar increases. Note that the rest of the series resistance components (contribution of emitter, base, front busbar, front contact, back busbar and back metal) were similar. This tremendous improvement in gridline resistance is related to a reduced effective gridline length for the 4- and 5-BB cells.

Our previous work [92] showed that gridlines should be kept as narrow as possible depending on the capability of printing technology, assuming no gridline breakage. Because for the same total gridline width (gridline width*number of gridlines), the narrower the gridline, the more uniform the distribution of metal coverage will be across the cell, resulting in smaller emitter resistance. And the efficiency would increase with negligible variation in cost. With the current printing technologies, the gridline width of 50-60 μm can be achieved, so the gridline width in the model is set as 60 μm.

Since the practical gridline has a quasi-Gaussian shape rather than a rectangular one, average printed thickness of silver paste (defined as cross-sectional area of gridline divided by gridline width) is used to facilitate the calculation in the model. Gridlines are assumed to be uniform in thickness along the gridline and from gridline to gridline. However, a more accurate model would take into account the non-uniformity of the screen-printed gridline by adding a roughness coefficient [65]. To better assess the series resistance and improve the inaccuracy caused by non-uniform printed gridline, busbar to busbar resistance (BBR) and front busbar resistance (FBR) were directly measured and incorporated in the calculation of R_s according to the methods implemented by Meier [67].

In the modeling, the potential reflection of sunlight from the quasi-Gaussian surface of gridlines was not considered, therefore the shadowing was directly set as the

metallization area on the front surface. Since the surface recombination with gridline contact and non-metallization area varies as the geometries of metal grid change, the V_{oc} was calculated using Eq. (4.1),

$$V_{oc} = \frac{nkT}{q} \ln\left(\frac{J_{sc}}{J_{oe} + J_{ob}} + 1\right) \quad (4.1)$$

where $J_{oe} = F_m \cdot J_{oem} + (1\text{-}F_m) \cdot J_{oeSiN}$. J_{oe} and J_{ob} are the emitter saturation current density and the bulk saturation current density, respectively. F_m is the metal coverage contributed by gridlines. And J_{oem} is the emitter saturation currently density underneath the gridline contact, while J_{oeSiN} is the emitter saturation currently density underneath the SiN_x film at non-metallized area. The values for these parameters are estimated from Hilali's work [93].

The metallization cost (¢/W) was calculated based on the estimated silver paste consumption, price of silver paste and the power of the cell, using the estimated cost of printed silver paste divided by the wattage of the modeled cell. Because of the porosity of printed metal grid, and also the fact that silver paste contains glass frit and organic binder apart from silver, the density of metal gridlines was estimated as 85% of the density of silver. Two scenarios, single-printing (SP) and double-printing (DB), were examined to investigate the impact of busbar height on metallization cost. For single-printing, the busbar and gridline heights are the same but different for double printing.

4.3 Modeled Results and Discussions

Based on the modeled results in Chapter 3, the optimal emitter sheet resistance should be between 70 and 90 Ω/□ for the purpose of low emitter resistance and contact resistance. In this modeling, the emitter resistance was set as 80 Ω/□ to achieve the best results.

4.3.1 Investigation of the Optimum Number of Gridlines

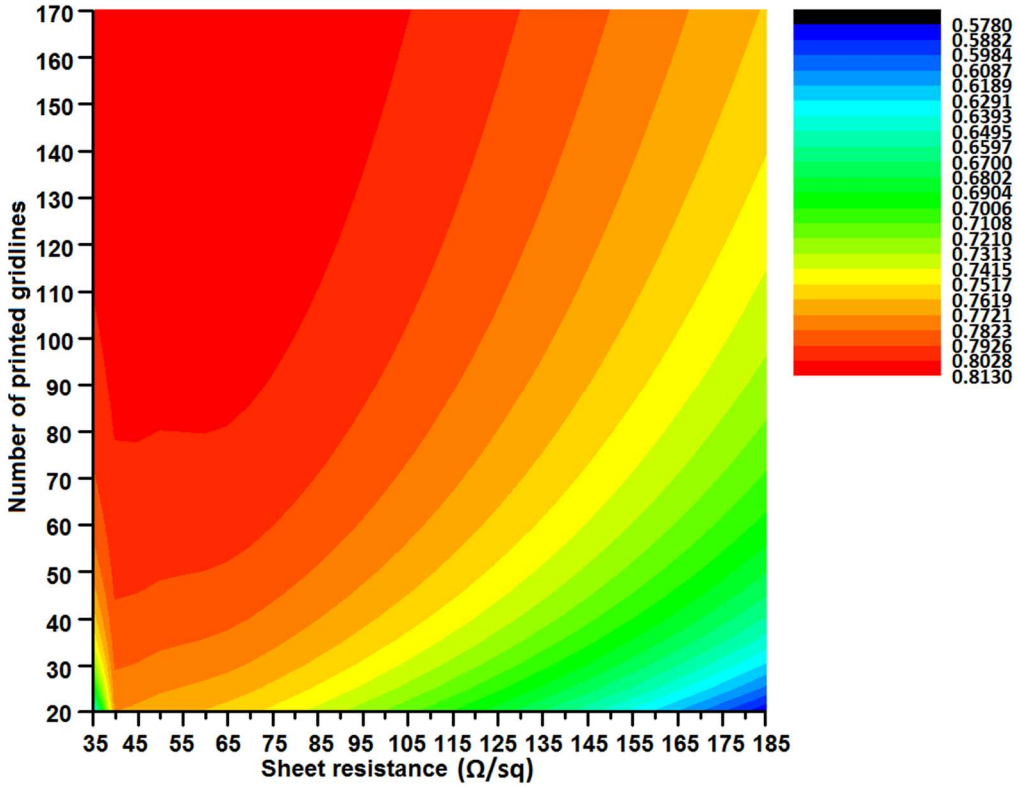

Figure 4.4: A 2D contour map of fill factor as a function of emitter sheet resistance and number of gridlines.

To find the optimum number of gridlines that results in maximum efficiency, a two-dimensional (2D) contour map was created for the resulting fill factor (FF) as a function of sheet resistance and number of gridlines as shown in Figure 4.4. The model shows that FF strongly depends on series resistance, which is mainly determined by emitter and gridline resistances. Thus for high sheet resistance emitter and same number of printed gridlines, the emitter resistance dominates and results in lower FF. This explains the relatively lower FF as sheet resistance increases from ~45 to 185 Ω/□, and number of gridlines drops from >150 to ~20. Obviously, low sheet resistance and more gridlines are preferred to obtain low series resistance of ~0.4 Ω-cm^2, which will result in high FF of ~0.81. However, low surface recombination and low shading fraction also need to be taken into account for

high efficiency solar cells. For 80 Ω/□ emitter, the FF mapping shows that ~90 gridlines would provide both high FF of ~0.81 and low front shading of ~5.72%, and thus high cell conversion efficiency.

4.3.2 Assessing the Impact of the Number of Busbars on Cell Efficiency

In order to assess the impact of the number of busbars on efficiency, the total busbar coverage was kept constant (4.5 mm x 154 mm) to avoid variation in shading fraction as the number of busbar increases. The gridline resistance was independently calculated and plotted with the total R_s to help explain the improvement in FF and efficiency, as shown in Figure 4.5.

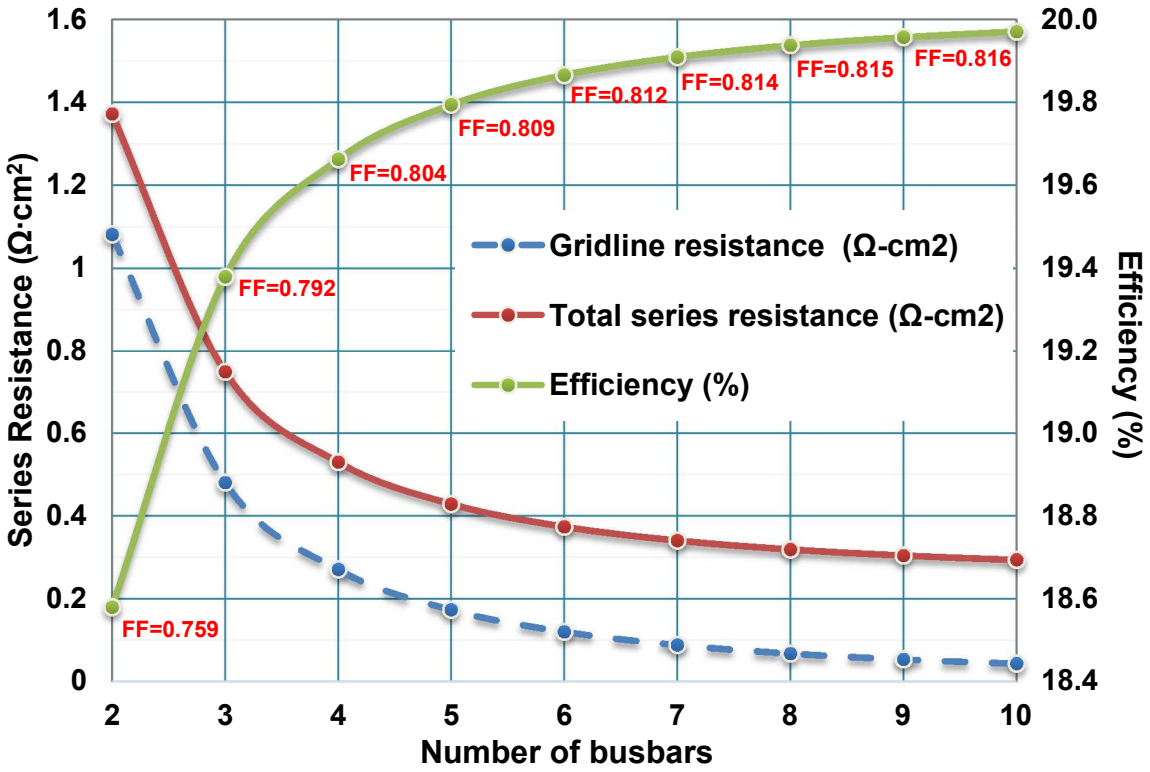

Figure 4.5: Gridline resistance, total series resistance and efficiency plotted as a function of number of busbars with constant total busbar coverage. The associated FF is put along the efficiency curve.

A strong dependence of R_s on gridline resistance was observed as the number of busbar increases, while the variation in the rest of series resistance is negligible. And a significant reduction of gridline resistance was seen as the busbar number change from two to three, three to four, and four to five. This improvement can be explained by reduced effective gridline length associated with more busbars. The effective gridline length for a commercial 6 inch 3-BB solar cell is ~26 mm, for instance, while for a 5-BB solar cell is ~15.6 mm, as shown in Figure 4.6.

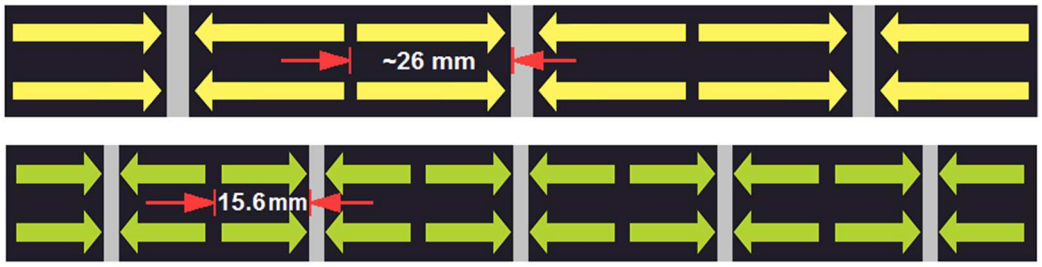

Figure 4.6: Current paths for 3- and 5-BB solar cells.

A closer observation of the plot of efficiency vs. number of busbars would reveal that the efficiency and FF improvement from two busbars to three busbars, and from three busbars to four busbars, tells the evolution of metallization technologies for conventional silicon solar cells to some extent. Actually even for 5-BB solar cell, the busbar still has the width of 0.9 mm, which should not be restricted by the ribbon materials when connected in module. This confirms that it would be beneficial for the solar companies to take advantage of a 5-BB solar cell in the production line. In the future, as the printing technologies improve and module fabrication advances, more busbars should be encouraged in the solar cell design.

4.3.3 Investigation of the Impact of Gridline Height for 3- and 5-BB Cells

To evaluate the impact of gridline height for 3- and 5-BB solar cells, average gridline height, defined as the total cross-sectional area of quasi-Gaussian profile gridline divided by the gridline width, was used in the model to facilitate calculation. Two different scenarios, single-printing (SP) and double-printing (DP) were considered for the impact of gridline height on silver paste consumption and efficiency. For single printing, busbar was kept the same height as gridline, while for double printing, busbar height was kept as 3 μm.

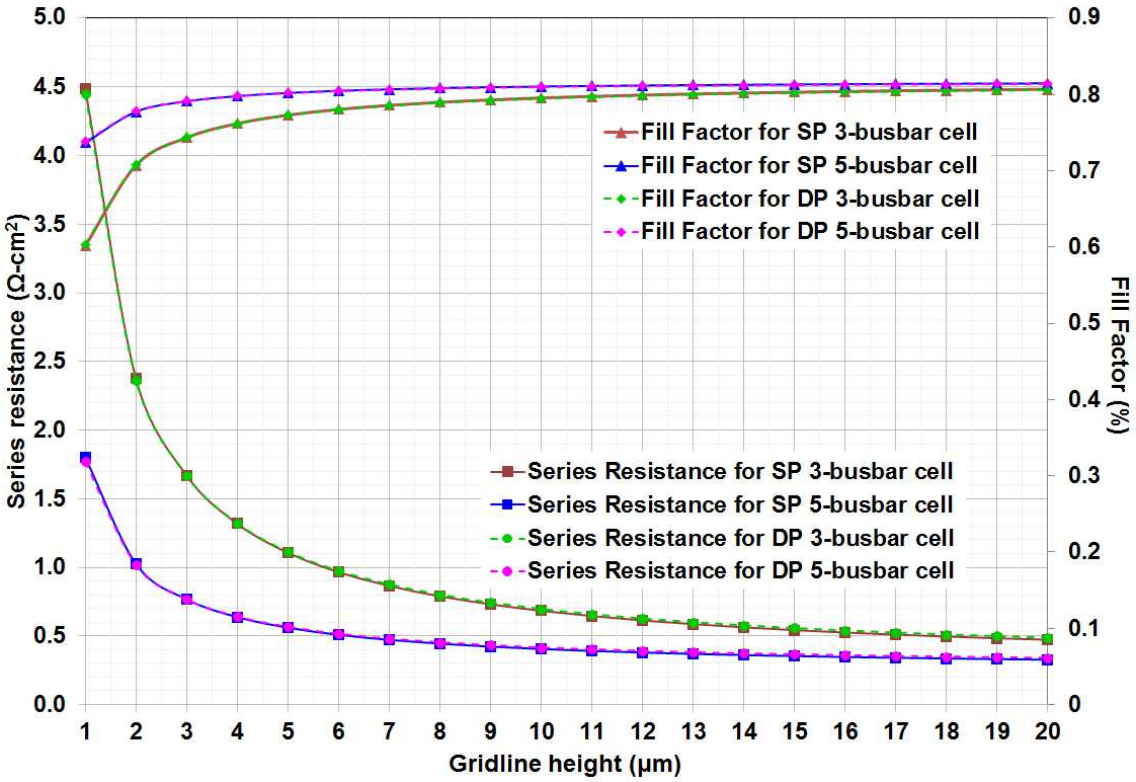

Figure 4.7: Plot of series resistance and fill factor vs. average gridline height for single- and double-printed solar cells.

In Figure 4.7, the series resistance and FF were plotted as functions of gridline height. As the gridline height increases, R_s decreases due to the reduced gridline resistance, resulting in improved FF. For SP and DP solar cells, the R_s and FF almost overlap as gridline height increases from 1 to 20 μm. This can be explained by the weak dependence

of R_s on the busbar component, as illustrated in Figure 4.3, although the double-printed busbar has smaller thickness than the single-printed counterpart. To achieve R_s of ~0.5 Ω-cm^2, average gridline height of 16 μm and 6 μm are required for 3- and 5-BB cells, respectively. While to achieve R_s of ~1 Ω-cm^2, 6 μm and 2 μm are required for 3- and 5-BB cells, respectively. This shows that the 5-BB design is superior to the 3-BB counterpart in efficiency enhancement and cost saving.

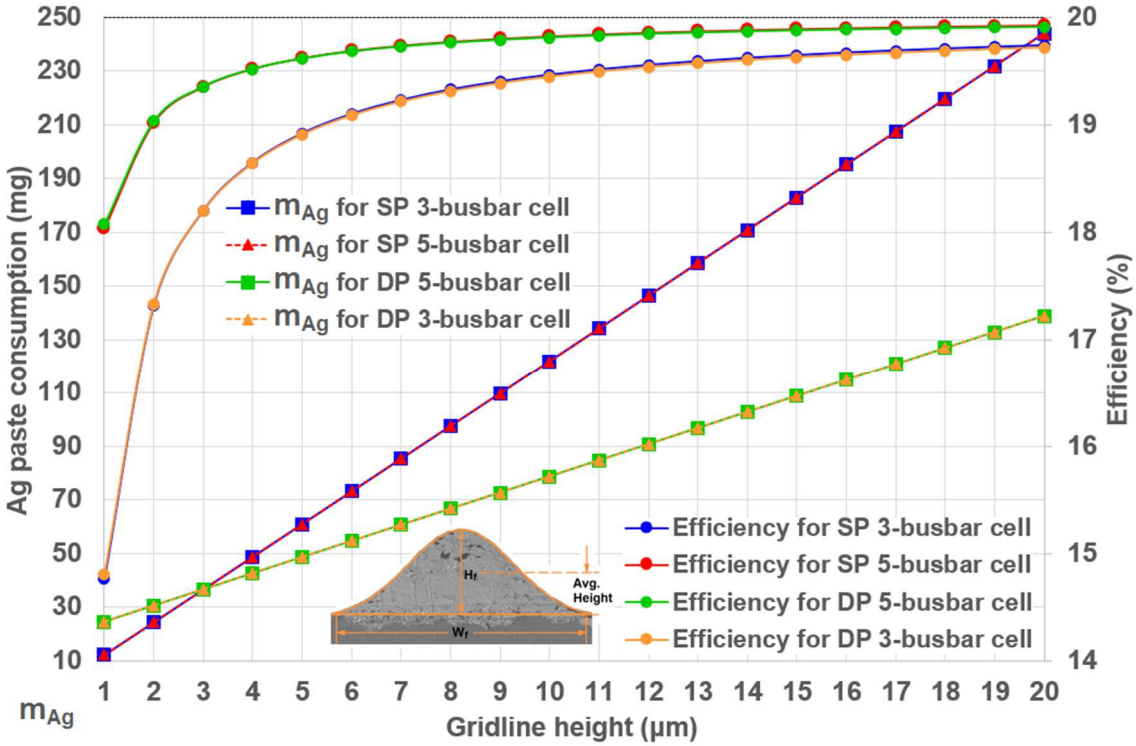

Figure 4.8: Plot of silver paste consumption (m_{Ag}) and efficiency vs. average gridline height for SP and DP solar cells.

Figure 4.8 shows the linear relationship between silver paste consumption and average gridline height. The efficiency is enhanced due to the resulting reduced series resistance by the increasing aspect ratio (height/width) of the gridlines. In addition, the shading fraction has no influence because the gridline width and number of busbars and gridlines are kept constant. And similar efficiencies were found for both SP and DP cells

as the gridline height varies. This could be explained by the similar output of R_s and FF as the gridline height varies for SP and DP cells (Figure 4.7). However, the great difference in silver paste consumption indicates that DP is superior to SP in terms of metallization cost savings. Therefore, if the saving in metallization outweighs the additional fabrication cost, DP should be implemented in solar cell metallization.

The efficiency curves in Figure 4.8 also show that after some points, the effort to continue to increase the gridline height will not be paid off considering the metallization cost. Apparently, there is no significant enhancement in efficiency after ~14 μm for 3-BB cell, and ~6 μm for 5-BB counterpart, so it is not necessary to pursue higher aspect ratio after these points. It is worth mentioning that with 5 μm gridline height, the double-printed 5-BB cell can achieve a conversion efficiency of ~19.6%, with silver paste consumption of only ~50 mg.

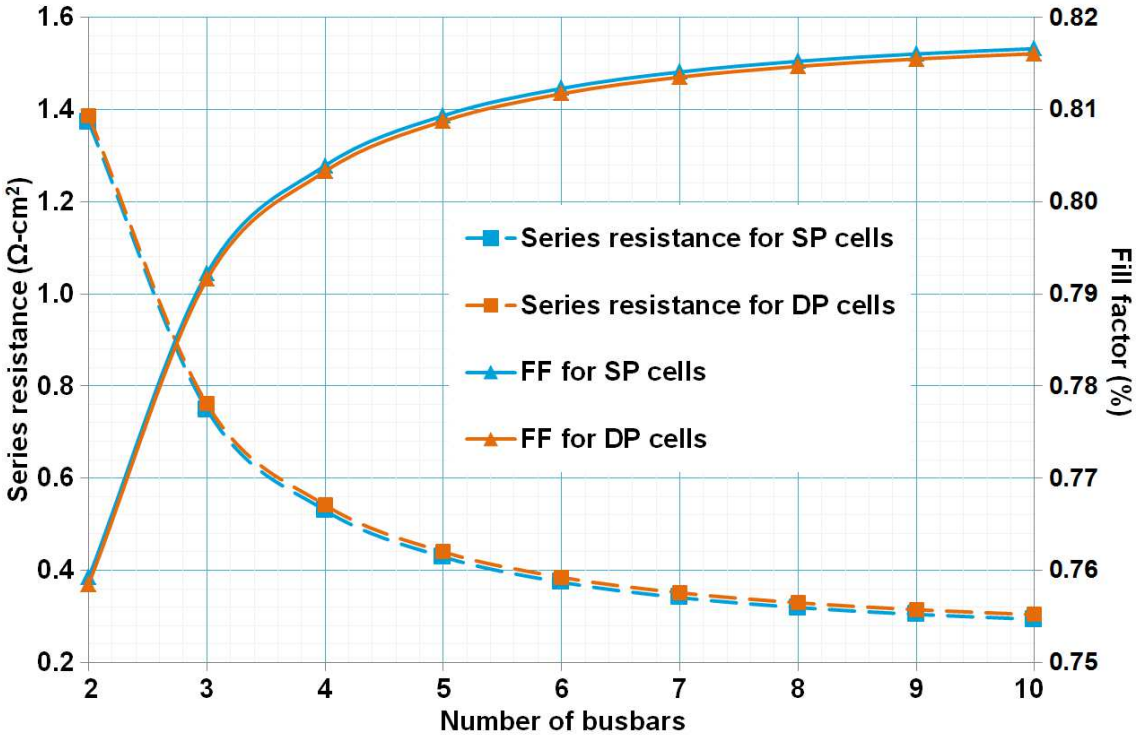

Figure 4.9: Plot of series resistance and FF as functions of the number of busbars for SP and DP cells. Total busbar coverage is fixed at 4.5 mm x 154 mm.

In order to investigate the impact of SP and DP on cells with different number of busbars, series resistance and FF are plotted as functions of the number of busbars, as shown in Figure 4.9. It is apparent that as the number of busbars increases, the differences in the values of series resistance and FF between SP and DP cells are negligible. This is because the busbar component is still much smaller compared to the total series resistance, although the series resistance significantly decreases as the number of busbar increases.

4.3.4 Evaluation of Metallization Cost (¢/W)

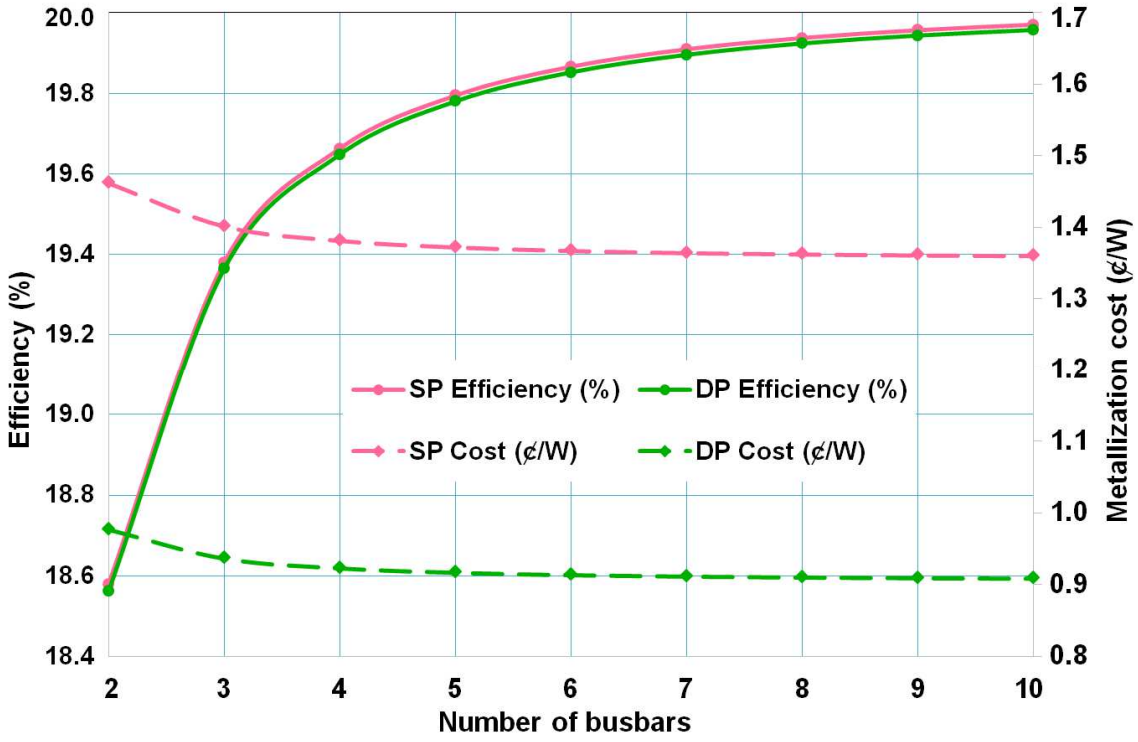

Figure 4.10: Efficiency and metallization cost as a function of number of busbars for single- and double-printed cells. Total busbar coverage is fixed at 4.5 mm x 154 mm.

Figure 4.10 shows the metallization cost and efficiency as a function of the number of busbars. It is apparent that as the number of busbar increases the corresponding silver cost slightly reduces until after five busbars, the cost tends to be constant. Notice also that the change in the number of busbars does not necessarily impact the cost from 2-BB cell

to 10-BB cell. However, with the similar cost, ~1.22% improvement in efficiency is observed as the number of busbar increases from two to five, and ~0.18% improvement from five busbars to ten busbars. This demonstrates that increasing the number of busbars contributes to achieve cost-effective high-efficiency solar cells.

More so, with almost the same resulting efficiencies, SP and DP cells show significantly different metallization cost. For a single-printed 5-BB cell, the metallization cost is ~1.37 ¢/W, while for a double-printed 5-BB cell, the cost is ~ 0.92 ¢/W, which saves about 33% of the amount of silver paste. This indicates that busbar thickness should be kept as low as ~3 μm for cost saving in the fabrication of solar cells.

4.4 Chapter Summary and Conclusions

In this chapter, computer modeling was carried out to study the optimum number of busbars to obtain low-cost and high efficiency industrial Al-BSF silicon solar cells. The simulation inputs includes experimentally measured electrical data from reference cell, geometries of metal electrodes (height and width of busbar and gridline, number of busbars and gridlines), and recombination parameters, etc. Based on the inputs, metal coverage and R_s were calculated accordingly to determine the modeled I-V data and metallization cost. It was demonstrated that compared to the state-of-the-art 3-BB Al-BSF solar cell design, multi-busbar (number of busbars >3), particularly 5-BB cells have great potential to increase FF and cell efficiency, and reduce metallization cost. With more busbars incorporated in solar cell design, gridline resistance would decrease due to the reduced effective gridline length. For a regular 3-BB solar cell design with gridline width of 50 μm, 75 Ω/□ emitter and ~90 gridlines should be implemented for high FF of ~0.80. Keeping the same busbar coverage (4.5 mm x 154 mm), a close correlation of R_s and gridline

resistance was found as the number of busbar increases. The corresponding efficiencies and FF improvement from two busbars to three busbars, and from three busbars to four busbars tells the evolution of metallization technologies for conventional silicon solar cells to some extent. This indicates that the advantage of multi-busbar solar cells, particularly 5-BB cell, should be taken by solar companies in the production line. The metallization analysis shows that using more busbars in the solar cell design is beneficial for cost saving. For the double-printed 5-BB solar cell, it is possible to implement the existing solar cell process and save ~33% of the printed silver paste compared with single-printing.

CHAPTER 5: EXPERIMENTAL VALIDATION OF MULTI BUSBAR AL-BSF SOLAR CELL

5.1 Introduction

The fabrication of Al-BSF cell involves several steps including emitter formation, deposition of ARC layer of SiN_x, front and back metallization, and contact co-firing. In chapter 2, the Al BSF was investigated; in chapter 3, the importance of emitter sheet resistance and uniformity was analyzed; and in chapter 4, the incorporation of these two important steps along with the front metallization was considered. In this chapter, the screen-printed 3-, 4- and 5-BB cells are fabricated and compared. To achieve high efficiency screen-printed cells with excellent fill factor, the uniform and repeatable fine-line printing is the key unit process step in addition to high quality emitter. The gridlines must be continuous and narrow to reduce shading and series resistance. Therefore, emphasis in this chapter is placed on printing narrow and continuous gridlines to improve both the FF and J_{sc} and hence the efficiency. After continuous and fine gridlines are achieved, the contact sintering was also investigated to ensure the ideality factor stays within the regime that does not degrade the cells.

Therefore, in this chapter, the process sequence for an Al-BSF cell fabrication is first enumerated followed by the printing optimization, then the firing of the contacts. The contact formation and current transport mechanisms for the screen-printed contacts were reviewed to understand the impact of contact co-firing on solar cell performance. And the experimental results were showed to validate the predictions by modeling.

5.1.1 Al-BSF Solar Cell Processing Sequence

The fabrication of Al-BSF Si solar cell usually consists (i) saw damage removal/texture, (ii) $POCl_3$ diffusion, (iii) PSG removal, (iv) edge isolation, (v) front deposition of PECVD SiN_x, (vi) metallization (print/dry back Al and front Ag pastes), and then (vii) co-firing of the back and front metal contacts. In this work, the first steps were carried out at Motech in Taiwan on their production line. This was followed by the back and front screen-printed metals at UNC Charlotte Photovoltaic Research Lab (PVRL) before the contact co-firing step. The 3- and 5-BB cells were printed with Al on the back side and Ag on the front side followed by the co-firing after profiling of the belt furnace to ascertain the peak temperature and dwell time.

5.1.2 Screen-Printing Metallization Process

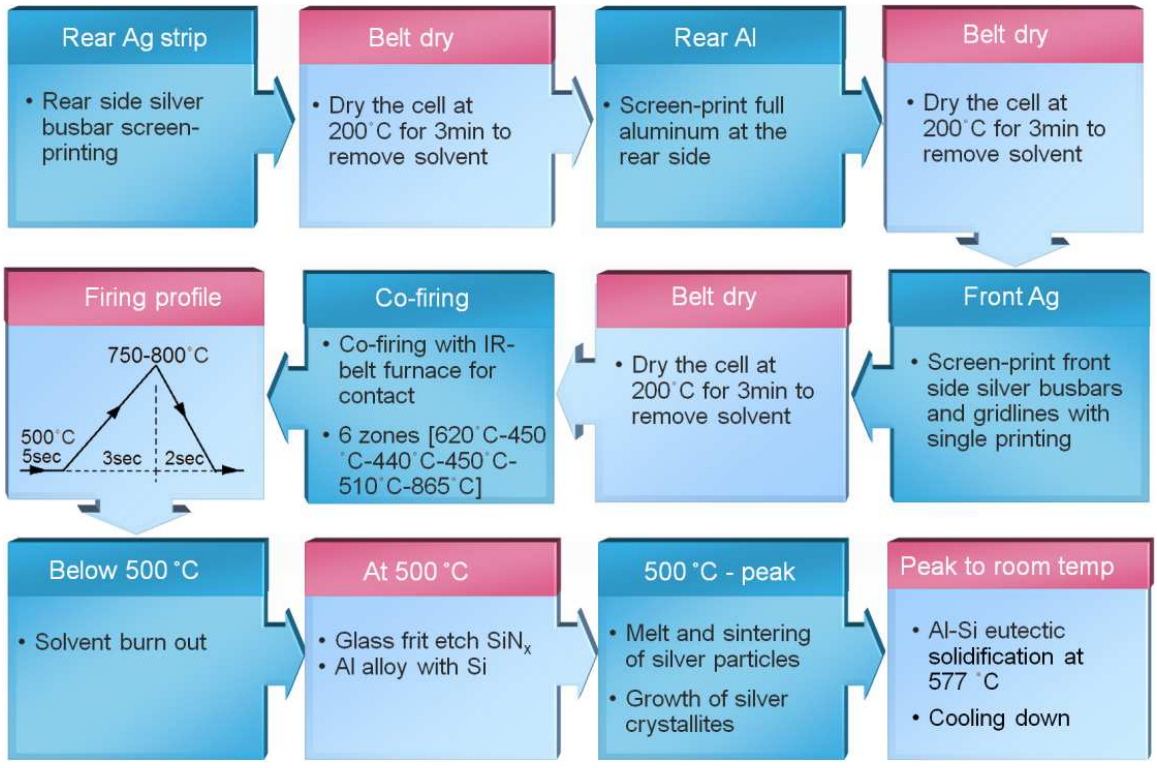

Figure 5.1: Processing details of screen-printing and firing in PVRL.

5.1.2.1 Overview of Screen-Printing

The screen-printing technology, which was first developed in the 1970's [94], is the most mature, best established solar cell metallization technology. The key advantages of screen-printing are low-cost, high-throughput, and the relative simplicity of the process compared with other technologies. The basic principle of the screen-printing process is simply the use of a mesh screen to reproduce the same pattern over and over again on Si wafer with metal paste. A schematic of the screen-printing process is demonstrated in Figure 5.2.

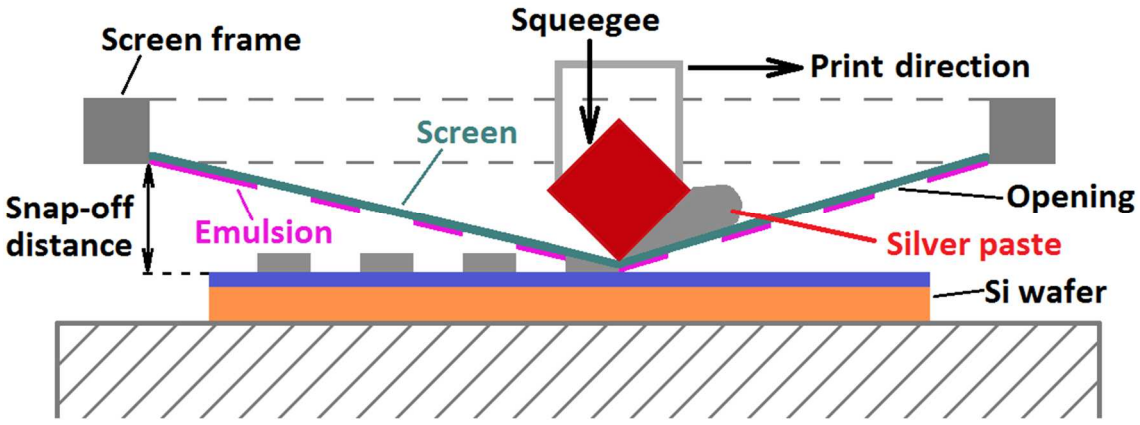

Figure 5.2: A schematic of the screen-printing process.

During the practical printing, paste is first applied to the screen before the movement of squeegee. As the squeegee moves the paste across the screen, a shearing action causes a decrease in viscosity, allowing the paste to pass through the open patterned area to the desired Si substrate. As the squeegee passes, the screen peels away and the paste viscosity recovers, leaving a well-defined print [95]. With no voids in the finished print, the printing process can be repeated as many times as the tension of screen materials does not affect the uniformity of printing. The main factors that influence the printing quality are snap-off distance, squeegee pressure, printing speed and range, attack angle, screen

resolution, and the viscosity of the paste, etc. The paste fundamentals are introduced in details as below.

5.1.2.2 Metallization Pastes

Metallization paste is a uniformly dispersed mixture with several organic and inorganic constituents such as metal particles, glass frit, solvent and binders, etc. A good paste for thick film metallization requires (i) moderate viscosity for good printability and high aspect ratio of printed metal grid, (ii) high lateral conductivity of printed gridline, (iii) low contact resistance between metal and silicon after appropriate firing, (iv)wide firing window to avoid variation in firing temperature, and (v) good solderability and mechanical adhesion for long-term stability.

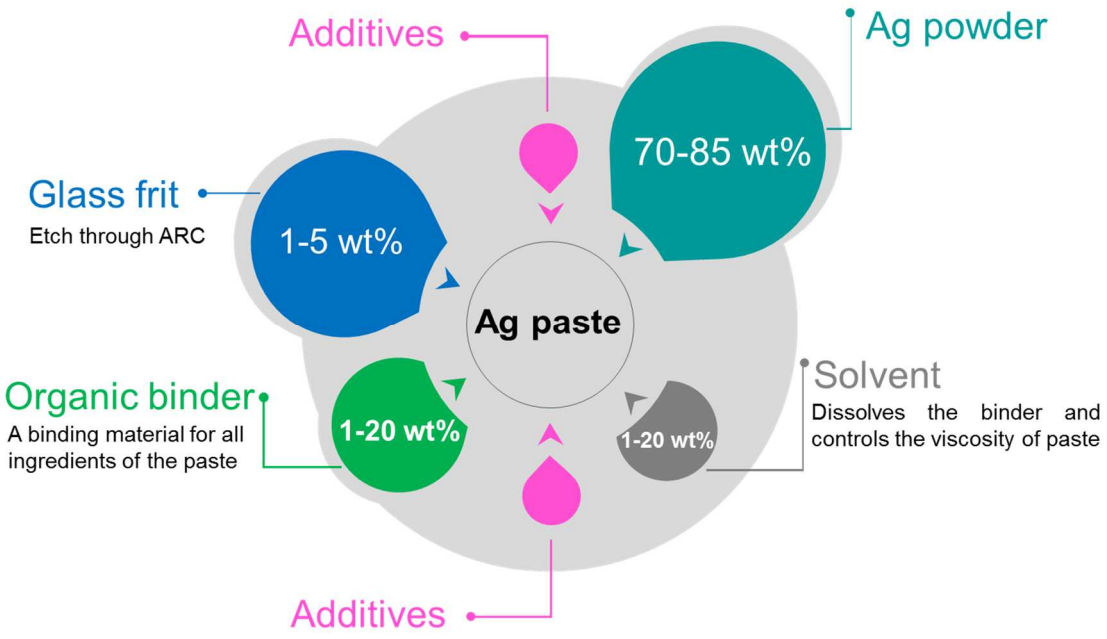

Figure 5.3: Typical front silver paste compositions [97].

Basically, a thick film paste mainly composes two groups of constituents, with one group controls the printing properties, and the other group determines firing properties and the solar cell performance. The former consists of an organic binder, typically ethyl

cellulose, and additives such as plasticizer, wetting agent, and thixotropic agent. The latter consists of fine metal powder as a conductive powder to provide electrical characteristics, and glass frit as a vehicle to etch ARC layer and transfer Ag particle from Ag bulk to Si [96]. Typically, the Ag paste contains 70-85 wt% of silver powder, 1-5 wt% of glass frit, 1-20 wt% of additives, and 1-20 wt% of organic binder, as shown in Figure 5.3 [97-98].

Every entry in the paste has its own function but it is the systematic combination of all elements that differentiates the performance of one paste from another in terms of different paste compositions. However, glass frit is most likely the determinant characteristic of a paste due to its responsibility for etching ARC layer and making contact between Ag bulk and Si substrate.

5.1.2.3 Screen Design and Fabrication

For screen-printing, the screen design is important to achieve desired gridline width and height. Since the front metal shadowing is defined by the screen mesh, therefore it is crucial to optimize the screen design such that both metal shadowing and series resistance can be minimized. The screen design can be done by some graphical design software such as Auto CAD and SolidWorks. The key features of a designed screen are characterized mainly by screen size, geometries of busbar and gridline openings, busbar and gridline spacing, and edge isolation, etc.

The fabrication of screen is usually done first by stretching stainless steel wire mesh cloth across the screen frame (10*10 inches in size for industrial application) and attaching it, maintaining high tension of the mesh. An organic light-sensitive emulsion layer is then spread over the entire mesh, filling all the open areas. Subsequently, the coated screen is exposed to a powerful UV lamp with the desired positive image blocked, which makes the

exposed area hard. Finally, the blocked areas are washed out, and the area to be screen-printed is then patterned on the screen [95], as shown in Figure 5.4.

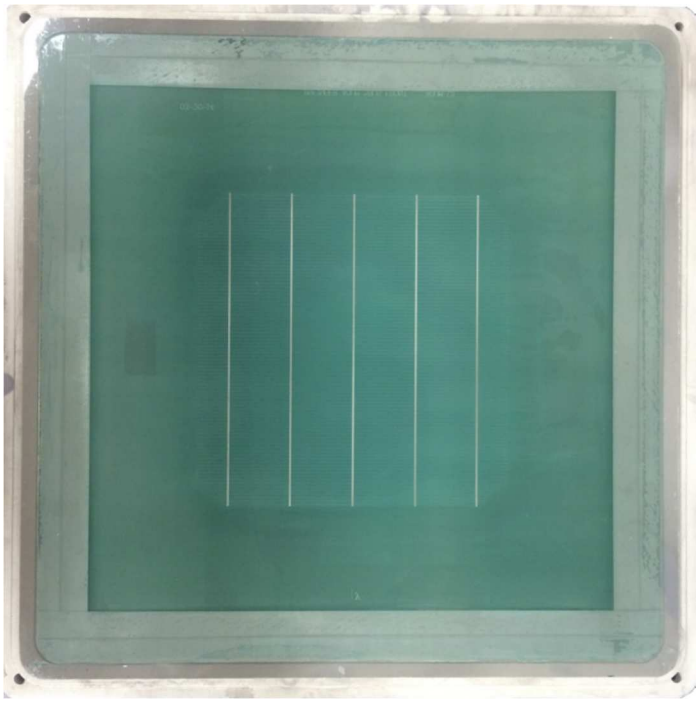

Figure 5.4: A practical 5-BB screen with 40 µm line opening fabricated by Sefar.

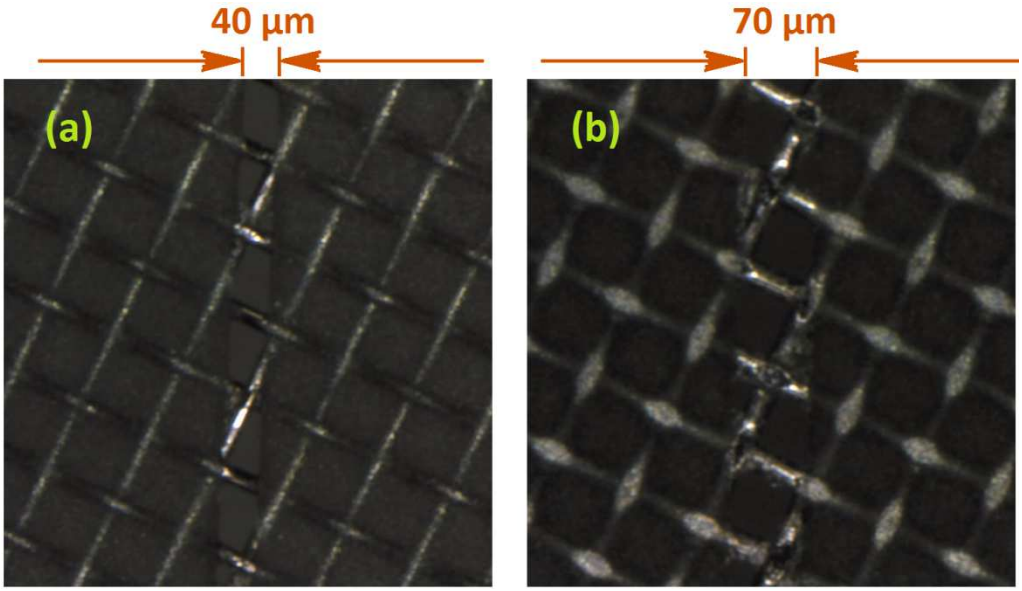

Figure 5.5: Different mesh openings of 40 µm and 70 µm in the screen design.

In order to achieve fine-line printing, it is very critical to design finer mesh opening in the screen. Currently in industry, the screen-printing with line opening of 60-70 μm are well established to achieve uniform printing and good repeatability to obtain stable cell efficiencies. In order to achieve ~50 μm gridline width, the line opening was decreased to 40 μm in our screen design compared to the 70 μm counterpart, as demonstrated in Figure 5.5. However, it gets much more challenging to attain high quality printing with finer line openings. Therefore the screen-printing needs to be thoroughly understood so as to optimize the printing process for uniform high resolution prints with great repeatability.

5.1.2.4 Path to Fine-line Printing

As modeled previously, it is very critical to achieve fine line features (e.g. ~50 μm gridline width) with screen-printing to obtain high efficiency solar cells. However, fine-line printing is still considered as a challenging technology in industry nowadays. In order to yield high resolution screen-printed metal grid with great uniformity and repeatability, and high throughput in the metallization process, the factors that influence the quality of screen-printing need to be investigated and controlled stringently in the experiment.

The current standard in industry for screen-printed Si solar cell includes printed gridline width of ~70-90 μm, and printed amount of Ag paste of ~90-120 mg. To be able to reach to fine gridline width of ~50-60 μm and printed Ag paste of ~70-80 mg for high-efficiency cost-effective Al-BSF solar cells, all the parameters and concerns with screen, squeegee, silver paste and printing process need to be taken into account, as illustrated in Figure 5.6. After reviewed all the factors that impact the quality of screen-printing in the process, a few of them were considered to be important variables on achieving fine-line printing and were paid special attention in the experiment. They were squeegee balance

(the parallelism between squeegee and substrate), squeegee down-stop distance, snap-off distance, squeegee pressure, print speed and Ag paste viscosity.

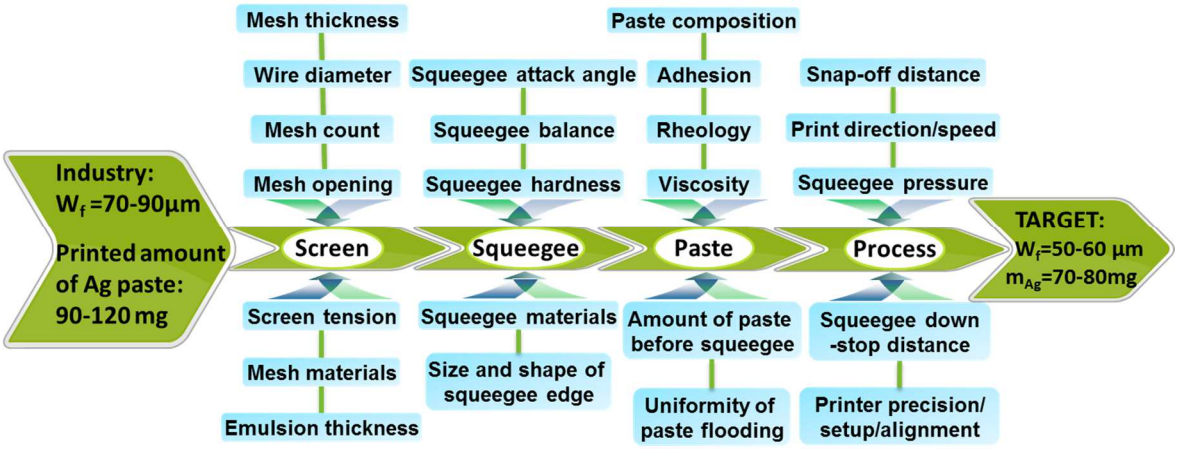

Figure 5.6: Factors that impact quality of screen-printing.

To obtain uniform transfer of Ag paste through the screen mesh opening, it is necessary to ensure great parallelism between the printing edge of the squeegee throughout the full printing stroke, and uniform flooding of the paste across the screen as the squeegee moves back the starting position. The squeegee down-stop distance and snap-off distance determine the printing force that applied to the squeegee during printing. The squeegee down-stop distance needs to be adjusted to the point that the printing force is just sufficient for the paste to pass through the mesh opening to the desired substrate. And the snap-off distance should be set to an appropriate value such that the screen tension will not be impacted after the printing stroke, and the screen can peel off the substrate smoothly to enhance the gridline height. The squeegee pressure should be just enough to wipe the mesh opening area free of Ag paste to ensure narrow printed gridline width. Excessive squeegee pressure will result in wider gridline width and might also cause some non-uniform prints near the edges of the substrate. In addition, the viscosity of Ag paste also strongly impacts

the quality of printing. Depending on the viscosity, the squeegee pressure and the print speed need to be customized to guarantee stable transfer of Ag paste to the substrate.

The important characteristics of the printed gridline are gridline height and width. Generally, high aspect ratio (defined as height/width) of gridline can be achieved with large snap-off distance, low squeegee pressure, low print speed and high viscosity of the paste, provided these conditions give good transfer of Ag paste to ensure continuous gridline and high throughput in cell processing.

The printed metal grid pattern may be blemished by gridline breakage, smearing, or non-uniform prints with raggedy gridlines. Usually, gridline breakage can be caused by (i) high viscosity of paste, (ii) low squeegee pressure, (iii) high print speed, or (iv) blocked mesh openings. Smearing occurs because of (i) too much paste loaded before squeegee, (ii) too low viscosity of the paste, (iii) too small snap-off distance, (iv) too low print speed, (v) too high squeegee pressure, or (vi) dirty screen on the side in contact with substrate due to bad peel off with the previous printing. Therefore it is important to monitor the printed gridlines and wipe the screen with a dry wiper if any smearing occurs. Non-uniform prints can result from (i) lack of parallelism between screen and substrate, (ii) insufficient paste on the screen, (iii) inadequate squeegee pressure, or (iv) too high paste viscosity. More so, a worn squeegee blade can also cause problems in printing, thus a hard squeegee with good blade should be implemented in printing.

In the experiment, in order to achieve high quality printings with the 40 μm opening screen, the print settings were customized based on the well-developed settings for the 70 μm opening screen. The adjustments mainly come from reduced snap-off distance, increased squeegee pressure, slowed print speed and slightly lowered squeegee down-stop

distance. And these parameters need to be changed if another paste of different viscosity is used.

5.1.3 Contacts Co-firing

Figure 5.7: The commercial inline IR-belt furnace by TP Solar.

It is well known that the performance of industrial silicon solar cells have a strong dependence on the final co-firing step because during co-firing [96], (i) the contact between printed metal grids and Si wafer is made, (ii) printed gridline resistance is reduced due to sintering process, and (iii) Al BSF is formed. All of the above mentioned activities with the firing process contribute to the improvement of R_s, FF and hence the overall solar cell efficiency. The typical firing profiles for the commercial inline IR belt furnace (Figure 5.7) used in the experiment are shown in Figure 5.8.

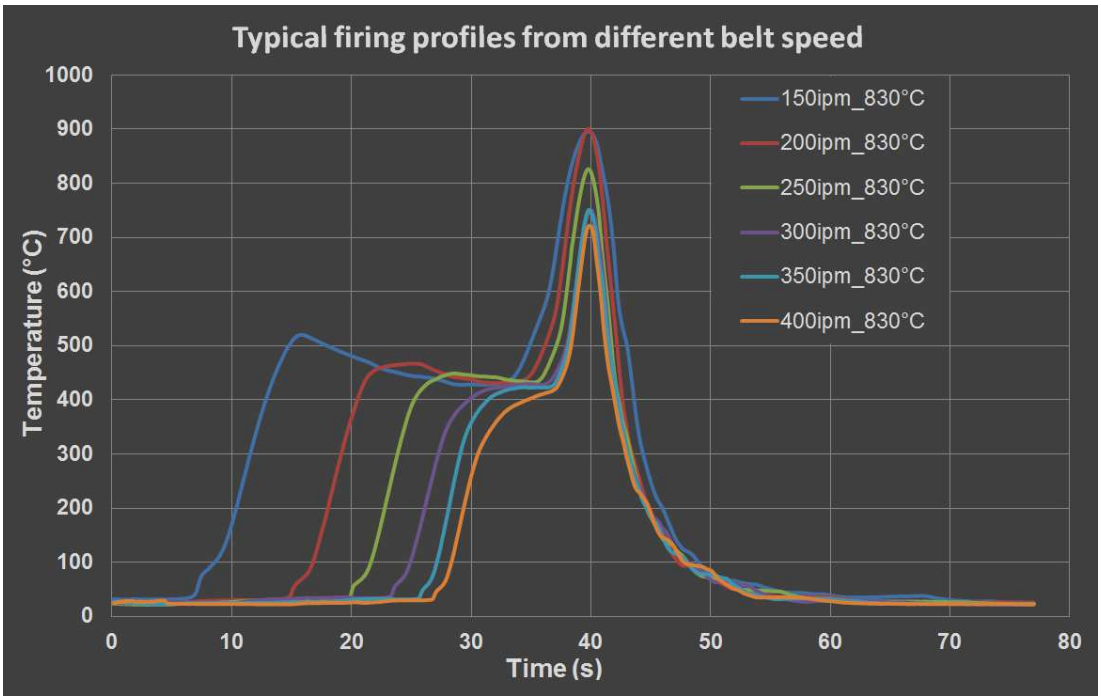

Figure 5.8: Typical firing profiles for conveyor-belt furnace with different belt speeds ranging from 150 to 500 inches per minute (IPM). The set point of peak firing temperature is 830°C.

Basically, contact-firing is a 3-step process, which includes burn-out, sintering and cooling. The burn-out process is done at temperatures in the range of 300-400°C to drive out the organic binders. The firing step happens at temperatures in the range of 700-800°C for the contact formation and liquid phase sintering of metal particles. And the cooling step takes action in the temperature range of <600°C for the formation of Al BSF during eutectic solidification at the back side of the cell [93].

5.1.4 Mechanism of Contact Formation and Current Transport

Screen-printed Ag contacts are commonly used for the thick-film metallization of crystalline Si solar cells on account of its cost-effectiveness compared with other metallization technologies. For the p-type Si substrate, the front metal grid is usually screen-printed on the $POCl_3$ diffused n^+-emitter coated by a SiN_x antireflection layer. After the screen-printed cell being dried at ~200°C for 2-3 minutes, a stable ohmic metal-silicon

contact can be obtained by firing the printed cell with an optimal firing profile, which is characterized by fast temperature ramp-up (>100°C/sec) and ramp-down rate (>150°C/sec), short dwell time (1-3 seconds), and optimal peak temperature (750-800°C). Depending on the firing condition, the metal contact can be under-fired, which leads to a poor opening of the SiN_x layer, or over-fired, which results in a rather thick glass layer with over-grown Ag crystallites that would cause a low shunt resistance[96]. The silver paste composition in terms of silver particle, glass frit, and organic binder, etc., is critical for high-quality electrical and mechanical contact formation.

5.1.4.1 Contact Formation Mechanism

The glass frit plays a crucial role in etching through the SiN_x ARC to react with n^+-emitter during contact formation, which enables the nucleation of Ag crystallites at the glass/Si interface to form an ohmic metal-Si contact with the emitter [99-104]. In addition, the glass frit dissolves several percent of Ag, and improves the sintering process of fine silver particles for the growth of silver crystallites during contact firing [96]. To obtain a detailed understanding of the formation and growth mechanism of these Ag crystallites, several studies have been reported to investigate the role of a lead borosilicate glass frit in Ag paste during contact formation [74, 99-105]. The understanding of Ag crystallites growth at the glass/Si interface is largely based on the model proposed by Schubert et al. [103]. In this model, metallic Pb precipitates are first formed by a redox reaction between Si and the PbO in the fluidized glass frit during heating-up. Subsequently, the precipitated Pb severs as a transport medium for Ag to diffuse from the bulk of printed silver paste to the glass/Si interface. The epitaxial growth of Ag crystallites into the Si is then completed upon fast cooling-down process. However, this model appears to be incompatible with

lead-free metallization paste [106], and also with the observations of vanished Pb precipitates around the grown Ag crystallites [100, 103]. To further investigate the growth mechanism of Ag crystallites, Hong et al. [107] found that, in contrast to the model proposed previously, the Ag crystallites are formed by a direct reaction between the Ag^+ ions dissolved in the glass frit and the Si wafer without the aid of Pb precipitates. The formation of Pb through a redox reaction between the PbO and Si or SiN_x will be suppressed when a few weight percentage of of Ag particles are dissolved into the glass frit. However, the size and distribution of the inverted pyramidal Ag crystallites formed at the glass/Si interface are found to have critical dependence on the PbO content in the glass frit.

5.1.4.2 Current Transport Mechanism

The glass layer at the interface of Ag/Si is often assumed to be insulating and hence responsible for high contact resistance. Because the glass layer separates the Ag crystallites from the Ag bulk, in order to understand the current transport path between Ag crystallites and Ag gridline, many studies have been carried out. The current transport mechanism is predominately explained by two different theories. The first one suggests that the current flows mainly through the sparsely distributed Ag crystallites grown into the silicon emitter, which are either directly connected to the silver bulk or separated from the silver gridline by an ultrathin glass layer [99, 101, 108-109]. The second one proposes that nano-Ag-colloids are formed inside the glass layer during firing, which allows the conduction to the silver bulk through multi-step tunneling [110-111]. By liquid conductive Ag experiments, Schubert et al. [112] subsequently established that both theories may be valid, but the current flow is dominated by the contribution of the conduction from the Si emitter to the

Ag bulk via Ag crystallites in direct contact which are mainly located at the Si pyramids tips.

5.2 Experimental Validation of the Innovative Front Grid Designs

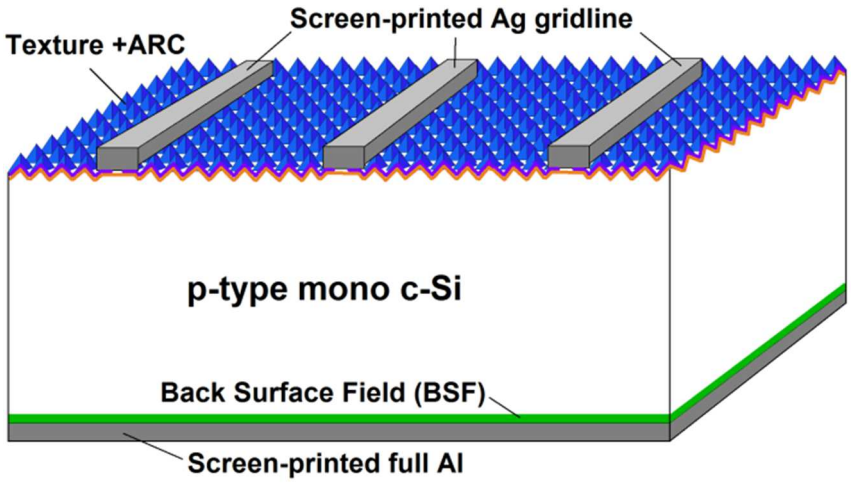

Figure 5.9: A schematic structure for conventional 3-BB cell with full Al-BSF.

Table 5.1: Overview of the screen-printed cells from three groups

Group	Type	Gridline width	Busbar width	Number of gridlines	Back side
Group I	3-BB	~60 μm	1.5 mm	89	Full Al-BSF
Group II	4-BB	~60 μm	1.125 mm	89	Full Al-BSF
Group III	5-BB	~60 μm	0.9 mm	89	Full Al-BSF

In the experiment, cells with conventional 3-BB design are compared with those with 4- and 5-BB designs. All the Al-BSF silicon solar cells, as shown in Figure 5.9, were fabricated on p-type Czochralski (CZ) monocrystalline silicon substrates having resistivity of 2.0 Ω-cm, thickness of 180 μm and size of 239 cm^2, and $POCl_3$ diffused emitter with sheet resistance of ~80 Ω/□. The wafers were divided into three groups, as shown in Table 5.1. Group I is the conventional 3-BB reference group. And group II and III have the improved metal grid designs with four and five busbars, respectively. The screen-printing

process follows the settings as described in the modeling, and the gridline width of 50-60 μm was achieved by a screen with 40 μm mesh opening. The rear side of the cells from all three groups was printed with full Al, as demonstrated in Figure 5.9.

In this part, the 3-, 4- and 5-BB monocrystalline Al-BSF Si solar cell were fabricated experimentally to verify the benefits of multiple busbars as shown in the modeling. This was done first by the design and fabrication of the screen with some screen manufacturer (e.g. Sefar, etc.), and then printing metal pastes on both the front and back side of the cell, and last firing the cells to make metal electrodes for I-V measurements.

5.2.1 Light I-V Measurements

Table 5.2: I-V measurements for cells from all groups

Group	V_{oc} (mV)	J_{sc} (mA/cm^2)	FF	Efficiency (%)
Group I-1	642	38.46	0.780	19.26
Group I-2	642	38.53	0.786	19.45
Group I-3	642	38.70	0.769	19.11
Group I-4	640	38.53	0.774	19.09
Group I-5	641	38.60	0.765	18.92
G-I average	**641.4**	**38.56**	**0.775**	**19.17**
Group II-1	642	38.49	0.791	19.55
Group II-2	641	38.60	0.795	19.67
Group II-3	641	38.54	0.792	19.57
Group II-4	642	38.65	0.788	19.55
Group II-5	641	38.47	0.794	19.58
G-II average	**641.4**	**38.55**	**0.792**	**19.58**
Group III-1	641	38.47	0.802	19.76
Group III-2	641	38.57	0.804	19.89
Group III-3	641	38.56	0.801	19.82
Group III-4	642	38.63	0.804	19.94
Group III-5	640	38.55	0.801	19.76
G-III average	**641.0**	**38.56**	**0.802**	**19.83**

For the I-V measurements, the V_{oc}, J_{sc}, FF and efficiencies for the 15 cells from three groups with five from each group are summarized in Table 5.2. It shows that the efficiencies for the 3-BB cells are in the range of 18.92%-19.45% with average fill factors

of 0.775, compared to 4- and 5-BB cells with efficiency range of 19.55%-19.67% and 19.76%-19.94%, and average fill factors of 0.792 and 0.802, respectively. Because the TBW for all the cells are the same, so cells from all groups have similar front metal shadowing and surface recombination, which explains the negligible variation in V_{oc} with the change in the number of busbars. However, due to the decreased resistive loss with gridlines as demonstrated in the model for the 4- and 5-BB cell, the experimental cells showed enhanced performance in J_{sc} and FF as the number of busbar increases, which results in higher conversion efficiency. A closer observation reveals that the average of measured I-V data for all the three groups is actually in good agreement with the modeled values. This indicates that multi-busbar cell design concept has the capability to improve solar cell efficiency without any additional cost, assuming all the fine gridlines are well printed with great uniformity from gridline to gridline, and from cell to cell.

Figure 5.10 shows the best 5-BB Al-BSF cell with V_{oc} of 642mV, J_{sc} of 38.63 mA/cm^2, FF of 80.4%, and the conversion efficiency of 19.94%. The fundamental strategy to achieve the high conversion efficiency in Al-BSF cells has not been changed for years, which includes (i) improving the surface passivation to increase V_{oc}, (ii) optimizing the grid electrodes to suppress the shadowing and resistive losses to increase J_{sc}, and (iii) decreasing the resistance loss to increase FF. The V_{oc} of the conventional Al-BSF cell has been consistently increased step by step with improving surface passivation techniques over the year. The high V_{oc} of ~642 mV achieved in our cells demonstrates the excellent surface passivation quality of the Al-BSF structure.

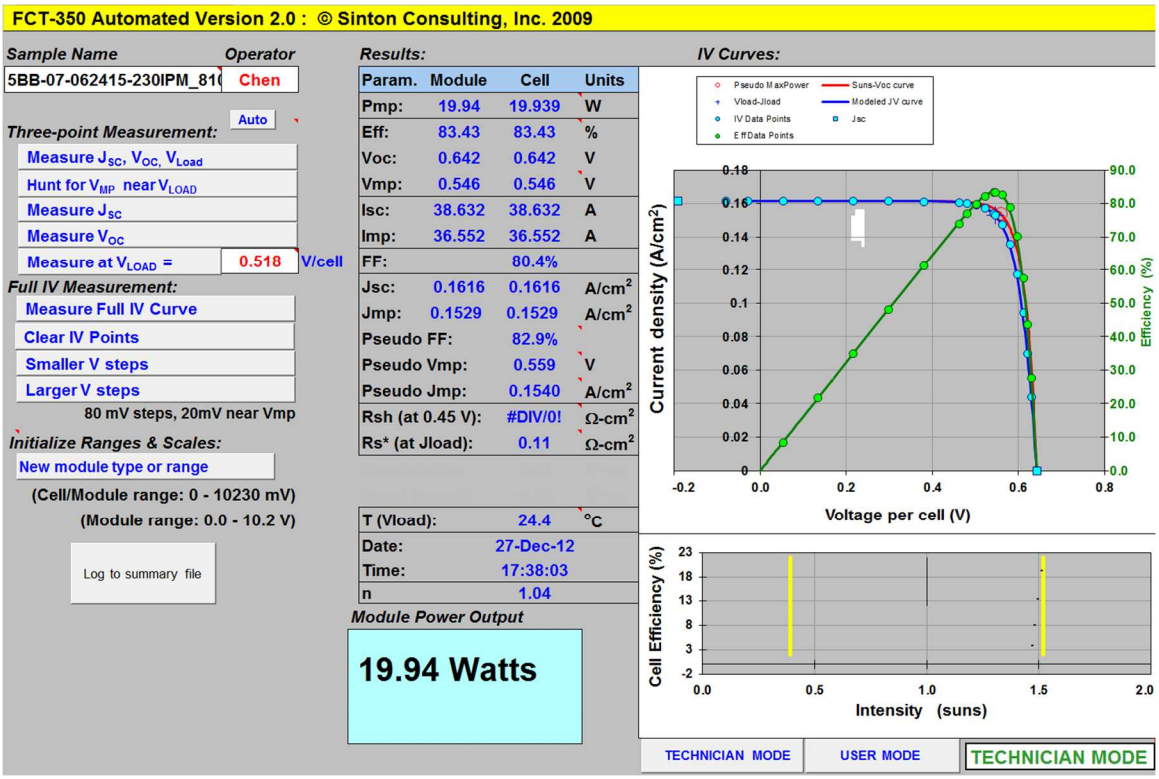

Figure 5.10: I-V data for the best 5-BB solar cell with 19.94% conversion efficiency.

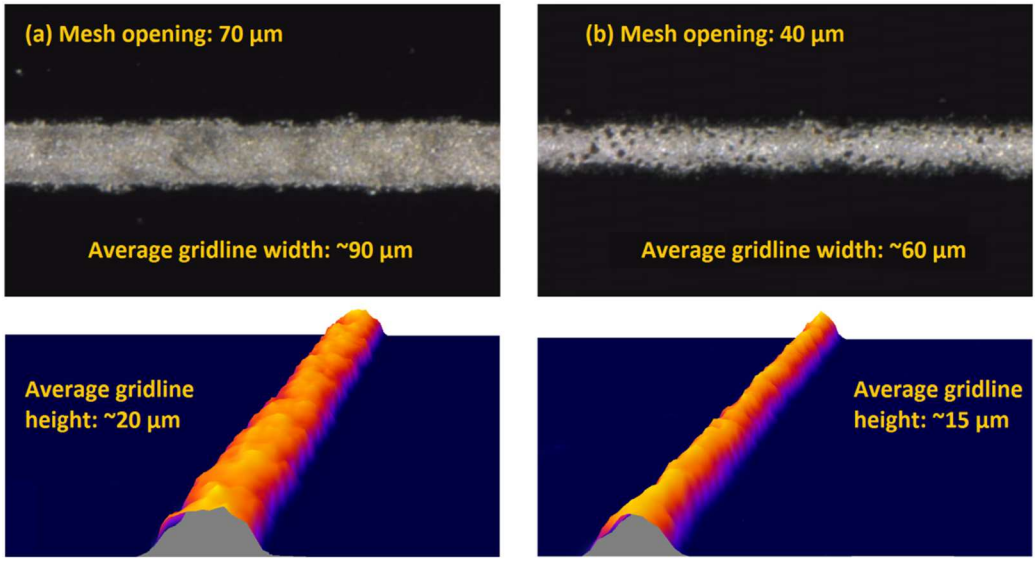

Figure 5.11: Images of front gridlines by digital microscope and the corresponding 3D profiles.

For the both side contacted 5-BB cells, the shadowing loss by the electrode on the front surface of the cell is the main factor that restricts the J_{sc} to <39 mA/cm^2. By

implementing fine-line printing in the 5-BB cells, both the shadowing and resistive losses by metal gridlines can be reduced. Figure 5.11 shows the 2D and 3D gridline profiles for gridlines printed with different mesh openings of 70 μm and 40 μm that result in ~90 μm and ~60 μm gridline width, respectively. With ~60 μm width achieved for the 5-BB cell, one third of the metal shading by gridlines can be saved compared with the conventional 3-BB counterpart. This explains the highest average J_{sc} with the 5-BB cells. To further minimize the optical losses on the front surface, it is crucial to have good management of the optical path of light incidence on the front electrode at the entire module level rather than a specific cell. This seems to be the key that leads to further elimination of optical losses of the Al-BSF cell.

The FF is affected by both the junction property and the resistive loss associated with series resistance and shunt resistance. We tried to increase the FF by optimizing the firing condition to obtain good junction properties. And also achieved low series resistance to minimize the impact of series resistance on FF. The Ag paste used for Al-BSF cell was also optimized to realize finer lines to decrease the shadowing loss for higher J_{sc} and simultaneously ensure lower series resistance to increase the FF. Based on what was achieved for FF, it is very likely that the FF can be further increased to >0.81 with better metal grid design and higher quality printing.

We have made great effort to not only increase the conversion efficiency of the Al-BSF cell because the efficiency has great impact on the cost of solar electricity, but also to implement the simplest processing steps with relative low quality Si wafers compared to the IBC and HIT cells, because the wafer cost and cell fabrication cost are the main part of

the PV cost. From our analysis, there are still more possibilities for further raising the conversion efficiency by the introduction of gridline segmentation and uneven busbars.

5.2.2 Optimization of Contact Firing

In order to optimize the firing condition to achieve low contact resistance, low gridline lateral resistance and good junction properties, it is crucial to understand the process occurring during the firing cycle in a belt furnace. As demonstrated in Figure 5.12, the typical firing profile of the conveyor-belt furnace is characterized by the ramp-up and ramp-down rate, the peak temperature, and the dwell time (time above temperature of 600°C).

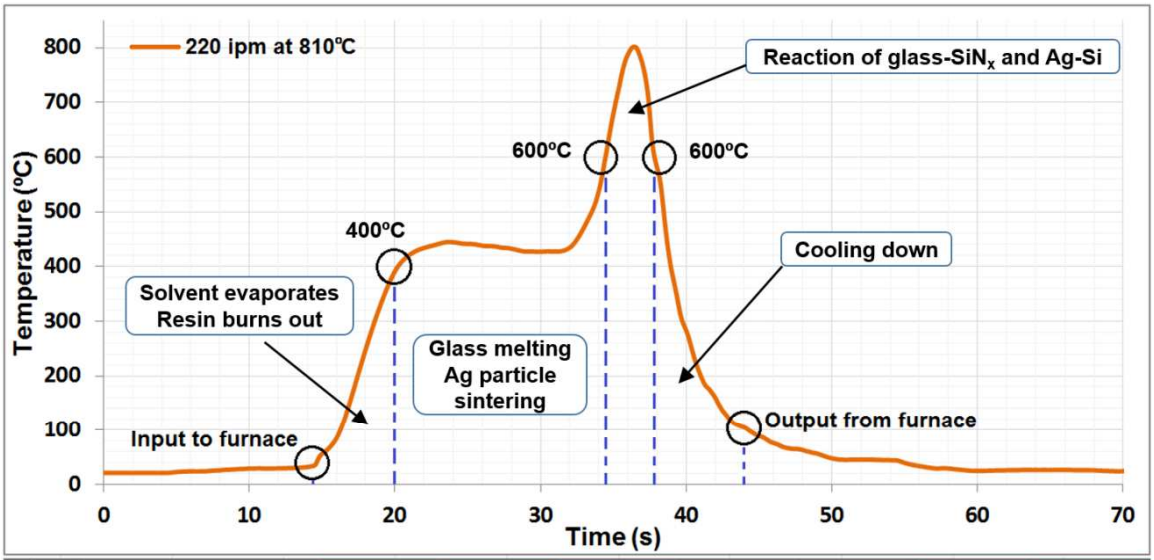

		Maximum Temperature	Maximum Positive Slope	Maximum Negative Slope	Time Between Temperature	Time Above Temperature: Rising (+)	Time Above Temperature: Falling (+)	Time Above Temperature: Total (+/-)
					390-430°C	600°C	600°C	600°C
Show All		°C	°C/sec	°C/sec	sec	sec	sec	sec
A2	Sensor 2 Location	801.7	127.83	-190.04	1.6	1.9	1.4	3.4
	Range	0.0	0.00	0.00	0.0	0.0	0.0	0.0
	Average	801.70	127.830	-190.040	1.60	1.90	1.40	3.40
	Std Deviation	-1.#IO	-1.#IND	-1.#IND	-1.#IO	-1.#IO	-1.#IO	-1.#IO
		Template: C:\ECD\MegamoleMAP\Template\DataTableCalculations.tpf						

Figure 5.12: A schematic of the firing profile for the conveyor-belt furnace with process occurring at different temperatures.

As the temperature increases from room temperature to 400°C, the resin burns out; between 400°C and 600°C, the melting of glass frit happens, and Ag particle sintering also occurs for the neck growth among Ag particles to reduce the porosity of the printed metal grids; during the dwell time (T >600°C), the molten glass together with some dissolved Ag particles etches the SiN_x ARC and reaches the glass/Si interface to react with Si. The dissolved Ag in the glass frit then precipitates onto the Si surface and grows into the Si to form Ag crystallites. To ensure optimal co-firing of the printed metal electrodes, it is critical to have fast ramp-up (> 100°C/sec) and ramp-down (< -150°C/sec) rates. Note that in our experiment, the firing profile implemented has a fast ramp-up rate of 127.83°C/sec, and a fast ramp-down rate of -190.04°C/sec, which contributes to the formation of front contact and back Al BSF. The peak temperature and the dwell time need to be adjusted based on the paste composition. Depending on the paste, the firing condition must be optimized to be compatible with the paste. For the Heraeus Ag paste used in our experiment, the peak temperature was tuned to ~800°C with a short dwell time 3.4 seconds to achieve good contact firing. To find the optimal firing profile that is within the firing window of the printed metal pastes, the mechanism of Ag particle sintering also need to be understood.

5.2.2.1 Sintering of Ag Particles

Basically, there are three types of sintering, solid state, transient liquid phase and liquid phase sintering (LPS). Of these three, LPS is applicable to the front Ag silver paste sintering because of the presence of the glass frit. The presence of molten glass frit remarkably accelerates the sintering rate due to rearrangement and coarsening processes in liquid phase. During the LPS, Ag particles start to grow neck among each other as soon as contacting points are formed to reduce the porosity in metal gridlines, as shown in Figure

5.13. The particles get reshaped by material transfer driven by the difference in free surface energy and the pressure difference across the curved surface to minimize the surface curvature and surface energy [96], which contributes to lower porosity and high conductivity in metal gridlines.

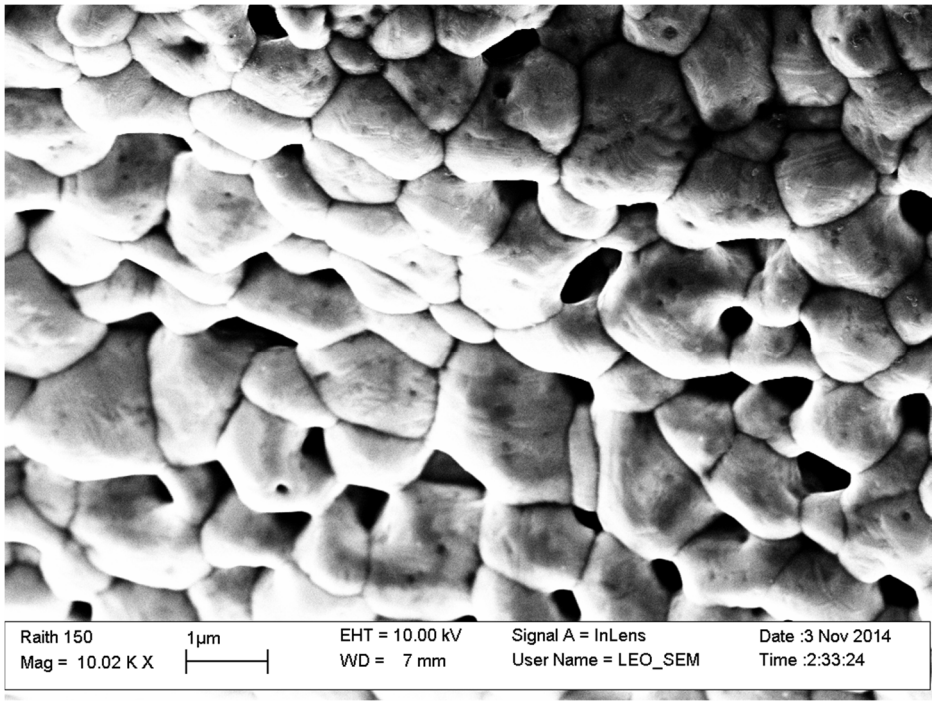

Figure 5.13: The E-beam lithography image of sintered Ag particles with reduced porosity.

Hilali et al. [73] reported that there is also an Ag particle size dependence of Ag crystallite formation, which is also explained by Herring's scaling law [113]. It is said that as the Ag particle size gets larger in the paste (in macro scale), the density of Ag crystallites formed at the interface is higher. However, during sintering, dissolution of Ag particles into the molten glass frit also takes place, which will form crystallites by precipitating into Si when cooling down. Ag particles get larger due to long firing time before the lead oxide (PbO) in glass frit reaches to ~580 $^{\circ}$C to be molten PbO which dissolves Ag particles in. So sintering should be correlated with the firing dwell time. To overcome this issue, either

Ag particle sintering must be slowed down by a sintering inhibitor, which requires another additive to the paste, or the dwell time should be decreased to lower the pace of sintering, which gives Ag particles a chance to be dissolved and hence precipitate into Si at Ag/Si interface. Therefore high belt speed (>200 IPM) should be implemented in the experiment to achieve low contact resistance with higher density of Ag crystallites between Ag electrode and Si substrate.

5.2.3 IQE Analysis

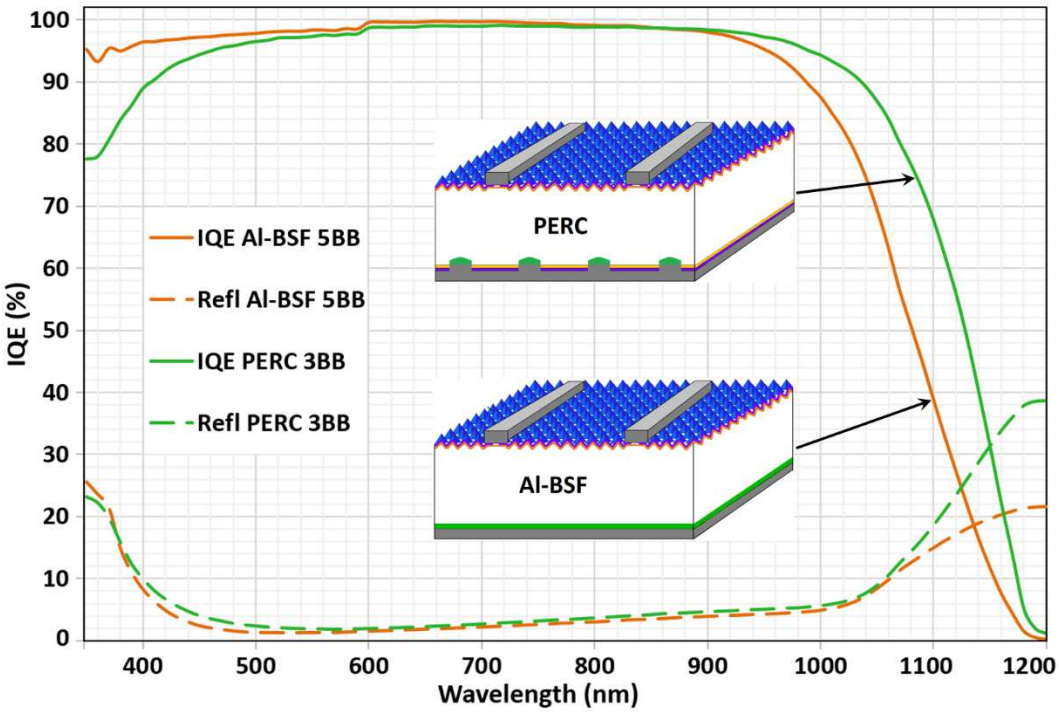

Figure 5.14: IQE analysis of the typical 5-BB cell of 19.76% efficiency compared to a 20.27% PERC cell.

To have a better understanding of the high performance 5-BB silicon solar cells, the IQE analysis was carried out for a typical 5-BB cell and compared to a PERC cell, as illustrated in Figure 5.14. It is obvious that due to the greatly improved surface passivation on the rear side, the PERC cell gains much better long wavelength spectral response than the 5-BB cell. However, the 5-BB cell has much superior blue response than the PERC cell

on the front surface of the cell. This tells that the doping and front surface passivation of the 5-BB cell is excellent for high solar cell performance, the strategies to further improve the cell conversion efficiency should be innovations on the front metallization to achieve lower R_s and metal shadowing loss, and the rear passivation to attain enhanced back reflectance and long wavelength spectral response. It is worth mentioning that the PERC cell used in the experiment should have doping problem that needs to be fixed to approach 21% conversion efficiency. And even higher efficiency of >21% should be expected if 5-BB metallization scheme can be implemented with the PERC cell.

5.2.4 Pseudo FF, V_{oc} and Parasitic (R_s, J_{o2} and n-factor) Mapping Using Suns-V_{oc} Measurements

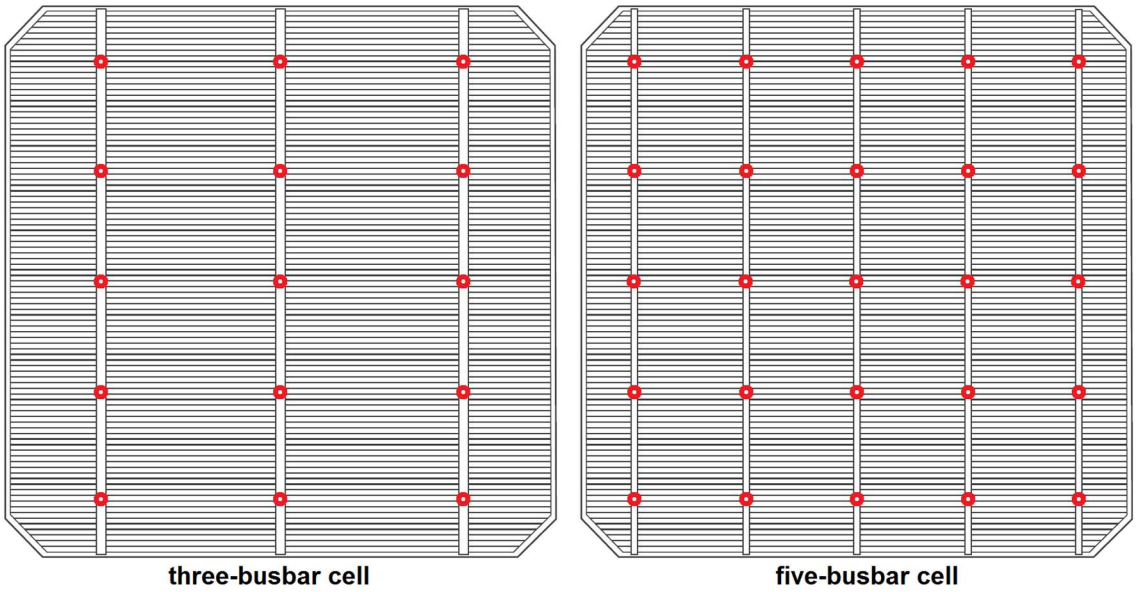

Figure 5.15: Multiple measurements by Suns-V_{oc} for both the 3- and 5-BB solar cells. The probe locations along the busbar are indicated by the small red circles.

To understand the factors that differentiate the performance of 5-BB cell from the 3-BB counterpart, Suns-V_{oc} measurement was taken for the typical 3- and 5-BB cells. To account for the non-uniformity in emitter that might cause variation in the measurement,

multiple measurements were taken along the busbars. The probe locations for all the measurements on the 3-and 5-BB are shown in Figure 5.15.

Table 5.3 summarizes the average Suns-V_{oc} data for the 3 and 5-BB cells. The ~650 mV V_{oc} on both cells confirms that both cells have similar metal coverage and hence same metal recombination. The pFF of 0.83 indicates the cell has great potential to achieve >0.81 FF if the printed metal gridlines and contact firing are optimized with low contact and gridline lateral resistances. The low junction reverse saturation current density (J_{o2}) and n factor at 0.1 sun show the cell has excellent contact firing and good junction properties. Note that all the parameters shown by Suns-V_{oc} measurements for both cells have similar values. This indicates that the performance differentiator for both cells is R_s. Because the Suns-V_{oc} measurement is free of R_s, so R_s could be the main factor that causes the difference in performance for the 3- and 5-BB cells.

Table 5.3: Suns-V_{oc} measurements for a 3-BB cell and the best 5-BB cell.

Name	Pseudo Efficiency	V_{oc} (mV)	pFF	n factor @ 1 sun	n factor @ 0.1 sun	J_{o1} (mA/cm^2)	J_{o2} (mA/cm^2)
3-BB Ave.	20.80	649.8	0.8309	0.95	1.10	4.30E-13	5.40E-09
5-BB Ave.	20.87	650.3	0.8307	0.98	1.10	4.28E-13	5.28E-09

In order to understand why the measured FF was far away from the pFF, location-dependent Suns-V_{oc} measurement was carried out. Multiple measurements for all the parameters, V_{oc}, pseudo FF (pFF), pseudo efficiency, n factor and J_{o2} were carried as plotted in the contour maps in Figures 5.16 to 5.20. The relatively small standard deviation for the values in each contour map indicates that the non-uniformity of the sheet resistance for the $POCl_3$ diffused emitter is within a small range. Figure 5.16 compares the V_{oc} variation for the 3- and 5-BB cells, which are quite similar. This should be because the grid

coverage for both cells are similar and therefore the metal recombination for the cells are the same. Also, since the pFF does not take into account the series resistance, it is also expected to be same irrespective of the number of busbars as shown in Figure 5.17. The J_{sc} was very close for the two cells (38.5 for 3-BB and 38.6 for the 5-BB). The difference in J_{sc} may be due to the slight difference in the R_s as shown in Figure 5.21 or a combination of ARC and emitter difference. Since firing was done at the same peak temperature, the n-factor and junction recombination are similar as in Figures 5.19 and 5.20. Thus the pseudo efficiency of >20% indicates the Al-BSF cell has the potential of reducing the cost of PV.

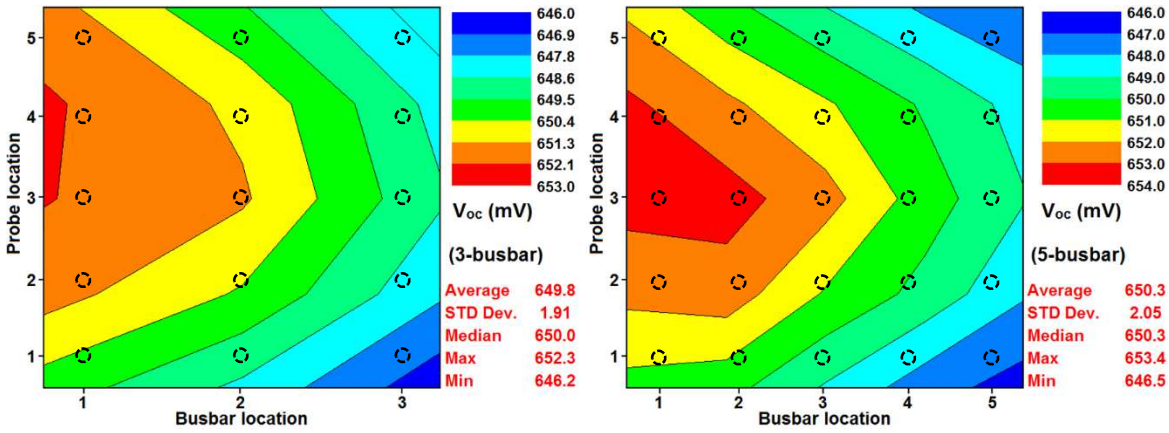

Figure 5.16: Contour map of V_{oc} for both 3- and 5-BB cells.

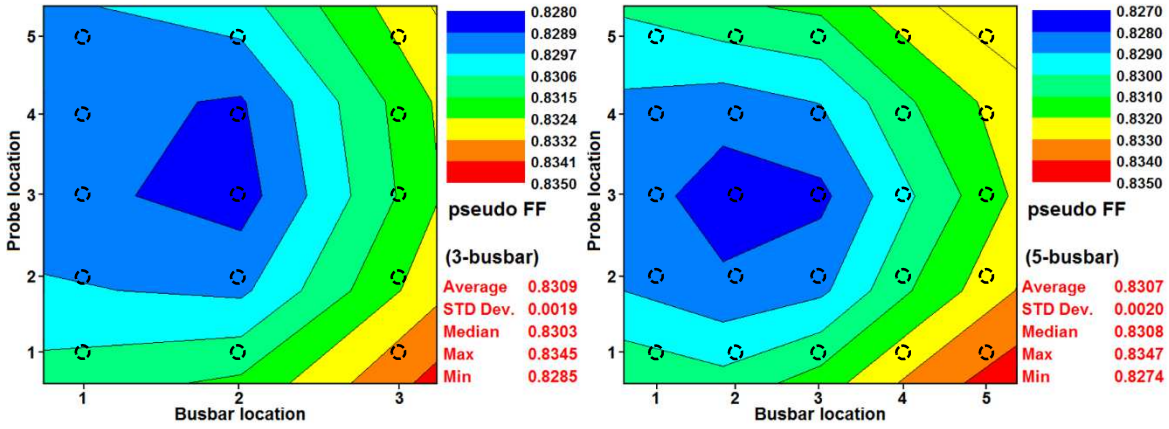

Figure 5.17: Contour map of the pFF for both 3- and 5-BB cells.

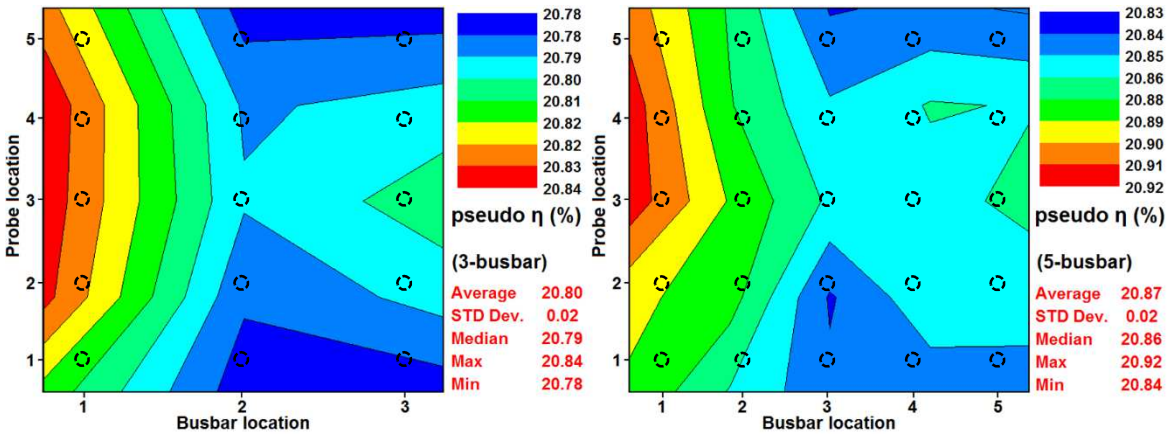

Figure 5.18: Contour map of pseudo efficiency for both 3- and 5-BB cells.

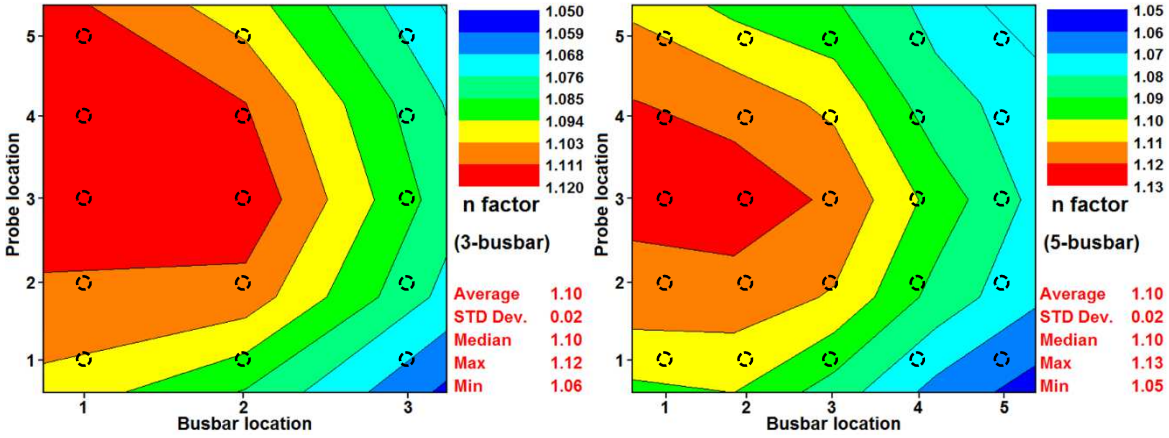

Figure 5.19: Contour map of n factor for both 3- and 5-BB cells.

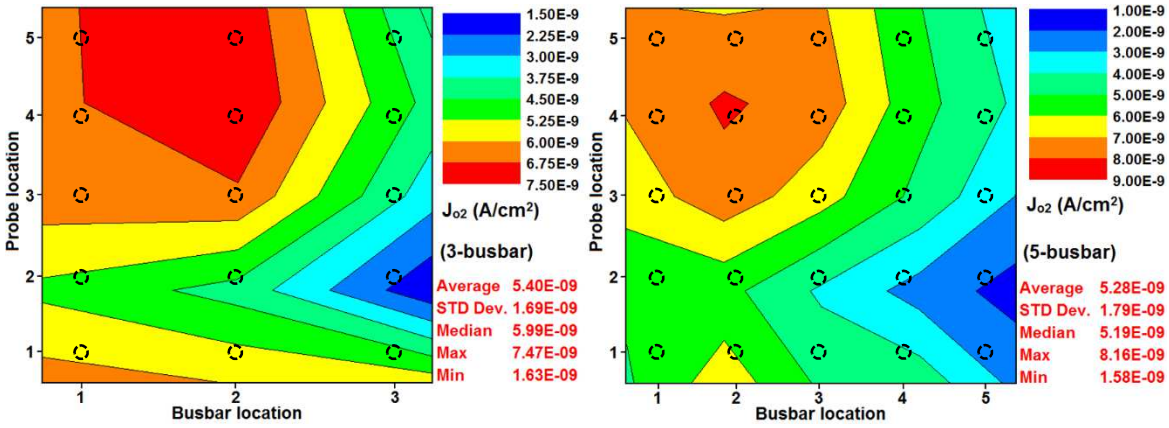

Figure 5.20: Contour map of J_{o2} for both 3- and 5-BB cells.

To identify the main performance differentiator for both 3- and 5-BB solar cells, the R_s was calculated based on V_{oc}, J_{sc}, pFF, FF and J_{mp} at the maximum power point, as shown in the equation below,

$$R_s = \frac{V_{oc} \cdot J_{sc} \cdot (pFF - FF)}{{J_{mp}}^2} \tag{5.1}$$

With the location-dependent pFF, the contour maps of R_s for both 3- and 5-BB cells were also created based the contour map of pFF, as illustrated in Figure 5.21. Tremendous different in R_s was found for both cells with 3-BB cell having R_s of 0.8628 Ω·cm^2, and 5-BB cell having R_s of 0.5035 Ω·cm^2. This explains why the FF of the 5-BB cell is higher than the 3-BB counterpart in the I-V measurements. Also this confirms the prediction in the simulation, which states that the 5-BB cell has lower Rs due to decreased effective gridline resistance compared to the 3-BB counterpart.

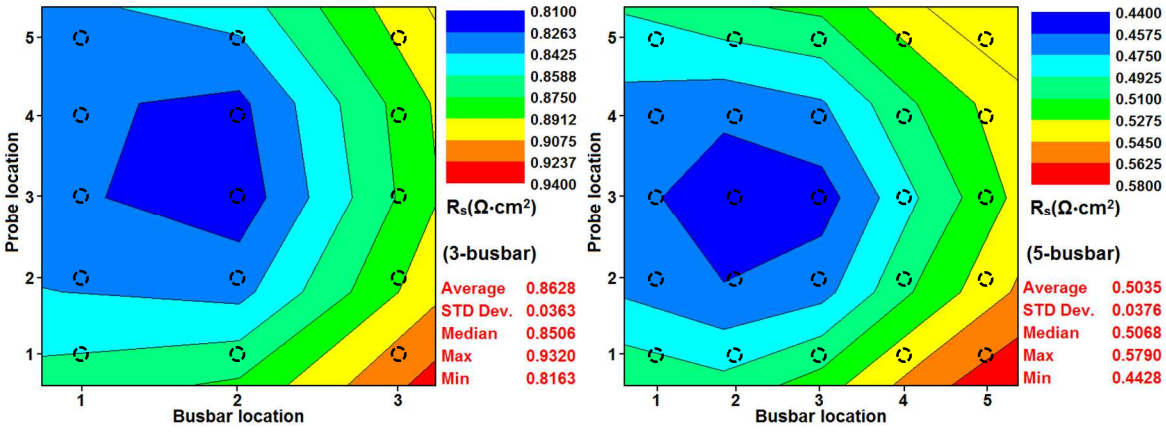

Figure 5.21: Contour map of R_s for both 3- and 5-BB cells.

5.3 Conclusions

It was demonstrated that the multi-busbar (4- and 5-BB) silicon solar cell designs bring benefits in FF and efficiency because of decreased R_s with more number of busbars. By implementing the same TBW, the solar cell performance can be enhanced with more

than 3-BB metal grid designs without adding any cost. This was confirmed both theoretically and experimentally. Based on the measured I-V data for all experimental cells, solar cell efficiency can be increased by $0.41\%_{absolute}$ when the number of busbars increases from three to four, and $0.66\%_{absolute}$ from three to five. And 5-BB cell have great potential to reach 20% efficiency with further improvement in front grid design. This indicates that the state-of-the-art 3-BB Al-BSF solar cell design should be re-considered in terms of efficiency enhancement and cost savings when fine line printing becomes prevalent in industrial mass production. And special attention should be paid to multi-busbar solar cells with narrower busbar width, particularly when compatible narrower ribbon material becomes commercially available. The IQE analysis between the best 5-BB cell and the PERC cell suggests that the efficiency of PERC cell can also be greatly improved if multi-busbar is used.

CHAPTER 6: INVESTIGATION OF THE IMPACT OF GRID SEGMENTATION AND UNEVEN BUSBAR ON SOLAR CELL PERFORMANCE

6.1 Introduction

In this part we investigate some promising front grid metallization patterns that can further increase the V_{oc}, J_{sc}, FF and hence the efficiency to ≥20%. In addition to increasing the efficiency, the cost reduction of metallization can also be realized. The V_{oc} of a cell can be increased if the metal recombination is decreased. The metal recombination for the homogeneous emitter can be reduced if the gridlines are narrow in addition to segmentation. The segmentation of the metal grids as well as uneven busbars can enhance the J_{sc}. However, the FF must also increase to yield the desired high efficiency. Therefore, the metal grid design with the introduction of grid segmentations and uneven busbars need to be optimized to achieve high V_{oc} and J_{sc} without sacrificing FF.

In order to accurately assess the impact of the segmentations of gridlines and busbars, as well as uneven busbars, a comprehensive empirical grid model was first established. This was followed by investigation of (i) the effect of segmented gridlines on efficiency for a three and five uniform busbar cells; (ii) the effect of segmented bus bars and gridlines on efficiency for a three and five uniform busbar cells; and (iii) the effect of uneven bus bars in conjunction with the segmented gridlines on efficiency for the three and five busbar cells, as demonstrated in Figure 6.1. Each of these scenarios was investigated theoretically with modeling to evaluate the impact on cell performance. The cost benefits for each of the scenarios were also taken into account.

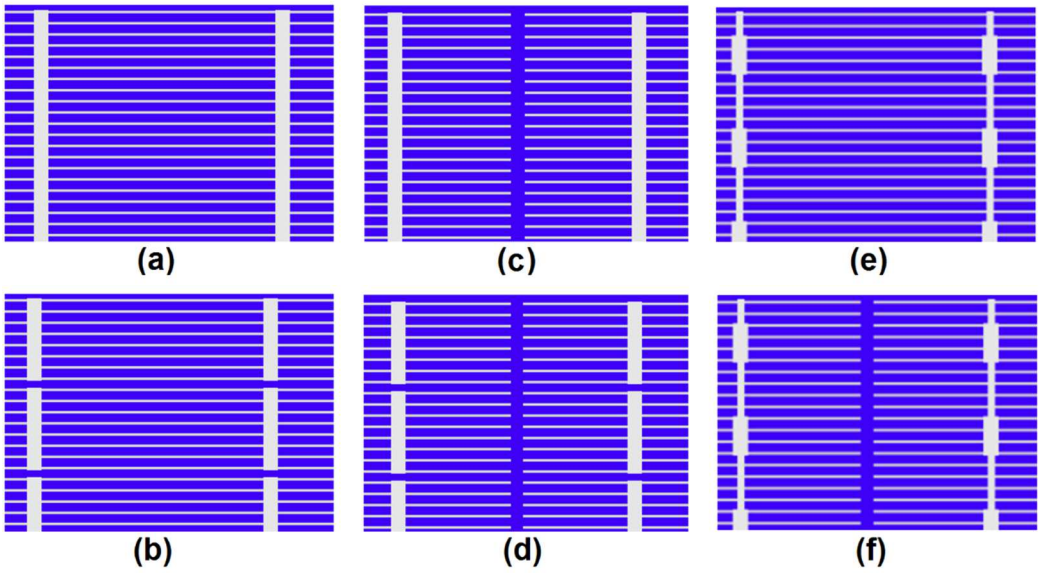

Figure 6.1: Different design patterns for front metal contacts. (a) Even busbar + continuous gridlines; (b) segmented busbar + continuous gridline; (c) even busbar + segmented gridline; (d) segmented busbar + segmented gridline; (e) uneven busbar + continuous gridline; (f) uneven busbar + segmented gridline.

6.2 Simulation Process

Similar to the simulation work done in Chapter 4, the modeling inputs also used the experimentally measured electrical parameters from an industrial size (239 cm^2), 3-BB monocrystalline Al-BSF silicon solar cell with continuous busbars and gridlines. However, apart from the regular input parameters of the front electrodes (height and width of gridlines and busbars, and the number of gridlines and busbars), gridline and busbar segmentations, as well as the uneven features of busbars were incorporated in the model. And a comprehensive empirical grid model was developed to evaluate the impact of the introduction of grid segmentations and uneven busbar features on R_s. With the new grid model, the simulation followed the same methodology as described in Chapter 4. Some of the input and output parameters for the reference cell and modeled cell are listed in Table 6.1. Note that the gridline and busbar segmentations were set to zero, and the ratio of major

busbar length to minor busbar length was set to 1 so as to simulate the reference cell with continuous metal grid and even busbars.

Table 6.1: Device and material parameters for reference cell and modeled cell without segmentations in metal grids.

Parameters	**Reference Cell**	**Modeled Cell**
Wafer thickness (μm)	180	180
Emitter sheet resistance (Ω/□)	75	75
Gridline width (μm)	~70	70
Gridline height (μm)	~20	20
Busbar width (mm)	1.5	1.5
Busbar height (μm)	~20	20
Base resistivity (Ω-cm)	1.5	1.5
Contact resistivity (mΩ-cm^2)	3.5	3.5
Gridline resistivity (Ω-cm)	5.0E-06	5.0E-06
V_{oc} (mV)	640.4	640.3
J_{sc} (mA/cm^2)	37.81	37.77
Fill factor	0.8030	0.8033
Efficiency (%)	19.44	19.43

By taking the input values from the reference cell, the modeled I-V data showed very good match with the measured data. This indicates that the calculations in the model are reliable to evaluate the metallization impact on solar cell performance. The modeled cell, subsequently, was taken as the baseline to investigate different scenarios in the metal grid designs (Figure 6.1).

6.3 Arithmetical Description of Segmented Grid and Uneven Busbar

For optimal grid pattern trends versus solar cell efficiency, different grid models [65-68, 81] have been developed to assess the total R_s and the corresponding resistive components such as emitter, gridline, busbar, and contact, etc. Because of non-uniformity and porosity of printed metal gridlines and busbars, and non-rectangular shape of gridline's cross section, as shown in Figure 6.2, the assumptions in those grid models disagree with

the practically printed metal grid. This often results in inconsistencies between the calculated total R_s and the measured values.

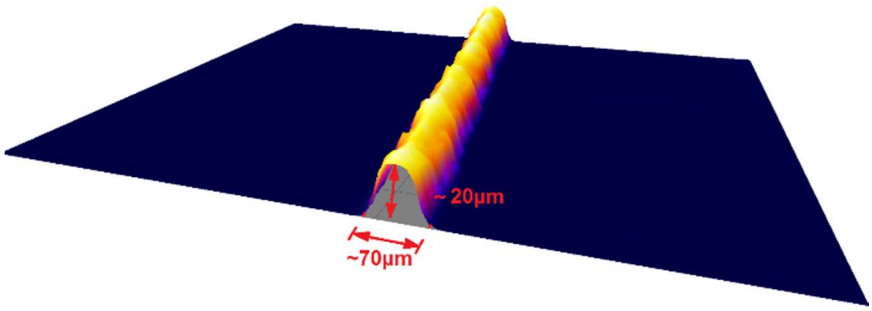

Figure 6.2: Practical profile of a screen-printed gridline.

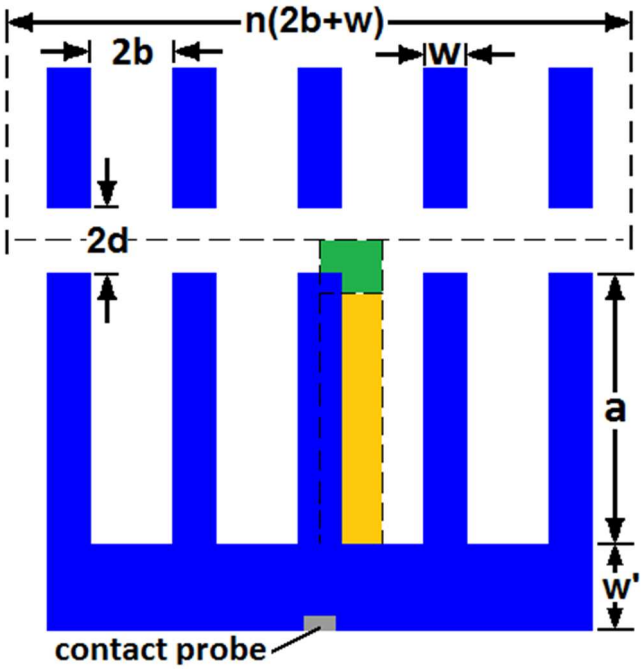

Figure 6.3: Simple grid pattern for solar cells with segmentation of gridlines. Active unit cell area is: $n(2b+w)(d+a+w')$.

To overcome this discrepancy, direct measurements of BBR and FBR were implemented by Meier et al. [67-68]. Also, the Gaussian shaped gridline was employed by Jiang et al [65] to simulate the practical shape of the screen-printed gridline. However, the direct measurements of BBR and FBR are not feasible due to segmented grid. Therefore

the grid model to assess the R_s of segmented grid needs to be established to further investigate the impact, as discussed below.

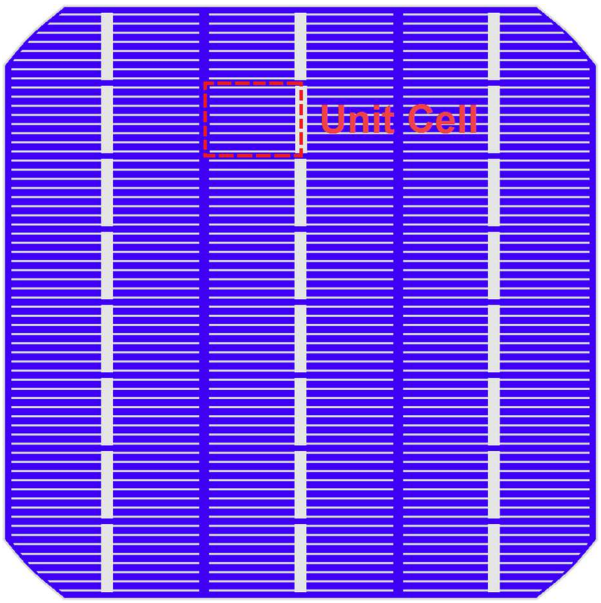

Figure 6.4: Front grid design of 3-BB solar cell with segmented gridlines and busbars.

Figure 6.3 shows a unit cell, as indicated in Figure 6.4, used in the calculation model to evaluate the series resistance. The unit cell has $d+a+w'$ units long and $n(2b+w)$ units wide, where n is the number of gridlines assigned to each unit cell, $2b$ is the distance between the edges of the neighboring gridlines, $2d$ is the length of gridline segmentation, w is the width of gridline, $2w'$ is the width of busbar, and a is the length of gridline in the unit cell, as shown in Figure 6.4. The entire solar cell is then composed of repeated unit cells across the full cell area.

6.3.1 Emitter Resistance

The power loss due to series resistance is associated with current traveling through the emitter, the contact resistance, gridlines, busbars, and through the base of the cell.

According to Meier et al. [57], for diffused emitter layer in the yellow region (Figure 6.3), the power loss is given by

$$P_{emitter1} = \frac{1}{3} {J_L}^2 \left(a - \frac{w}{2}\right) b^3 R_{sheet} \tag{6.1}$$

where J_L is the light-generated current density, R_{sheet} is the emitter sheet resistance, *a-w/2* is the length of emitter in the yellow region (Figure 6.3), and *2b* is the spacing of gridline.

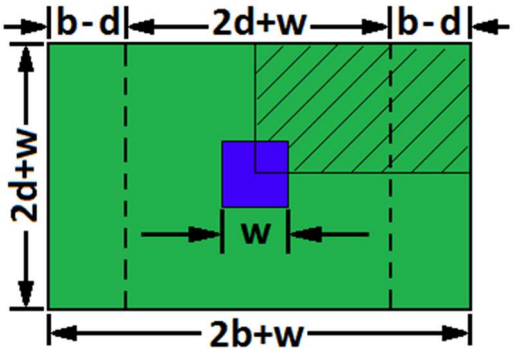

Figure 6.5: A non-square subdivision element (hatch shading area) of the unit cell with three mirror symmetries ($b \geq d$)

The diffused emitter layer in the green region (Figure 6.3) is shown in the hatch shading area of Figure 6.5. The combination of the hatch shading area with its three mirror symmetries, as demonstrated in Figure 6.5, resembles the subdivision of a symmetry element of a EWT solar cell. According to Fallisch et al. [114], the power loss of the whole green region in Figure 6.5 can be written as

$$P_{emitter2} = \frac{{J_L}^2 R_{sheet} (2d+w)^4}{2\pi} \left(ln\left(\frac{2d+w}{w}\right) - \frac{3}{4} + \frac{w^2}{(2d+w)^2} - \frac{w^4}{4(2d+w)^4} \right) \cdot \left(1 + f \cdot \frac{2b-2d}{2d+w}\right) + \frac{2{J_L}^2 R_{sheet} (2d+w)(b-d)^3}{3} \tag{6.2}$$

where $f = 0.61+0.44 \cdot exp[w/(2d+w)]$. Note that the above expression for the power loss is obtained based on the assumption that $b \geq d$. For $b \leq d$, the subdivision element in Figure

6.5 can be transformed into the counterpart shown in Figure 6.6. Similarly, the power loss can be written as,

$$P'_{emitter2} = \frac{{J_L}^2 R_{sheet}(2b+w)^4}{2\pi}\left(ln\left(\frac{2b+w}{w}\right) - \frac{3}{4} + \frac{w^2}{(2b+w)^2} - \frac{w^4}{4(2b+w)^4}\right) \cdot \left(1 + f' \cdot \frac{2d-2b}{2b+w}\right) + \frac{2{J_L}^2 R_{sheet}(2b+w)(d-b)^3}{3} \quad (6.3)$$

where f'=0.61+0.44·exp[$w/(2d+w)$].

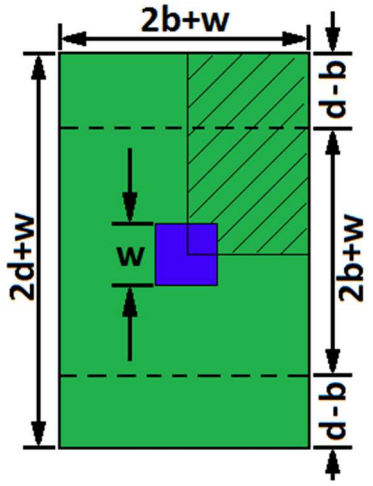

Figure 6.6: A non-square subdivision element (hatch shading area) of the unit cell with three mirror symmetries ($b \leq d$)

Therefore the total power loss associated with the emitter in the unit cell shown in Figure 6.4 can be given as,

$$P_{emitter} = \begin{cases} 2n(P_{emitter1} + \frac{P_{emitter2}}{4}), & b \geq d \\ 2n(P_{emitter1} + \frac{P'_{emitter2}}{4}), & b \leq d \end{cases} \quad (6.4)$$

6.3.2 Contact Resistance

The power loss associated with the contact resistance is

$$P_{contact} = n \cdot (I^2 R_c) \quad (6.5)$$

According to the theory of transmission line model, the contact resistance (R_c) is given by [115],

$$R_c = \frac{R_{sheet}L_T}{a} \cdot \coth\left(\frac{w}{L_T}\right) \tag{6.6}$$

$$R_c = \frac{\rho_c}{aL_T} \cdot \coth\left(\frac{w}{L_T}\right) \tag{6.7}$$

where the transfer length L_T is defined as [116],

$$L_T = \sqrt{\rho_c / R_{sheet}} \tag{6.8}$$

Note that two cases lead to simplifications of Eq. (6.7). For $w \leq 0.5L_T$, $\coth(w/L_T) \approx L_T/w$ and

$$R_c \approx \frac{\rho_c}{aw} \tag{6.9}$$

For $w \geq 1.5L_T$, $\coth(w/L_T) \approx 1$ and

$$R_c \approx \frac{\sqrt{\rho_c R_{sheet}}}{a} \tag{6.10}$$

Suppose ρ_c =3 mΩ-cm^2, R_{sheet} = 80 Ω/□, then we have L_T ≈60 μm. This means that to take advantage of the approximation in Eq. (6.10), the width of gridline has to be greater than ~90 μm, which will not be true for the shrinking gridline width driven by silver cost-reduction and more advanced printing technologies such as inkjet printing.

Therefore with

$$I = J_L\left[2ab + 2d\left(b + \frac{w}{2}\right)\right] \tag{6.11}$$

The expression for contact resistance dissipated power yields,

$$P_{contact} = 4n{J_L}^2\left[ab + d\left(b + \frac{w}{2}\right)\right]^2 \frac{R_{sheet}L_T}{a} \cdot \coth\left(\frac{w}{L_T}\right) \tag{6.12}$$

6.3.3 Gridline Resistance

Associated with current flow along the gridline, the power loss is

$$P_{gridline} = n\int_0^a I^2(y)dR \tag{6.13}$$

where I(y) is the accumulated current in the gridline at location y. To simplify the calculation, we can assume that the photo-generated current at the segmented region goes to the gridline at location y = *a*, so we have

$$I(y) = J_L d(2b + w) + 2\int_y^a J_L b dy = J_L[d(2b + w) + 2b(a - y)] \tag{6.14}$$

The resistance of *dR* as an element of the gridline is represented by

$$dR = \frac{\rho_f}{A_f} dy' \tag{6.15}$$

where ρ_f is the resistivity of gridline material, and A_f is the cross-sectional area of the gridline. Since the cross section of the practical gridline is not ideally rectangular, a Gaussian curve is used to simulate the shape of gridline, as shown in Figure 6.7.

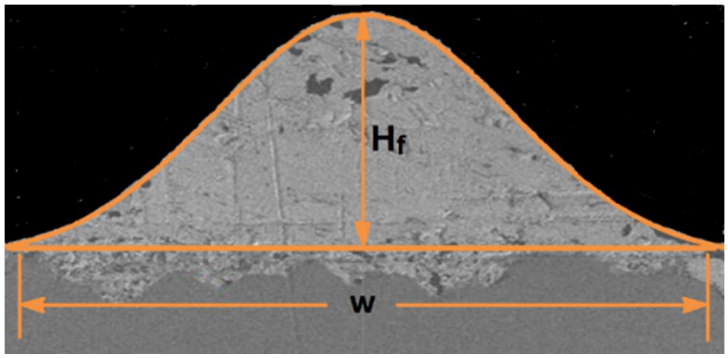

Figure 6.7: Gaussian shape of metal gridlines with gridline width of w and height of H_f.

The profile of a Gaussian shape gridline can be described as Eq. (6.16), with the peak of H_o and the standard deviation of σ,

$$f(x) = H_o \cdot e^{-\frac{x^2}{2\sigma^2}} \tag{6.16}$$

To find gridline width (w) in the Gaussian profile, we assume that w equals $1/e^2$ width of the Gaussian profile, which is defined as the distance between the two points (x_1, $f(x_1)$), (x_2, $f(x_2)$) on the Gaussian curve where $f(x_1) = f(x_2) = H_o/e^2$. Then we have

$$w = 2\sigma - (-2\sigma) = 4\sigma \tag{6.17}$$

And gridline height H_f can be calculated as

$$H_f = H_o(1 - \frac{1}{e^2}) \tag{6.18}$$

The cross-sectional area of gridline can thus be obtained as

$$A_f = H_o \int_{-2\sigma}^{2\sigma} e^{-\frac{x^2}{2\sigma^2}}\, dx - 4\sigma \cdot (H_o - H_f) = \sqrt{2\pi}\sigma \cdot \mathrm{erf}(\sqrt{2})H_o - \frac{4\sigma H_o}{e^2} \tag{6.19}$$

Combining Eqs. (6.17), (6.18) and (6.19), gives

$$\mathrm{A}_f = (\frac{\sqrt{2\pi}}{4} \cdot \mathrm{erf}(\sqrt{2}) - \frac{1}{e^2}) \cdot wH_f \cdot \frac{e^2}{e^2 - 1} \tag{6.20}$$

Substituting Eqs. (6.14), (6.15), (6.20) into (6.13), the power loss with gridlines in the unit cell yields

$$P_{gridline} = \frac{nJ_L{}^2\rho_f}{(\frac{\sqrt{2\pi}}{4} \cdot \mathrm{erf}(\sqrt{2}) - \frac{1}{e^2}) \cdot wH_f \cdot \frac{e^2}{e^2 - 1}} \cdot \left[\frac{4}{3}b^2a^3 + 2bda^2(2b + w) + d^2a(2b + w)^2\right] \tag{6.21}$$

6.3.4 Busbar Resistance

6.3.4.1 Uniform Busbars

In addition to emitter, contact, gridlines, the fourth contribution to power loss is the busbar. In the unit cell, the current enters the busbar from the individual gridlines in discrete quantities, then flows along the busbar and leaves the unit cell from a contact probe at the

center of the busbar (Figure 6.4). To simplify the calculation, the current is treated as if it enters the busbar continuously. The power loss associated with the busbar is thus given as

$$P_{busbar} = 2\int_0^{n(b+\frac{w}{2})} {I_b}^2 dR' \tag{6.22}$$

where I_b can be expressed as

$$I_b = \int_x^{n\left(b+\frac{w}{2}\right)} J_L\left(a+d-\frac{aw}{2b+w}\right)dx = J_L\left(a+d-\frac{aw}{2b+w}\right)\left[n\left(b+\frac{w}{2}\right)-x\right] \tag{6.23}$$

The resistance dR' of an element of busbar is given by

$$dR' = \frac{\rho_f}{A_b}dx' \tag{6.24}$$

Since the busbar width is much wider than that of gridline, it is technologically easier to print the busbar with a rectangular cross-sectional area, therefore

$$A_b = 2w' \cdot H_b \tag{6.25}$$

where $2w'$ is the busbar width, and H_b the busbar height. Substituting Eqs. (6.23), (6.24), (6.25) into (6.22), the expression for power loss associated with busbar can be deduced as,

$$P_{busbar} = \frac{\rho_f {J_L}^2 n^3}{3w'H_B}\left(a+d-\frac{aw}{2b+w}\right)^2 (b+w/2)^3 \tag{6.26}$$

6.3.4.2 Uneven Busbars

For solar cells designed with uneven busbars, as shown in Figure 6.8, we can similarly calculate the power loss with busbars by combining the losses from both the major and the minor parts. Assume the ratio of the length of major part of busbar to total busbar length is *s*, the width of the major part is $2w_1$, and the minor part is $2w_2$, then we have,

$$P_{minor} = \frac{\rho_f {J_L}^2 n^3}{3 w_2 H_B}\left(a + d - \frac{aw}{2b + w}\right)^2 \left(b + \frac{w}{2}\right)^3 (1 - s)^3 \tag{6.27}$$

$$P_{major} = \frac{\rho_f {J_L}^2 n^3}{3 w_1 H_B}\left(a + d - \frac{aw}{2b + w}\right)^2 \left(b + \frac{w}{2}\right)^3 [1 + (s - 1)^3] \tag{6.28}$$

Therefore the total power loss associated with the busbar is,

$$P_{busbar}{}' = \frac{\rho_f {J_L}^2 n^3}{3 H_B}\left(a + d - \frac{aw}{2b + w}\right)^2 \left(b + \frac{w}{2}\right)^3 \left[\frac{1 + (s - 1)^3}{w_1} + \frac{(1 - s)^3}{w_2}\right] \tag{6.29}$$

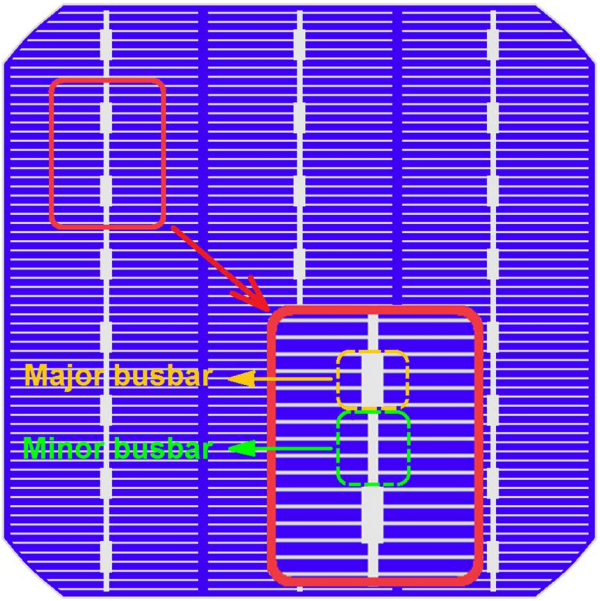

Figure 6.8: Solar cell designed with uneven busbars with the major part of busbar having regular width, and the minor part having shrunk width.

6.3.5 Base Resistance

Current flow through the base of the cell results in a power loss given simply by

$$P_{base} = I^2 R_{base} \tag{6.30}$$

with

$$I = 2 n J_L \left[ab + d\left(b + \frac{w}{2}\right)\right] \tag{6.31}$$

$$R_{base} = \frac{\rho_w t_w}{A_{cell}} = \frac{\rho_w t_w}{n(2b+w)(d+a+w')} \tag{6.32}$$

where ρ_w is the base resistivity, t_w is the thickness of the bulk, and A_{cell} the area of the unit cell. Thus the power loss with the base can be rewritten as

$$P_{base} = 4nJ_L{}^2 \left[ab + d\left(b + \frac{w}{2}\right)\right]^2 \cdot \frac{\rho_w t_w}{(2b+w)(d+a+w')} \tag{6.33}$$

6.3.6 Shadowing Loss

Finally, the power loss resulting from front shadowing of the cell by both gridlines and busbar is

$$P_{shadow} = P_L \eta n[aw + w'(2b+w)] \tag{6.34}$$

where P_L is the power density of the incident light and η is the energy conversion efficiency of the cell.

6.3.7 Total Series Resistance

For the power loss with the back metallization, since the entire back side of the silicon wafer is contacted by full Al and silver strips, the power loss associated with the back contact and back metal is relatively much smaller than other losses and can be ignored in the calculation.

To better assess the total power loss of the cell, the corresponding losses with different components of series resistance from Eqs. (6.4), (6.12), (6.21), (6.26), (6.29), (6.33) and (6.34) are then normalized to unit cell area of $n(2b+w)(d+a+w')$, and the summary of expressions are listed in Table 6.2.

Table 6.2 Summary of power loss expressions

Power Loss Factors	Normalized expression
Emitter	$p_{emitter} = P_{emitter} / [\, n(2b+w)(d+a+w')]$
Front Contact	$p_{contact} = P_{contact} / [\, n(2b+w)(d+a+w')]$
Gridline	$p_{gridline} = P_{gridline} / [\, n(2b+w)(d+a+w')]$
Busbar (even)	$p_{busbar} = P_{busbar} / [\, n(2b+w)(d+a+w')]$
Busbar (uneven)	$p_{busbar}' = P_{busbar} / [\, n(2b+w)(d+a+w')]$
Base	$p_{base} = P_{base} / [\, n(2b+w)(d+a+w')]$
Shadowing	$p_{shadow} = P_{shadow} / [\, n(2b+w)(d+a+w')]$

where $(2b+w)(d+a+w')$ is the area of unit cell defined in Figure 6.4.

The overall power loss normalized to unit area is the sum of power loss from the emitter, contact, gridlines, busbar, base, plus the shadowing loss,

$$p_{R_s} = p_{emitter} + p_{contact} + p_{gridline} + p_{busbar} + p_{base} \tag{6.35}$$

$$p_{total} = p_{R_s} + p_{shadow} \tag{6.36}$$

The cell series resistance (Ω-cm^2), normalized to unit area is,

$$r_s = p_{R_s}/J_L^2 \tag{6.37}$$

6.4 Modeled Results and Discussions

6.4.1 Impact of Gridline Segmentation on Solar Cell Efficiency, R_s and FF

The relationship between solar cell efficiency, series resistance and gridline segmentation is shown in Figure 6.9. The efficiency improves when gridline segmentation increases within ~1.2 mm, and decreases with further increased gridline segmentation after ~1.2 mm. Although there is a reduction in gridline shadowing due to larger segmentation, this is negated by larger series resistance. A further investigation, as indicated by the green curve in Figure 6.9, shows that for large gridline segmentation, the change in total series

resistance would be dominated by the variation in emitter resistance, which impacts the efficiency with greatly increased R_s with large segmentation. Note that as gridline segmentation increases from 2 to 6 mm, the efficiency decreases from 19.40 to 19.23%, as demonstrated in Table 6.3.

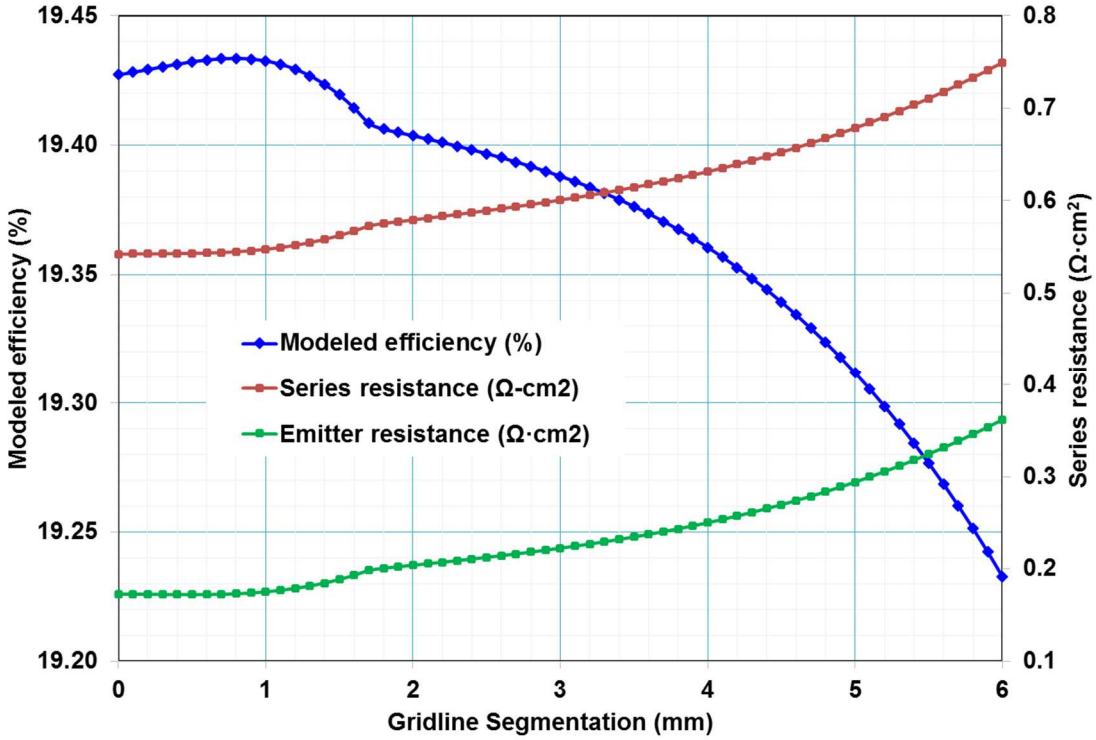

Figure 6.9: Modeled 3-BB cell efficiency, R_s and corresponding emitter resistance plotted as a function of gridline segmentations. Efficiency peaks at segmentation of 0.79 mm.

Table 6.3: Modeled 3-BB cell I-V data with different gridline segmentations.

Gridline Segmentation (mm)	V_{oc} (mV)	J_{sc} (mA/cm^2)	FF	Efficiency (%)
0	640.25	37.77	0.8033	19.4272
1.0	640.30	37.80	0.8030	19.4325
2.0	640.34	37.82	0.8013	19.4036
3.0	640.39	37.84	0.8002	19.3880
4.0	640.43	37.86	0.7985	19.3605
5.0	640.48	37.88	0.7960	19.3118
6.0	640.52	37.90	0.7922	19.2327

To better understand solar cell performance enhanced by the introduction of gridline segmentation, the variations of FF and J_{sc} were also investigated with different gridline segmentations, as illustrated in Figure 6.10. It is observed that FF decreases and J_{sc} increases with increasing gridline segmentation. This is due to the increasing series resistance and decreasing front metal shadowing as gridline segmentation increases. However, efficiency is a product of V_{oc}, J_{sc} and FF. For small gridline segmentation (< ~1.2 mm), the enhancement in J_{sc} outweighs the lost in FF, which explains the improvement in efficiency. But for large gridline segmentation (> ~1.2 mm), the gain in J_{sc} cannot compensate the lost in FF, and this leads to decreased efficiency.

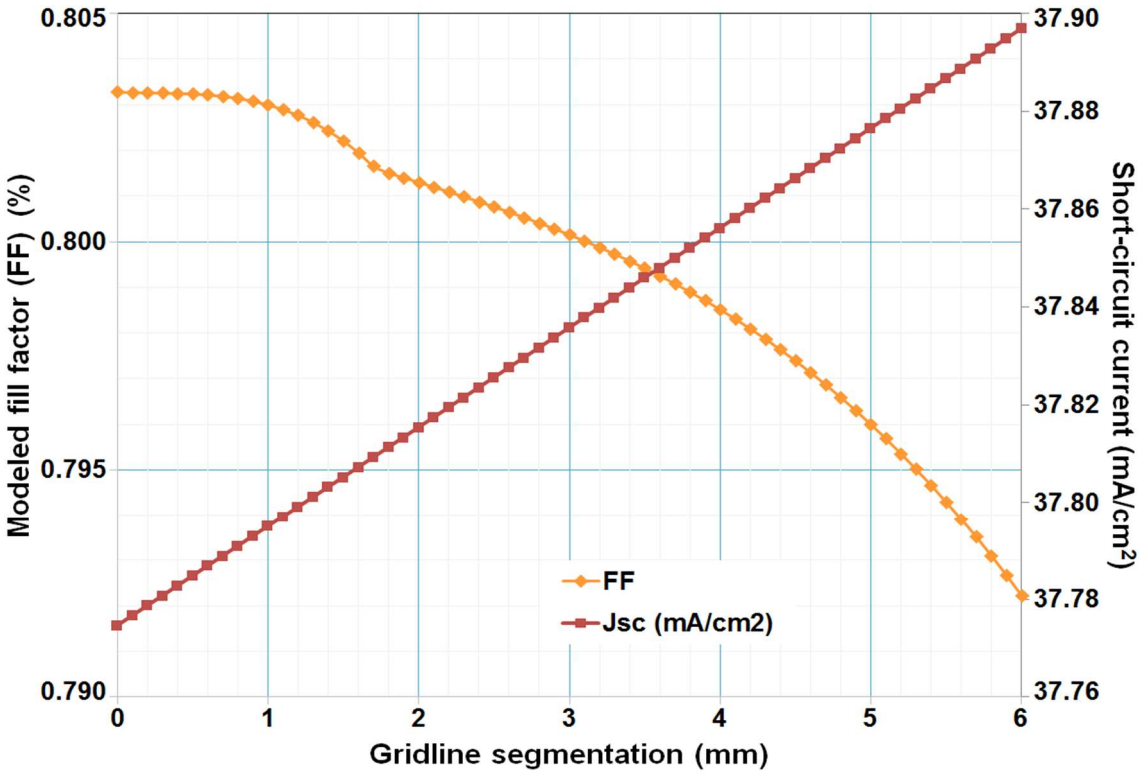

Figure 6.10 Modeled 3-BB solar cell FF and J_{sc} as a function of gridline segmentation. Efficiency peaks at segmentation value of 0.79 mm.

6.4.2 Impact of Busbar Segmentations on Solar Cell Efficiency

Figure 6.11 and 6.12 show the benefits of busbar segmentations for 3- and 5-BB solar cells based on different gridline segmentation scenarios: the continuous gridline, and the gridline with optimal segmentation. In order to make the two different busbar designs comparable, the total busbar coverage was kept the same for different numbers of busbar. It is obvious that the solar cell efficiencies have a linear relationship with busbar segmentations. An increase in efficiency of ~0.05%$_{absolute}$ was found as busbar segmentation increases from 0 to 1.7 mm for both 3- and 5-BB solar cells. This gives a much stronger impact on efficiency than segmentations introduced by the gridline. Note that for a solar cell screen design as shown in Figure 6.1 (b), the busbar segmentation cannot go beyond the gridline spacing. This indicates that there is more room to improve the efficiency if tapered busbar or uneven busbar width is implemented in the busbar design. More so, a quantitative investigation reveals that for 3-BB solar cell design, the optimal gridline segmentation is 0.79 mm and busbar segmentation is 1.7 mm, and this leads to the saving of ~0.26%$_{absolute}$ in metal shadowing, with ~85% contribution in saving from busbar segmentations. While for 5-BB solar cell, similar optimal grid segmentations were found (gridline segmentation = 0.86 mm and busbar segmentation = 1.7 mm), as well as the dominance in metal coverage saving by busbar segmentation. This implies, the redesign of busbars is more effective in efficiency improvement than gridlines.

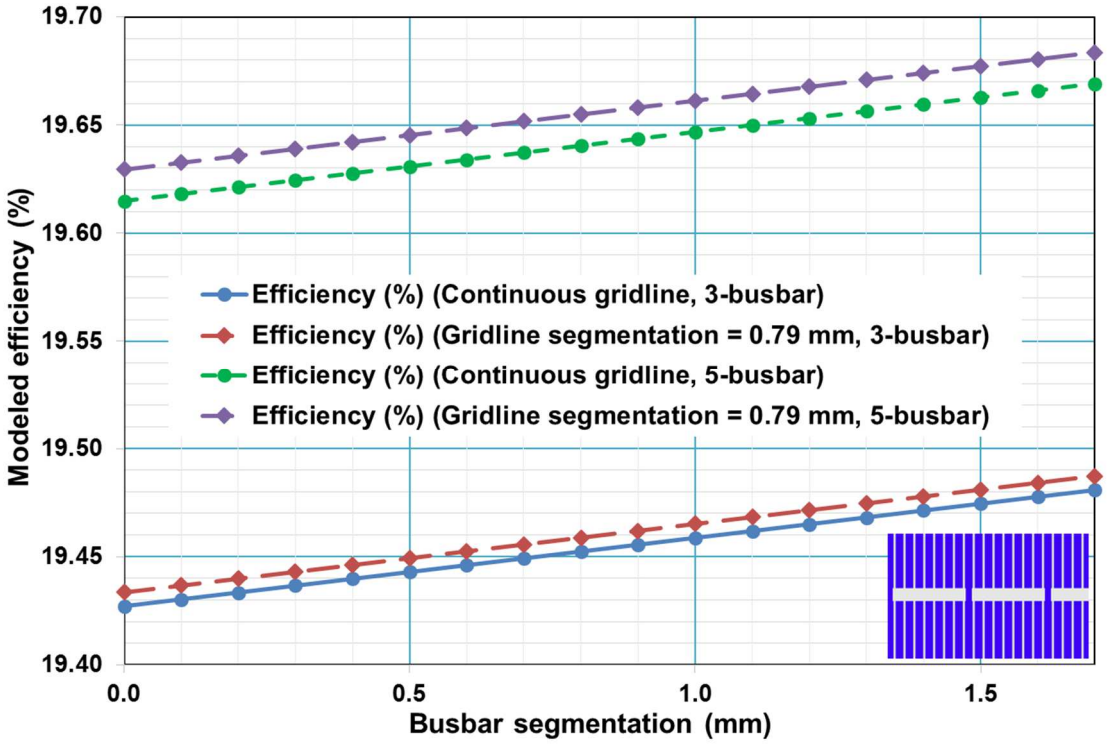

Figure 6.11: Modeled 3- and 5-BB solar cell efficiency as a function of busbar segmentations for continuous gridlines and gridlines with optimal segmentation

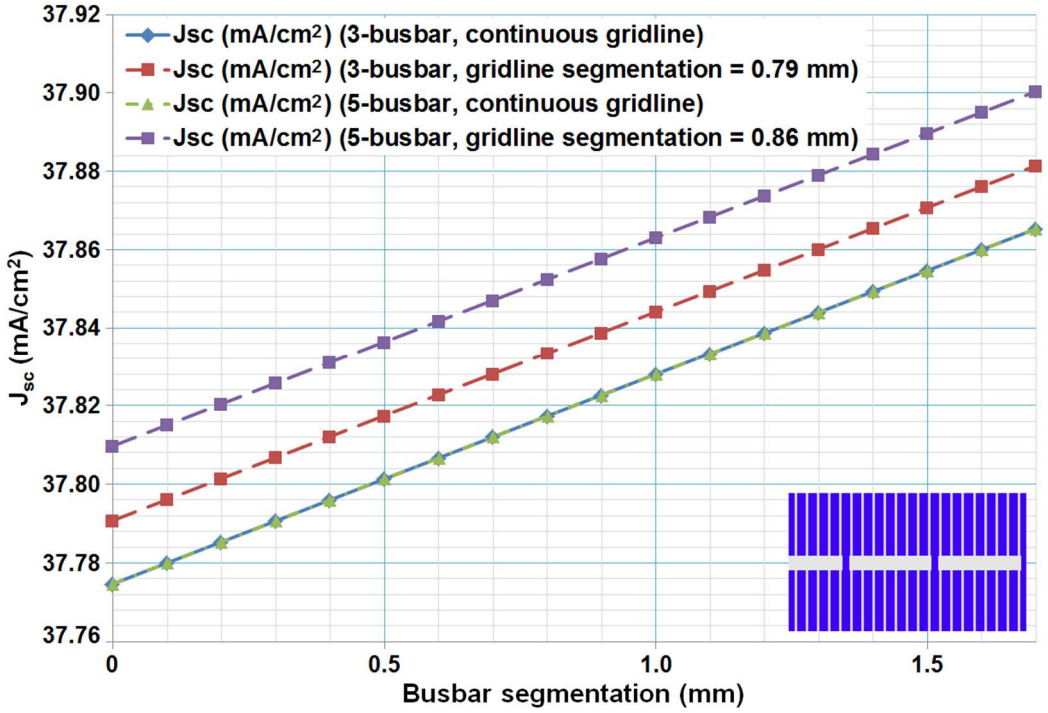

Figure 6.12: Modeled 3- and 5-BB short-circuit currents as a function of busbar segmentations for continuous gridlines and gridlines with optimal segmentation.

6.4.3 Impact of Uneven Busbars on Solar Cell Efficiency

In order to overcome the restriction with segmented busbars in solar cell design, the uneven busbars, as shown in Figure 6.8, were assessed for the impact on cell performance. Both 3- and 5-BB solar cells were taken into account to investigate the variation of front shadowing, J_{sc}, FF and efficiency with ration of major busbar to total busbar (s), and minor busbar width ($2w_2$).

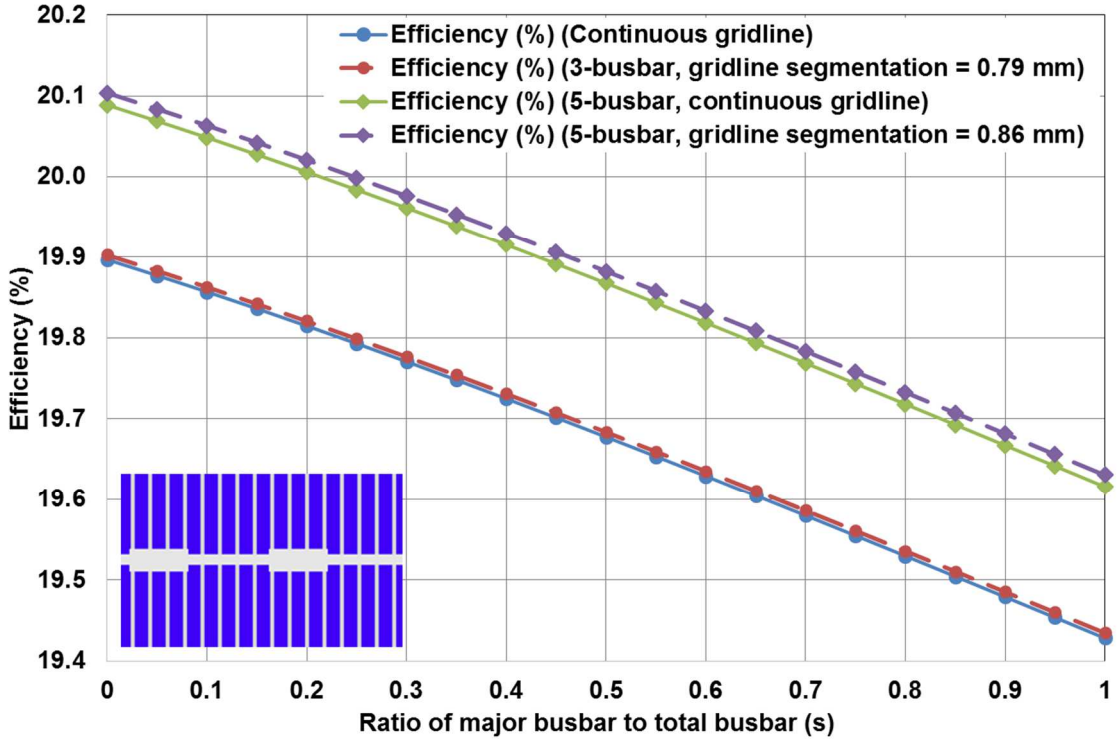

Figure 6.13: Modeled 3- and 5-BB solar cell efficiencies as a function of s for continuous gridlines and gridlines with optimal segmentation (minor busbar width = 0.4 mm).

In Figure 6.13, efficiency was plotted as a function of s for two different gridline types: continuous gridline and gridline with optimal segmentation. Note that s=1 represents uniform busbar width as 1.5 mm and 0.9 mm (major busbar width) for 3- and 5-BB cells, respectively. While s=0 represents uniform busbar width as 0.4 mm and 0.24 mm (minor

busbar width) for 3- and 5-BB counterparts, respectively. As *s* decreases from 1 to 0, the average busbar width shrinks due to the reduced total major busbar length. Because the busbar resistance does not carry much weight in R_s, the decrease in average busbar width only has very small impact in total R_s. As *s* varies from 0 to 1, for instance, the modeled busbar resistance only decreases from 0.044 $\Omega \cdot cm^2$ to 0.012 $\Omega \cdot cm^2$ for both 3- and 5-BB solar cells.

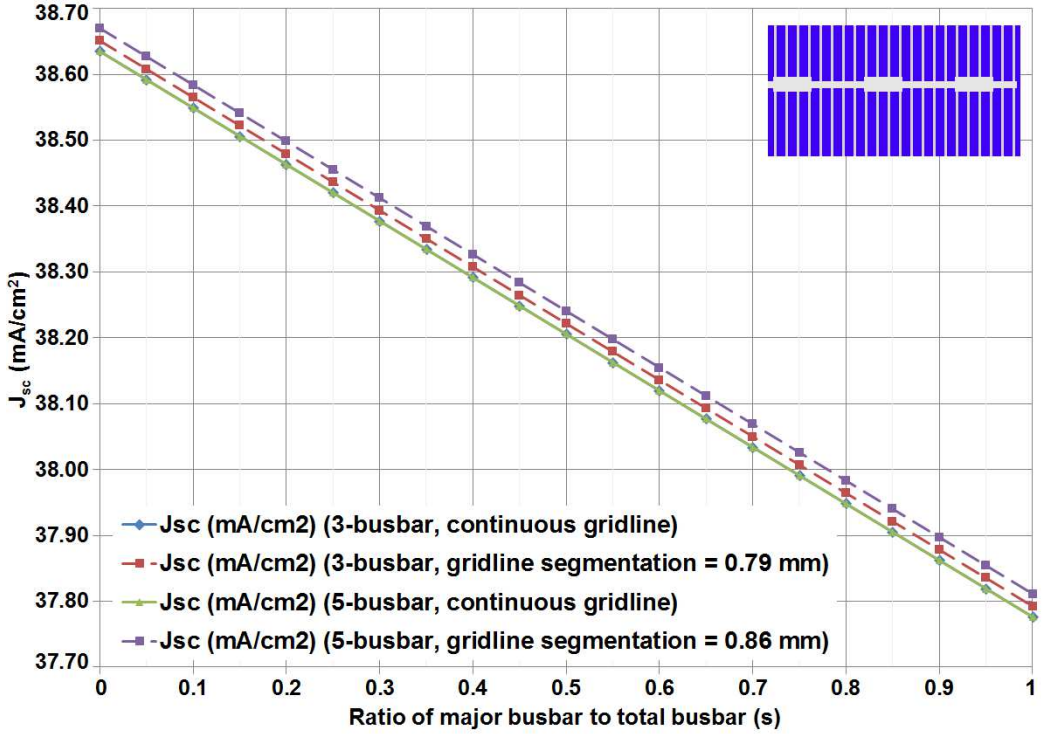

Figure 6.14: Modeled 3- and 5-BB solar cell short-circuit currents plotted as a function of s for continuous gridlines and gridlines with optimal segmentation (minor busbar width = 0.4 mm).

However, the improvement in J_{sc} is pronounced for all solar cell designs as *s* decreases from 1 to 0, as demonstrated in Figure 6.14. And all different cases have ~0.86 mA/cm^2 enhancement in J_{sc} due to the saving in metal shadowing contributed by shrunk average busbar width. Note that 5-BB solar cell has more potential than the 3-BB

counterpart to obtain over 20% conversion efficiency due to relatively shorter effective gridline length. The gridline segmentations associated with the 5-BB design also give stronger effect in the increase of J_{sc} due to more segmentations introduced by more busbars and greater gridline segmentation length.

To further evaluate the enhancement in J_{sc} with shrunk average busbar width, the 3-BB solar cell was taken as an example to investigate the change of front metal shadowing with *s*, as shown in Figure 6.15. It is apparent that the variation in front shadowing is dominated by the change in busbar coverage as *s* decreases from 1 to 0. It is worth mentioning that the reduction in metal shading can be as high as $2.13\%_{absolute}$ when the average busbar width decreases from 1.5 mm to 0.4 mm. This explains the noticeable improvement in J_{sc}, and hence efficiency.

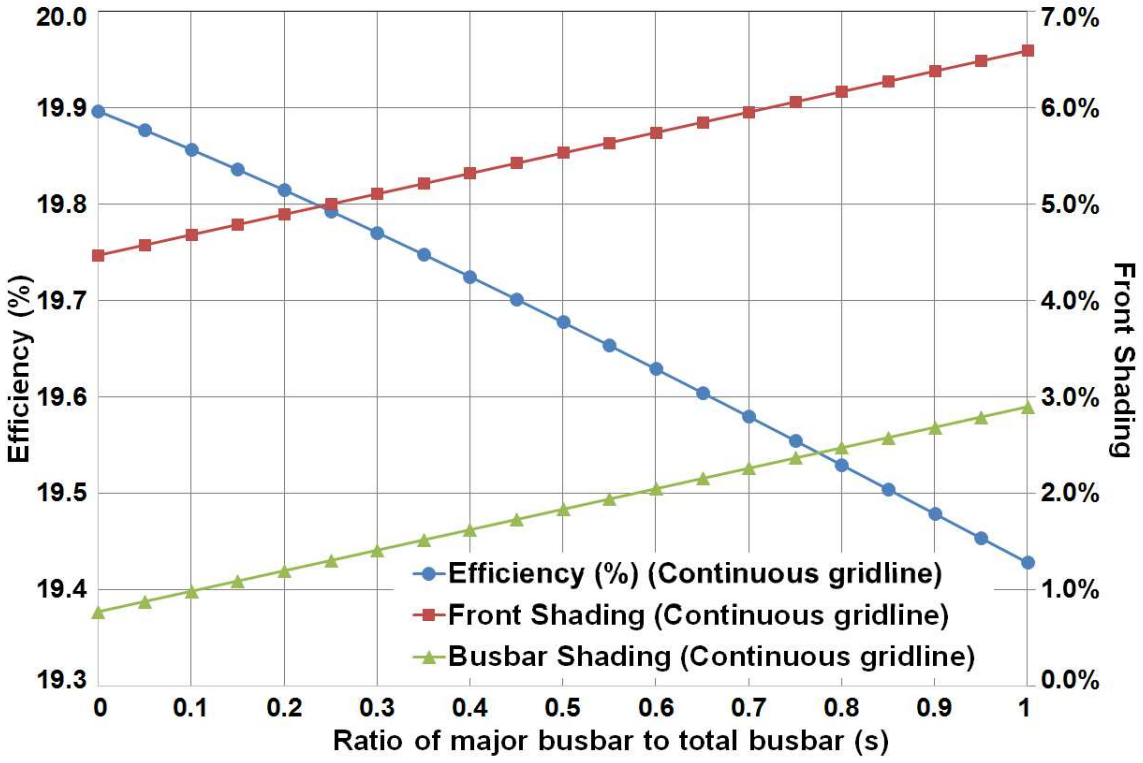

Figure 6.15: Modeled 3-BB solar cell efficiencies and front shading plotted as a function of s for continuous gridlines (minor busbar width = 0.4 mm).

To determine the optimal minor busbar width, practical values for *s* were employed to assess the variation in efficiency as minor busbar width ($2w_2$) changes, as shown in Figure 6.16. Note that the minor busbar width of 1.5 mm represents uniform busbar width along total busbar length, and efficiency stays the same irrespective of the values for *s*. As minor busbar width decreases from 1.5 mm to 0.1 mm, the efficiency keeps increasing for *s* equals 0.4 and 0.5. While for *s* of 0.3, the efficiency reaches the peak at *s*=0.2 mm. More so, for smaller *s* values, the impact of minor busbar width on conversion efficiency gets stronger as it decreases. This indicates that the design of uneven busbar needs to be optimized at cell level before connecting in module.

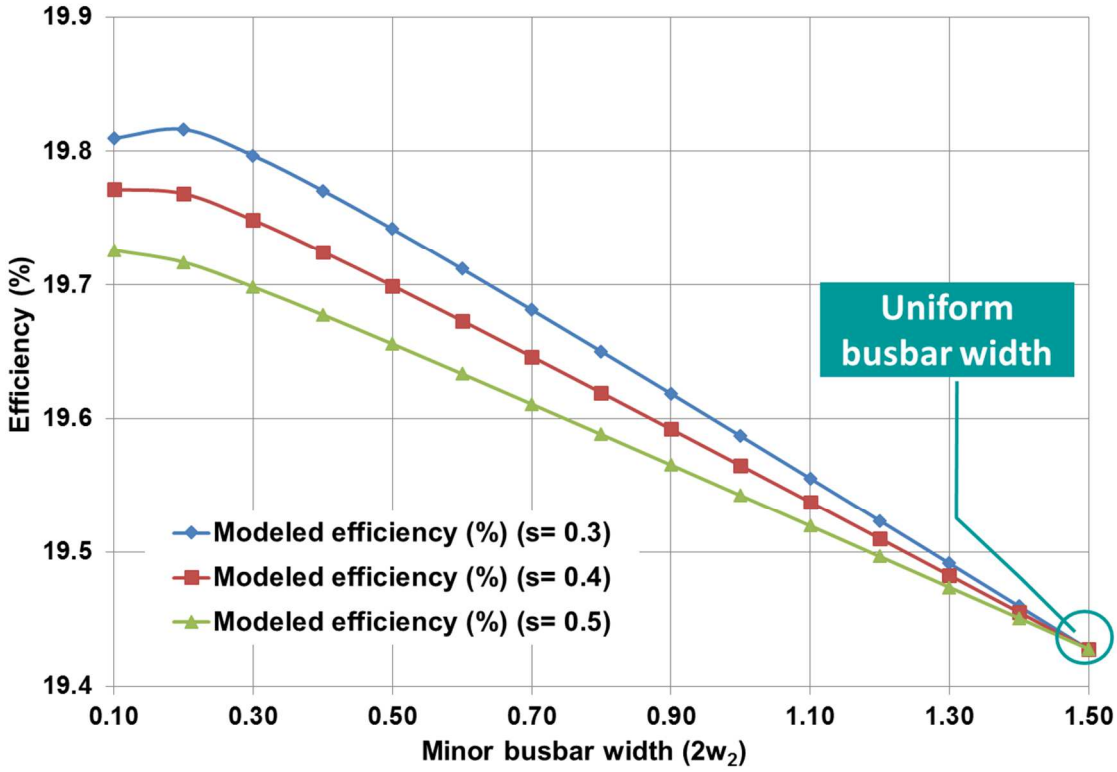

Figure 6.16: Modeled 3-BB solar cell efficiencies plotted as a function of minor busbar width ($2w_2$) for continuous gridlines with s = 0.3, 0.4 and 0.5.

To better interpret the enhancement in efficiency brought by different values for *s* as well as the minor busbar width, the front metal shadowing and J_{sc} were also investigated

correspondingly, as illustrated in Figure 6.17. It is shown that for any given *s*, the front shadowing increases as minor busbar width increases, which explains the decreasing J_{sc} accordingly. When minor busbar width reaches 1.5 mm, the front metal shadowing and J_{sc} associated with different *s* converge at the same point, respectively, because the busbar width along busbar gets uniform such that the cell I-V data becomes independent of *s*. However, for the minor busbar width falls below 1.5 mm, *s* of 0.3 provides the lowest front shadowing and the highest J_{sc}, which corresponds to the highest efficiency obtained in Figure 6.16.

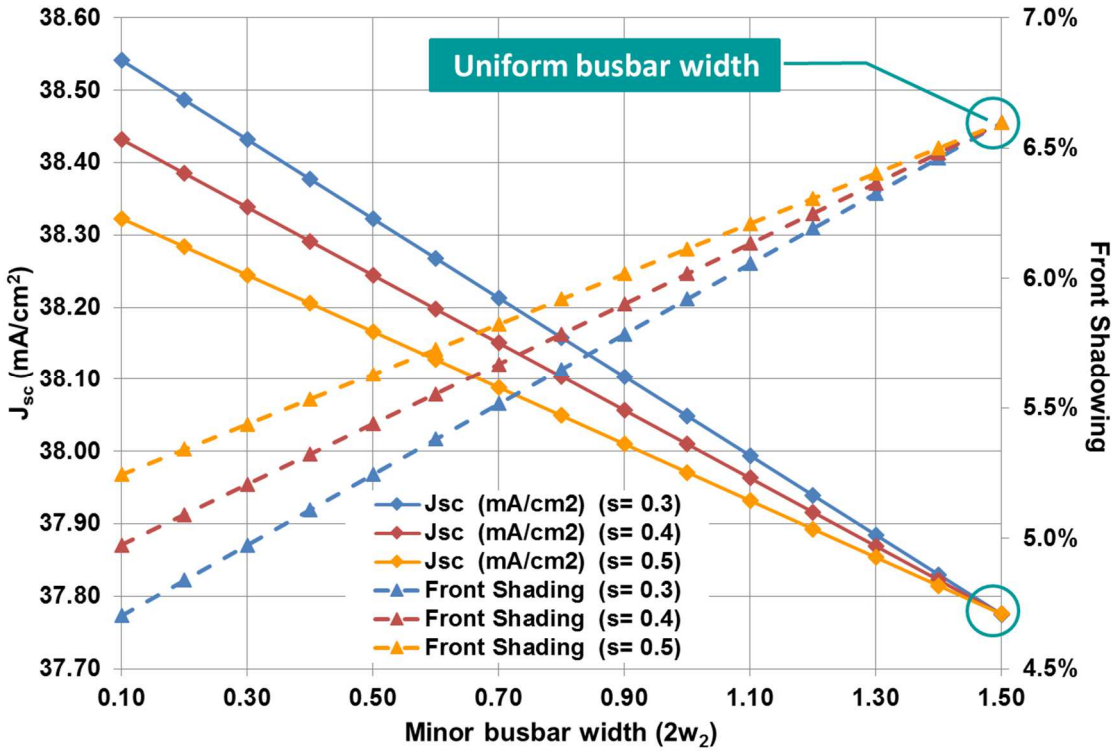

Figure 6.17: Modeled 3-BB solar cell short-circuit current and front shadowing plotted as a function of minor busbar width ($2w_2$) for continuous gridlines with s = 0.3, 0.4 and 0.5.

6.5 Chapter Summary and Conclusions

In this chapter, some promising front grid metallization patterns were investigated to find the path to achieve ~20% conversion efficiency for the conventional Al-BSF solar

cell without any additional cost. To accurately evaluate the series resistance with the introduction of grid segmentations and uneven features of busbars, an empirical comprehensive grid model was established and incorporated in the modeling. The modeled results showed that gridline and busbar segmentations are beneficial to efficiency enhancement and cost saving. However, gridline segmentation works only for segmentation of less than ~1.2 mm because of significant increase in emitter resistance for larger segmentation. It is worth mentioning that the grid segmentations have more improvement in the 5-BB cell than the 3-BB counterpart because of more segmented area with gridlines. Busbar segmentations, although work more effective than gridline segmentation, are restricted by the gridline spacing. In order to overcome the limitations with segmented busbars in solar cell design, the uneven busbars were introduced. It was found that the uneven busbars in conjunction with segmented gridlines have great potential to achieve ~20% efficiency Al-BSF solar cells without any additional cost.

CHAPTER 7: SUMMARY

The work presented in this thesis dealt with the fundamental understanding and implementation of front side metallization of Al back surface field (Al-BSF) silicon solar cell. Theoretical design and calculation of front metallization was first carried out, based on low power loss, to establish the achievable cell efficiency and then followed by experimental validation. The experimental data support the theoretical design and calculations and resulted in the highest average efficiency of ~19.8%, for a 5-BB cell, which is ~0.35% higher than the state-of-the-art 3-BB cell. This is the highest efficiency for a cost-effective industrial full Al-BSF silicon solar cell reported today.

Today, more than 90% of the installed solar modules are based on crystalline silicon, mono and multi combined. Of the >90% modules shipment, 48% was made from the conventional Al-BSF cells, 43% from the advanced structures which includes metal wrap through (MWT - 27%), passivated emitter rear contact (PERC - 10%), and interdigitated back contacts (IBC) and heterojunction intrinsic thin layer (HIT) - 6% [38]. Although the advanced cell structures with 43% market share is slightly more efficient than the Al-BSF, the added cost in processing and complexity overrides this improvement. Therefore, to maintain the low-cost and high-efficiency, it is important to implement simple processing steps to achieve cost-effective solar electricity. That is why this thesis focuses on the conventional cost-effective Al-BSF cell. The path to achieve cost-effective high-efficiency Al-BSF cell comprises (i) the design, and modeling of front metal electrodes including the

use of multi-busbar capable of decreasing the gridline resistance, (ii) the fine-line printing and (iii) the metal contact co-firing using optimized firing condition.

To better understand the limitations of screen-printed Al-BSF cell, various factors that affect the V_{oc}, J_{sc} and FF, as well as the conversion efficiency of a solar cell were identified. In addition to the advantages and disadvantages of this conventional technology, some alternative advanced solar cell technologies suitable for commercialization were also reviewed, which includes PERC, EWT, MWT, IBC, HIT, Triex Cell and Pluto Cell. However, none of these technologies fulfills the demands of cost-effective solar electricity due to the more expensive cell fabrication cost associated with the more complex solar cell architectures. Thus in this work the development of new concepts for the innovation of front metallization was based on the Al-BSF cell. A high-efficiency Al-BSF silicon solar cell usually requires (i) thick and uniform BSF at the back side of the cell, (ii) high minority carrier lifetime in the base, (iii) uniform emitter formation with good junction properties and optimal emitter sheet resistance, (iv) good front surface passivation and optimized anti-reflection coating layer, (v) low contact resistance and low gridline lateral conductance, (vi) low front metal shadowing, etc.

Uniform and thick BSF introduced by screen-printed full Al are the key features of a highly efficient Al-BSF cell. In order to understand the impact of Al BSF on solar cell performance, the relationship of BSF thickness, BSRV, V_{oc} and cell efficiency was evaluated by the PC1D device modeling to show the requirements on solar cell design. It was found that to achieve V_{oc} >638 mV and efficiency >19.3%, BSRV <200 cm/s and BSF thickness ≥6 μm are needed. To further understand the Al BSF, the Al particle morphology and printed thickness as well as the peak firing temperature were studied experimentally

by implementing different commercial Al pastes from different vendors. The effect of BSF was quantified by investigating the thickness and uniformity of Al BSF and BSRV. It was found that despite the variation in BSF thickness, similar cell performance with $V_{oc} \geq 635$ mV can be achieved provided that the BSF is uniform and greater than 5.49 μm.

After the back Al-BSF being optimized, the optimal emitter sheet resistance needs to be determined for the front side in pursuit of high efficiency solar cells. In the last few years, it is popular to use high sheet resistance emitter in solar cell design due to the enhanced blue response. However, for the Al-BSF cell, the high contact resistance and emitter resistance can result in high R_s without the use of selective emitter and narrower gridline spacing. To find out the optimal range of emitter sheet resistance in solar cell design for high conversion efficiency, a generalized calculation model was built to determine the number of gridlines required for a range of sheet resistance. The model is useful in determining optimum solar cell design including emitter sheet resistance and the number of gridlines that can achieve the highest efficiency. In order to better evaluate series resistance based on various metal grid designs, different grid models were implemented to evaluate the resistive losses. The one having the best match with the reference cell was incorporated in the simulation. It was found that for a typical 3-BB screen-printed silicon solar cell, the optimal emitter sheet resistance should be in the 70-90 Ω/□ range to achieve the best cell efficiency. Particularly, for sheet resistance of ~80 Ω/□, ~90 gridlines should be incorporated in the design of front electrode to strike for the best balance between emitter resistive loss and front metal shadowing loss.

With respect to the analysis of innovative front contact schemes, the total series resistance of a solar cell is a critical parameter for quantifying the electrical loss, while the

front shadowing loss is another important parameter for assessing the optical loss. The challenge is to find the optimal combination of busbars and gridlines in terms of their quantities and geometries to minimize the electrical and optical losses due to the front metal electrodes. To overcome the difficulties, a customized excel-based modeling program was implemented. Based on the variation in metal grid geometries and the number of busbars and gridlines, series resistance were calculated accordingly to determine the modeled I-V data and metallization cost. It was demonstrated that compared to the state-of-the-art 3-BB Al-BSF solar cell design, multi-busbar (number of busbars >3), particularly 5-BB cells have great potential to increase FF to ~0.81 and cell efficiency to ~20%. With more busbars incorporated in solar cell design, gridline resistance decreases due to the reduced effective gridline length. The metallization analysis shows that using more busbars in the solar cell design is also beneficial for cost saving. For the double-printed 5-BB solar cell, it is possible to implement the existing solar cell process and save ~33% of the printed silver paste compared with single-printing.

According to the guidelines for high-efficiency Al-BSF cell suggested by computer modeling, the benefits of multi-busbar and fine-line printed metal gridlines were validated experimentally using industrially feasible fabrication process. This was done first by the design and fabrication of the screen with some screen manufacturer (e.g. Sefar, etc.), and then printing metal pastes on both the front and back side of the commercial wafers with emitter and antireflection coating, and last co-firing the cells to make metal electrodes for I-V measurements. In the experiments, cells with conventional 3-BB design are compared with those with 4- and 5-BB designs. All the Al-BSF silicon solar cells were fabricated on p-type Czochralski (CZ) monocrystalline silicon substrates having resistivity of 2.0 Ω-cm,

thickness of 180 μm and size of 239 cm^2, and $POCl_3$ diffused emitter with sheet resistance of ~80 Ω/□. The gridline width of 50-60 μm was achieved by a screen with 40 μm mesh opening. After the screen-printed metal electrodes being dried, all the solar cells were co-fired on an IR-belt furnace with belt speed of 230 IPM at peak firing temperature of ~800 °C. It was demonstrated that the multi-busbar (4- and 5-BB) silicon solar cell designs enhance fill factor and hence efficiency. By implementing the same total busbar width, the solar cell performance can be enhanced with 4- and 5-BB metal grid designs without any additional cost. Based on the measured I-V data for all experimental cells, solar cell efficiency can be increased by $0.41\%_{absolute}$ when the number of busbars increases from three to four, and $0.66\%_{absolute}$ from three to five. And 5-BB cell have great potential to reach ~20% efficiency with further improvement in front electrode design.

To further improve solar cell conversion efficiency, some promising front grid metallization patterns with the introduction of grid segmentation and uneven busbar were also investigated to find the path to achieve >20% efficiency for the Al-BSF cell. To accurately assess the impact of the segmentation of gridlines and busbars, as well as uneven busbars, a comprehensive empirical grid model was first established. This was followed by investigation of (i) the effect of segmented gridlines on efficiency for a three and five uniform busbar cells; (ii) the effect of segmented bus bars and gridlines on efficiency for a three and five uniform busbar cells; and (iii) the effect of uneven bus bars in conjunction with the segmented gridlines on efficiency for the three and five busbar cells. Each of these scenarios was investigated theoretically with modeling to evaluate the impact on cell performance. The cost benefits for each of the scenarios were also taken into account. The modeled results showed that gridline and busbar segmentations are beneficial for efficiency

enhancement and cost saving. However, gridline segmentation works only for segmentation of less than ~1.2 mm because of significant increase in emitter resistance for larger segmentation. It is worth mentioning that the grid segmentations have more improvement in the 5-BB cell than the 3-BB counterpart because of more segmented area with gridlines. Busbar segmentations, although work more effective than gridline segmentation, are restricted by the gridline spacing. In order to overcome the limitations with segmented busbars in solar cell design, the uneven busbars were implemented. It was found that the uneven busbars in conjunction with segmented gridlines have great potential to achieve >20% efficiency Al-BSF solar cells.

Future Work

For the future work, it is necessary to experimentally validate the effect of gridline segmentation and uneven busbars introduced to the front electrode design as demonstrated in Chapter 6 to achieve Al-BSF cell with >20% conversion efficiency. Additionally, busbar width of 1.0-1.2 mm should be used in the 3-BB design to minimize optical and electrical losses. And fine-line printing with of <40 μm (e.g. 30 μm) mesh opening should be implemented to achieve higher resolution printing, which would contribute to higher J_{sc} and lower R_s compared to what has been achieved. Also, it would be interesting to take advantage of the benefit of 5-BB in the metallization of PERC cell to achieve >22.5% conversion efficiency.

REFERENCES

[1] A. Ebong, A. Upadhyaya, J. Kean, B. C. Rounsaville, I. B. Cooper, V. Upadhyaya, A. Kapoor, A. Rohatgi, D. C. Tamboli, A. Wu, and M. B. Rao. "Effect of surface cleaning on pyramid size of randomly textured mono crystalline silicon and the impact on solar cell efficiency." *Con. Proc., 37th IEEE PVSC*, Austin-Texas, 2011, pp.1046-1049.

[2] A. Ebong, and N. Chen. "Metallization of crystalline silicon solar cells: A review." *High Capacity Optical Networks and Enabling Technologies (HONET), 2012 9th International Conference on*, pp. 102-109, IEEE, 2012.

[3] A. W.Blakers , A. Wang, A. M. Milne, J. Zhao, and M. A. Green. "22.8% efficient silicon solar cell." *Applied Physics Letters* 55, no. 13 (1989): 1363-1365.

[4] M. A. Green, et al. "Characterization of 23-percent efficient silicon solar cells." IEEE Transactions on Electron Devices, 37.2 (1990): 331-336.

[5] R. N. Hall, and T. J. Soltys. "Polka dot solar cell." *In 14th Photovoltaic Specialists Conference*, vol. 1, pp. 550-553. 1980.

[6] J. M. Gee, W. K. Schubert, and P. A. Basore. "Emitter wrap-through solar cell." *Conference Record of the 23rd Photovoltaic Specialists Conference*, IEEE, 1993.

[7] W. Neu, A. Kress, W. Jooss, P. Fath, and E. Bucher. "Low-cost multicrystalline back-contact silicon solar cells with screen printed metallization." *Solar energy materials and solar cells*, 74.1 (2002): 139-146.

[8] S. K. Chunduri, "PV production pathways to 61 euro cents per W module costs in 2 years", *presented at PHOTON's 6th PV Production Equipment Conference (c-Si)*, Berlin, Germany, April 2011.

[9] D. H. Jang, J. H. Ko, J. W. Kang, J. H. Kim, and J. W. Jeong. "Effect of series resistance on metal-wrap-through multi-crystalline silicon solar cells." *Solar Energy Materials and Solar Cells*, 95.1 (2011): 53-55.

[10] Dirk-Holger Neuhaus, and Adolf Münzer. "Industrial silicon wafer solar cells." *Advances in OptoElectronics*, 2007 (2008).

[11] T. Saga. "Advances in crystalline silicon solar cell technology for industrial mass production." *NPG Asia Materials*, 2.3 (2010): 96-102.

[12] B. Thaidigsmann, A. Drews, T. Fellmeth, P. Saint-Cast, A. Wolf, F. Clement, R. Preu, and D. Biro. "Synergistic effects of rear-surface passivation and the metal wrap through concept." *IEEE Journal of Photovoltaics*, 2.2 (2012): 109-113.

[13] D. Biro, B. Thaidigsmann, F. Clement, A. Wolf, E. Lohmüller, S. Mack, T. Fellmeth, A. Drews, A. Spribille, E. A. Wotke, F. Lottspeich, M. Hofmann, U. Jäger, and R. Preu. "MWT meets PERC: Towards 20% efficient industrial silicon solar cells." *The 37th IEEE Photovoltaic Specialists Conference (PVSC)*, 2011.

[14] M. D. Lammert, and R. J. Schwartz. "The interdigitated back contact solar cell: a silicon solar cell for use in concentrated sunlight." *IEEE Translations on Electron Devices*, vol. 24, no. 4, pp. 337–342, 1977.

[15] P. J. Verlinden, M. Aleman, N. Posthuma, J. Fernandez, B. Pawlak, J. Robbelein, M. Debucquoy, K. V. Wichelen, and J. Poortmans. "Simple power-loss analysis method for high-efficiency Interdigitated Back Contact (IBC) silicon solar cells." *Solar Energy Materials and Solar Cells*, 106 (2012): 37-41.

[16] E. V. Kerschaver, and G. Beaucarne. "Back‐contact solar cells: A review." *Progress in Photovoltaics: Research and Applications*, 14, no. 2 (2006): 107-123.

[17] Green, Martin A. *Silicon solar cells: advanced principles & practice*. Centre for photovoltaic devices and systems, University of New South Wales, 1995.

[18] P. J. Cousins, D. D. Smith, H. C. Luan, J. Manning, T. D. Dennis, A. Waldhauer, K. E. Wilson, G. Harley, and W. P. Mulligan. "Generation 3: Improved performance at lower cost." *The 35th IEEE Photovoltaic Specialists Conference (PVSC)*, 2010.

[19] D. Swanson, "The Role of Modeling in SunPower's Commercialization Efforts", *presented at Challenges in PV Science, Technology, and Manufacturing: A workshop on the role of theory, modeling, and simulation*, Purdue University, August 2-3, 2012.

[20] M. Taguchi, M. Tanaka, T. Matsuyama, T. Matsuoka, S. Tsuda, S. Nakano, Y. Kishi, and Y. Kuwano. "Improvement of the conversion efficiency of polycrystalline silicon thin film solar cell." *In Proc. 5th PVSEC*, pp. 689-692. 1990.

[21] M. Tanaka, et al. "Development of New a-Si/c-Si Heterojunction Solar Cells: ACJ-HIT (Artificially Constructed Junction-Heterojunction with Intrinsic Thin-Layer)", *Jpn. J. Appl. Phys.*, 31,1992, pp.3518-3522.

[22] M. Tanaka, M. Taguchi, T. Takahama, T. Sawada, S. Kuroda, T. Matsuyama, S. Tsuda, A. Takeoka, S. Nakano, H. Hanafusa, and Y. Kuwano. "Development of a new heterojunction structure (ACJ-HIT) and its application to polycrystalline silicon solar cells." *Progress in Photovoltaics: Research and Applications* 1, no. 2 (1993): 85-92.

[23] Panasonic, Panasonic HIT. "Solar Cell Achieves World's Highest Energy Conversion Efficiency of 25.6% at Research Level." Press release (2014).

[24] S. Taira, Y. Yoshimine, A. Terakawa, E. Maruyama, and M. Tanaka. "Temperature properties of high-Voc HIT solar cells." *Renewable energy* (2006): 115-118.

[25] T. Kinoshita, D. Fujishima, A. Yano, A. Ogane, S. Tohoda, K. Matsuyama, Y. Nakamura, et al. "The approaches for high efficiency HIT solar cell with very thin (< 100 μm) silicon wafer over 23%." *The 26th EUPVSC Proceedings* (2011): 871-874.

[26] Jan. Schmidt, "Light-induced degradation in crystalline silicon solar cells." *Solid State Phenomena*, 95 (2003): 187-196.

[27] M. Taguchi, H. Sakata, Y. Yoshimine, E. Maruyama, A. Terakawa, M. Tanaka, and S. Kiyama. "An approach for the higher efficiency in the HIT cells." *Conference Record of the 31st IEEE Photovoltaic Specialists Conference*, 2005.

[28] E. Maruyama, A. Terakawa, M. Taguchi, Y. Yoshimine, D. Ide, T. Baba, M. Shima, H. Sakata, and M. Tanaka. "Sanyo's challenges to the development of high-efficiency HIT solar cells and the expansion of HIT business.", *Conference Record of the 2006 IEEE 4th WCPEC*. Vol. 2. IEEE, 2006.

[29] R. B. Godfrey, and M. A. Green. "655 mV open−circuit voltage, 17.6% efficient silicon MIS solar cells." *Applied physics letters*, 34.11 (1979): 790-793.

[30] R. B. Godfrey, and M. A. Green, "A 15% efficient silicon MIS solar cell," *Applied Physics Letters*, 33.7 (1978): 637-639.

[31] pv-tech.org/editors_blog/is_silevo_the_next_sunpower

[32] silevosolar.com

[33] J. Zhao, A. Wang, and M. A. Green. "24.5% E ciency Silicon PERT Cells on MCZ Substrates and 24.7% Efficiency PERL Cells on FZ Substrates." *Prog. Photovolt: Res. Appl* 7.471 (1999): 144.

[34] Z. Wang, P. Han, H. Lu, H. Qian, L. Chen, Q. Meng, N. Tang, F. Gao, Y. Jiang, J. Wu, W. Wu, H. Zhu, J. Ji, Z. Shi, A. Sugianto, L. Mai, B. Hallam, and S. Wenham. "Advanced PERC and PERL production cells with 20.3% record efficiency for standard commercial p−type silicon wafers." Progress in *Photovoltaics: Research and Applications* 20.3 (2012): 260-268.

[35] suntech-power.com/en/technology/technology/pluto

[36] "April 25, 1954: Bell Labs Demonstrates the First Practical Silicon Solar Cell". APS News (American Physical Society) 18 (4). April 2009.

[37] "The History of Solar". U.S. Department of Energy, Energy Efficiency and Renewable Energy.

[38] NPD Solarbuzz PV Equipment Quarterly (http://www.solarbuzz.com/news/recent-findings/multicrystalline-silicon-modules-dominate-solar-pv-industry-2014).

[39] European Photovoltaic Industry Association (EPIA), "Global Market Outlook for Photovoltaics 2014-2018".

[40] The Core Writing Team of IPCC Synthesis Report, and R. K. Pachauri, and L. Meyer. "Climate Change 2014 Synthesis Report." IPCC Fifth Assessment Synthesis Report.

[41] B. Elliston, I. MacGill, and M. Diesendorf. "Grid parity: A potentially misleading concept." *In Proc. Solar*, pp. 1-11. 2010.

[42] C. Breyer, and A. Gerlach. "Global overview on grid‐parity." *Progress in photovoltaics: Research and applications*, 21.1 (2013): 121-136.

[43] A. Goodrich, P. Hacke, Q. Wang, B. Sopori, R. Margolis, T. L. James, and M. Woodhouse. "A wafer-based monocrystalline silicon photovoltaics road map: Utilizing known technology improvement opportunities for further reductions in manufacturing costs." *Solar Energy Materials and Solar Cells*, 114 (2013): 110-135.

[44] eu-solar.panasonic.net/en/products/n-240-n-245/

[45] Shreesh Narasimha, Ajeet Rohatgi and A. W. Weeber, "An Optimized Rapid Aluminum Back Surface Field Technique for Silicon Solar Cells", *IEEE Transactions on Electron Devices*, Vol. 46, No. 7, July 1999.

[46] James A. Amick, Frank J. Bottari and Jack I. Hanoka, "The Effect of Aluminum Thickness on Solar Cell Performance", *J. Electrochem. Soc.*, Vol. 141, No. 6, June 1994.

[47] Michael Rauer, Christian Schmiga, Jonas Krause, Robert Woehl, Martin Hermle and Stefan W. Glunz, "Further Analysis of Aluminum Alloying for the Formation of p^+ Regions in Silicon Solar Cells", *Energy Procedia*, 8 (2011), 200-206.

[48] Vishal Mehta, Bhushan Sopori, Robert Reedy, Bobby To, Helio Moutinho and N. M. Ravindra, "Screen-Printed Al Back Contacts on Si Solar Cells: Issues and Some Solutions", *Mater. Res. Soc. Symp. Proc.*, Vol. 1210.

[49] W. Shockley, and W. T. Read Jr. "Statistics of the recombinations of holes and electrons." *Physical Review* 87.5 (1952): 835.

[50] V. Meemongkolkiat, K. Nakayashiki, D. S. Kim, R. Kopecek and A. Rohatgi, "Factors Limiting the Formation of Uniform and Thick Aluminum- Back-Surface Field and Its Potential", *J. Electrochem. Soc.*, 153 (1), G53-G58 (2006).

[51] J. Krause, R. Woehl, M. Rauer, C. Schmiga, J. Wilde and D. Biro, “Microstructural and Electrical Properties of Different-sized Aluminum- alloyed Contacts and Their Layer System on Silicon Surfaces”, *Solar Energy Materials & Solar Cells*, 95 (2011), 2151-2160.

[52] X. Gu, X. Yu, J. Xu, R. Fan and D. Yang. "Towards thinner and low bowing silicon solar cells: form the boron and aluminum co‐doped back surface field with thinner metallization film." *Prog. Photovolt: Res. Appl*, 21.4 (2013): 456-461.

[53] J. del Alamo, J. Eguren, A. Luque, “Operating limits of Al- alloyed high-low junctions for BSF solar cells”, *Solid-State Electronics*, 24 (1981) 415-468.

[54] D. Clugston, and P. A. Basore. "PC1D version 5: 32-bit solar cell modeling on personal computers." *Conference Record of the 26th IEEE Photovoltaic Specialists Conference*, pp. 207-210, 1997.

[55] P. A. Basore, “Extended spectral analysis of internal quantum efficiency”, *Proceedings of the 23rd IEEE Photovoltaic Specialists Conference*, Louisville, KY, 1993, pp. 147-152.

[56] Paul A. Basore and Kirsten Cabanas-Holmen, “PC2D: A Circular-Reference Spreadsheet Solar Cell Device Simulator”, *IEEE Journal of Photovoltaics*, Vol. 1, No. 1, July 2011.

[57] D. L. Meier, and D. K. Schroder. "Contact resistance: its measurement and relative importance to power loss in a solar cell." *IEEE Trans. Electron Devices* on 31, (1984) 647.

[58] A. Safiei, H. Windgassen, K. Wolter, and H. Kurz. "Emitter profile tailoring to contact homogeneous high sheet resistance emitter." *Energy Procedia*, 27, (2012) 432.

[59] G. Kulushich, B. Bazer-Bachi, T. Takahashi, H. Iida, R. Zapf-Gottwick, and J. H. Werner. "Contact Formation on 100 Ω/sq Emitter by Screen Printed Silver Paste." *Energy Procedia*, 27, (2012) 485.

[60] A. Ebong, I. B. Cooper, B. C. Rounsaville, F. Zimbardi, A. Upadhyaya, A. Rohatgi, W. Borland, K. Mikeska, and A. Carroll. "Formation of high quality screen-printed contacts to homogeneous high sheet resistance emitters (HHSE).” *Proc. 37th IEEE Photovoltaic Spec. Conf.*, 2013, p. 2157.

[61] A. Ebong, I. B. Cooper, A. Rounsaville, A. Rohatgi, W. Borland, and K. Mikeska. "Overcoming the technological challenges of contacting homogeneous high sheet resistance emitters (HHSE)." *Proc. 26th EU PVSEC*, 2011, p. 1747.

[62] M. M. Hilali, K. Nakayashiki, A. Ebong, and A. Rohatgi. "High‐efficiency (19%) screen‐printed textured cells on low‐resistivity float‐zone silicon with high sheet‐resistance emitters." *Prog. Photovoltaics* 14, (2006) 135.

[63] A. Ebong, I. B. Cooper, B. C. Rounsaville, A. Rohatgi, M. Dovrat, E. Kritchman, D. Brusilovsky, and A. Benichou. "Capitalizing on the Glass-Etching Effect of Silver Plating Chemistry to Contact Si Solar Cells With Homogeneous 100-110 Ω/sq Emitters." *IEEE Electron Device Lett.* 32, (2011) 779.

[64] A. Ebong, I. B. Cooper, B. Rounsaville, K. Tate, A. Rohatgi, B. Bunkenburg, J. Cathey, S. Kim, and D. Ruf. "High efficiency inline diffused emitter (ILDE) solar cells on mono‐crystalline CZ silicon." *Prog. Photovoltaics* 18, (2010) 590.

[65] L. Jiang, W. Zhang, T. Guo, D. Kapp, Y. Li, and L. Wang. "An improved mathematical modeling to simulate metallization screen pattern trend for silicon solar cell." *Proc. 39th IEEE Photovoltaic Spec. Conf.*, 2013, p. 2641.

[66] L. J. Caballero, P. Sánchez-Friera, B. Lalaguna, J. Alonso, and M.A. Vázquez. "Series resistance modelling of industrial screen-printed monocrystalline silicon solar cells and modules including the effect of spot soldering." *Proc. 4th WCPEC, IEEE*, 2006, p. 1388.

[67] D. L. Meier, V. Chandrasekaran, A. Gupta, V. Yelundur, and A. Rohatgi. "Silver Contact Grid: Inferred Contact Resistivity and Cost Minimization in 19% Silicon Solar Cells." *IEEE J. Photovolt.* 3, (2013) 199.

[68] D. L. Meier, E. A. Good, R. A. Garcia, B. L. Bingham, S. Yamanaka, V. Chandrasekaran and C. Bucher. "Determining components of series resistance from measurements on a finished cell." *Proc. 4th WCPEC, IEEE*, 2006, p. 1315.

[69] A. Goetzberger, J. Knobloch and B. Voss. *Crystalline Silicon Solar Cells: Technology and System Applications* (John Wiley & Sons, Inc., April 1998) 1st ed., p. 105.

[70] G. Schubert, J. Horzel, R. Kopecek, F. Huster and P. Fath. "Silver thick film contact formation on lowly doped phosphorous emitters." *Proc. 20th EU PVSEC*, 2005, p. 934.

[71] G. Schubert, J. Horzel and S. Ohl. "Investigations on the mechanism behind the beneficial effect of a forming gas anneal on solar cells with silver thick film contacts." *Proc. 21st EU PVSEC*, 2006, p. 1460.

[72] M. M. Hilali, M. M. Al-Jassim, B. To, H. Moutinho, A. Rohatgi, and S. Asher. "Understanding the formation and temperature dependence of thick-film Ag contacts on high-sheet-resistance Si emitters for solar cells." *J. Electrochem. Soc.* 152, (2005) 742.

[73] M. M. Hilali, K. Nakayashiki, C. Khadilkar, R. C. Reedy, A. Rohatgi, A. Shaikh, S. Kim and S. Sridharan. "Effect of Ag particle size in thick-film Ag paste on the electrical and physical properties of screen printed contacts and silicon solar cells." *J. Electrochem. Soc.* 153, (2006) A5.

[74] M. M. Hilali, S. Sridharan, C. Khadilkar, A. Shaikh, A. Rohatgi, and S. Kim. "Effect of glass frit chemistry on the physical and electrical properties of thick-film Ag contacts for silicon solar cells." *J. Electron. Mater.* 35, (2006) 2041.

[75] S. M. Sze: *Physics of Semiconductor Devices* (Wiley, New York, 2007) 3rd ed., p. 95.

[76] Andreas Schenk, "Finite-temperature full random-phase approximation model of band gap narrowing for silicon device simulation." *J. Appl. Phys.*, 84, (1998) 3684.

[77] W. R. Thurber, R. L. Mattis, Y. M. Liu, and J. J. Filliben. "Resistivity−Dopant Density Relationship for Boron−Doped Silicon." *J. Electrochem. Soc.* 127, (1980) 2291.

[78] W. R. Thurber, R. L. Mattis, Y. M. Liu, and J. J. Fillibe. "Resistivity−dopant density relationship for phosphorus−doped silicon." *J. Electrochem. Soc.* 127, (1980) 1807.

[79] D. B. M. Klaassen, "A unified mobility model for device simulation - I. Model equations and concentration dependence." *Solid-State Electron.*, 35, (1992) 953.

[80] D. B. M. Klaassen, "A unified mobility model for device simulation - II. Temperature dependence of carrier mobility and lifetime." *Solid-State Electron*., 35, (1992) 961.

[81] Martin A. Green, *Solar cells: operating principles, technology, and system applications* (Prentice-Hall, Inc., New Jersey, 1982) 1st ed. p. 81.

[82] C. Bottosso, W. Tao, X. Wang, L. Ma, and M. Galiazzo. "Reliable Metallization Process for Ultra-Fine Line Printing." *Energy Procedia* 43 (2013): 80-85.

[83] A. Ebong, I. B. Cooper, K. Tate, B. Rounsaville, F. Zimbardi, V. Upadhyaya, A. Rohatgi, M. Dovrat, E. Kritchman, D. Brusilovsky, and A. Benichou. "Implementing narrow front silver gridlines through ink jet machine for high quality contacts to silicon solar cells." *Photovoltaic Specialists Conference (PVSC)*, 2011 37th IEEE. IEEE, 2011.

[84] A. Ebong, D. Gililov, L. Lavid, S. Krispil, S. Thygelbaum, M. Dovrat, Y. Wang, G. Jin, and T. Zhou. "Capitalising on the Precisions of Ion Implantation and Ink Jetted Fine Gridline to Create Low-Cost High Efficiency Silicon Solar Cells." *Energy Procedia* 33 (2013): 24-32.

[85] A. Ebong, V. Unsur, N. Chen, and A. Chowdhury. "Understanding the Sintering of Digital Inkjet Printed (DIP) Contacts to Achieve Low-contact Resistance on Silicon Solar Cells." *In 1st Africa Photovoltaic Solar Energy Conference and Exhibition Proceedings*, vol. 1, no. 1, pp. pp-1. 2014.

[86] Y. Yang, P. P. Altermatt, W. Zhu, X. Liang, and H. Shen. "Analysis of industrial c-Si solar cell's front metallization by advanced numerical simulation." *Progress in Photovoltaics: Research and Applications* 20, no. 4 (2012): 490-500.

[87] Yong Sheng Khoo, Timothy M. Walsh, and Armin G. Aberle. "Optimizing the Front Electrode of Silicon-Wafer-Based Solar Cells and Modules." *Photovoltaics, IEEE Journal of* 3, no. 2 (2013): 716-722.

[88] A. R. Burgers, "How to design optimal metallization patterns for solar cells." *Progress in Photovoltaics Research and Applications* 7.6 (1999): 457-461.

[89] Serreze, H. B. "Optimizing solar cell performance by simultaneous consideration of grid pattern design and interconnect configurations." *Conf. Record 13th. IEEE Photovoltaic Specialists Conf.* 1978.

[90] H. Hannebauer, et al. "Record low Ag paste consumption of 67.7 mg with dual print." *Energy Procedia* 43 (2013): 66-71.

[91] N. Chen, and A. Ebong. "Investigation of the Optimum Number of Busbars for Cost-effective Industrial Al-BSF Silicon Solar Cell." *24th Workshop on Crystalline Silicon Solar Cells & Modules: Materials and Processes*, July 27-30, 2014, Breckenridge, Colorado.

[92] N. Chen, A. Chowdury, E. Ahmad, V. Unsur, and A. Ebong. "Assessing the impact of multi-busbars on metallization cost and efficiency of solar cells with digital inkjet-printed gridlines," *High Capacity Optical Networks and Enabling Technologies (HONET-CNS)*, pp.60-65, 11-13 Dec. 2013.

[93] Mohamed M. Hilali, "Understanding and development of manufacturable screen-printed contacts on high sheet-resistance emitters for low-cost silicon solar cells." PhD thesis, Georgia Institute of Technology (2005).

[94] en.wikipedia.org/wiki/Screen_printing

[95] dupont.com/products-and-services/electronic-electrical-materials/articles/basics-of-screen-printing.html

[96] Gunnar Schubert, "Thick Film Metallisation of Crystalline Silicon Solar Cells." PhD thesis, Universität Konstanz, August, 2006.

[97] Won II Son, You-Jin Sim, Choong-Hoon Paik, and Mi-Kyoung Kim. "Glass frit, and conductive paste composition and solar cell comprising the same." U.S. Patent 20,150,007,880, issued January 8, 2015.

[98] Min-Seo Kim, and Soo-Yeon Heo. "Silver paste composition and solar cell using same. " EP Patent 2490228 A2, issued August 22, 2012.

[99] R.J.S. Young, A.F. Carroll, "Advances in front-side thick film metallisations for silicon solar cells", *in: Proceedings of the 16th European Photovoltaic Solar Energy Conference*, Glasgow, 2000, pp. 1731–1734.

[100] C. Ballif, D.M. Huljic, A. Hessler-Wyser, G. Willeke, "Nature of the Ag–Si interface in screen-printed contacts: a detailed transmission electron microscopy study of cross-sectional structures", *in: Proceedings of the 29th IEEE Photovoltaic Specialists Conference*, Glasgow, 2002, pp. 360–363.

[101] C. Ballif, D.M. Huljic, G. Willeke, A. Hessler-Wyser, "Silver thick-film contacts on highly doped n-type silicon emitters: structural and electronic properties of the interface", *Appl. Phys. Lett.* 82 (2003) 1878–1880.

[102] G. Schubert, F. Huster, P. Fath, "Formation and nature of Ag thick film front contacts on crystalline silicon solar cells", *in: Proceedings of the Photovoltaic in Europe Conference, Rome*, 2002, pp. 343–346.

[103] G. Schubert, F. Huster, P. Fath, "Current Transport mechanism in printed Ag thick film contacts to an n-type emitter of a crystalline silicon solar cell", *in: Proceedings of the 19th European Photovoltaic Solar Energy Conference*, Paris, 2004, pp. 813–816.

[104] G. Schubert, F. Huster, P. Fath, "Physical understanding of printed thickfilm front contacts of crystalline Si solar cells — review of existing models and recent developments", *Sol. Energy Mater. Sol. Cells* 90 (2006) 3399–3406.

[105] M.M. Hilali, B. To, and A. Rohatgi, "A review and understanding of screen-printed contacts and selective-emitter formation", *in: Proceedings of the 14th Workshop on Crystalline Silicon Solar Cell Materials and Processes*, Winter Park, CO, 2004, pp. 109–116.

[106] J. Hoornstra, G. Schubert, K. Broek, F. Granek, C. LePrince, "Lead free metallisation paste for crystalline silicon solar cells: from model to results", *in: Proceedings of the 31st IEEE Photovoltaic Specialists Conference*, Orlando, FL, 2005, pp. 1293–1296.

[107] K. K. Hong, S. B. Cho, J. S. You, J. W. Jeong, S. M. Bea, and J. Y. Huh, "Mechanism for the formation of Ag crystallites in the Ag thick-film contacts of crystalline Si solar cells." *Sol. Energy Mater. and Sol. Cells*, 93(6), (2009) 898-904.

[108] G.C. Cheek, R.P. Mertens, R. Van Overstraeten, L. Frisson, "Thick-film metallization for solar cell applications." *Electron Devices*, *IEEE Transactions on*, 31(5), (1984) 602-609.

[109] K. Firor, S.J. Hogan, J.M. Barret, R.T. Coyle, *in: Proceedings of the 16th IEEE PVSC*, San Diego, 1982, pp. 824–827.

[110] M. Prudenziati, L. Moro, B. Morten, F. Sirotti, and L. Sardi. "Ag-based thick-film front metallization of silicon solar cells." *Active and passive electronic components* 13, no. 3 (1989): 133-150.

[111] T. Nakajima, A. Kawakami, and A. Tada, "Ohmic Contact of Conductive Ag paste to Silicon Solar Cell", *International Journal of Hybrid Microelectronics*, vol.6, (1983) pp.580-586.

[112] E. Cabrera, S. Olibet, J. Glatz-Reichenbach, R. Kopecek, D. Reinke, and G. Schubert. "Current transport in thick film Ag metallization: Direct contacts at Silicon pyramid tips? " *Energy Procedia* 8 (2011): 540-545.

[113] Kang, M.-K., Yoo, Y.-S., Kim, D.-Y. and Hwang, N.-M., "Growth of BaTiO3 Seed Grains by the Twin-Plane Reentrant Edge Mechanism", *J. Am. Ceram. Soc.*, 83, 385–90, 2000.

[114] A. Fallisch and D. Biro, "2-D SPICE simulation and analytical calculation of spreading resistance effects in emitter wrap-through cells with nonsquare via-hole pattern." *Photovoltaics, IEEE Journal of* 1.2 (2011): 153-158.

[115] G. K. Reeves, and H. B. Harrison. "Obtaining the specific contact resistance from transmission line model measurements." *Electron Device Letters, IEEE* 3, no. 5 (1982): 111-113.

[116] D. K. Schroder, *Semiconductor Material and Device Characterization*, 3rd ed, June 2015, Wiley-IEEE Press.

PUBLICATIONS

[1] Nian Chen, A. Ebong and E. Addo, “Understanding and Quantifying the Impact of Al Pastes on Al Back Surface Field Screen-Printed Silicon Solar Cell”, *The 27th European Photovoltaic Solar Energy Conference and Exhibition*, September 24-28, 2012, Frankfurt, Germany.

[2] A. Ebong, and Nian Chen. "Metallization of crystalline silicon solar cells: A review." *In High Capacity Optical Networks and Enabling Technologies (HONET), 2012 9th International Conference on*, pp. 102-109. IEEE, 2012.

[3] Nian Chen, A. Chowdury, E. Ahmad, V. Unsur, and A. Ebong. "Assessing the impact of multi-busbars on metallization cost and efficiency of solar cells with digital inkjet-printed gridlines." *In High Capacity Optical Networks and Enabling Technologies (HONET-CNS), 2013 10th International Conference on*, pp. 60-65. IEEE, 2013.

[4] Nian Chen, and A. Ebong. "Investigation of the Optimum Number of Busbars for Cost-effective Industrial Al-BSF Silicon Solar Cell". 24th *Workshop on Crystalline Silicon Solar Cells & Modules: Materials and Processes*. Breckenridge, Colorado, July 27-30, 2014.

[5] A. Ebong, V. Unsur, Nian Chen, and A. Chowdhury. "Understanding the Sintering of Digital Inkjet Printed (DIP) Contacts to Achieve Low-contact Resistance on Silicon Solar Cells." *In 1st Africa Photovoltaic Solar Energy Conference and Exhibition Proceedings*, vol. 1, no. 1, pp. pp-1. 2014. (Keynote Session, invited)

[6] A. Ebong, and Nian Chen. "Understanding the uniqueness of the inkjet metallization of multicrystalline silicon solar cell." *in: Proceedings of The 6th World Conference on Photovoltaic Energy Conversion (WCPEC)*, 23-27th November 2014, Kyoto, Japan.

[7] Nian Chen, and A. Ebong. "Comprehensive Assessment of the p-n Junction Formation Technologies for Solar Cell Emitter Uniformity, Contact Formation and Performance." *in: Proceedings of The 6th World Conference on Photovoltaic Energy Conversion (WCPEC)*, 23-27th November 2014, Kyoto, Japan.

[8] Nian Chen, and A. Ebong. "Generalized Analysis of the Impact of Emitter Sheet Resistance on Silicon Solar Cell Performance." *in: Proceedings of The 6th World Conference on Photovoltaic Energy Conversion (WCPEC)*, 23-27th November 2014, Kyoto, Japan.

[9] Nian Chen, A. Chowdhury, and A. Ebong. "Comprehensive empirical model for evaluation of the series resistance of a solar cell." *In High-capacity Optical Networks and Emerging/Enabling Technologies (HONET), 2014 11th Annual*, pp. 214-218. IEEE, 2014.

[10] A. Ebong, Nian Chen, A. Chowdhury and V. Unsur. "The impact of rapid thermal processing (RTP) on crystalline silicon solar cell performance and light induced degradation (LID)." *in: Proceedings of The 42nd IEEE Photovoltaic Specialists Conference (PVSC)*, June 14-19, 2015, New Orleans, LA.

[11] Nian Chen, and A. Ebong. "Investigating the Benefits of Multi Bus-bars for Industrial Al-BSF Silicon Solar Cells." *in: Proceedings of The 42nd IEEE Photovoltaic Specialists Conference (PVSC)*, June 14-19, 2015, New Orleans, LA (Best Poster Award Winner).

[12] V. Unsur, A. Chowdhury, Nian Chen, and A. Ebong. "The Effects of Nano Ag Particles on Gridline Sintering for Silicon Solar Cells." *in: Proceedings of The 42nd IEEE Photovoltaic Specialists Conference (PVSC)*, June 14-19, 2015, New Orleans, LA (Best Poster Award).

[13] Nian Chen, and A. Ebong. "Generalized Analysis of the Impact of Emitter Sheet Resistance on Silicon Solar Cell Performance." *Jpn. J. Appl. Phys*. 54, 08KD20 (2015).

[14] Nian Chen, and A. Ebong. " Theoretical Investigation of the Impact of Gridline and Busbar Segmentation on Industrial Al-BSF Silicon Solar Cell Performance." 25th *Workshop on Crystalline Silicon Solar Cells & Modules: Materials and Processes*. Keystone, Colorado, July 26-29, 2015.

[15] A. Ebong, Nian Chen, V. Unsur and A. Chowdhury. "Understanding the impact of rapid thermal processing (RTP) on the light induced degradation (LID) of mono and multi crystalline silicon solar cells." *The 30th European Photovoltaic Solar Energy Conference and Exhibition*, September 14-18, 2015, Hamburg, Germany.

[16] Nian Chen, and A. Ebong. "Towards 20% efficient industrial Al-BSF silicon solar cell with multiple busbars and fine gridlines." Submitted to *Solar Energy Materials and Solar Cells* for publication.

INVITED TALK

[1] A. Ebong, and Nian Chen. **Invited talk**: “Solar Cell Technologies and Challenges to Commercialization.” *Global Photovoltaic Conference (GPVC), International Symposium on Photovoltaics (ISP)*, November 10-11th, 2014, Busan, Korea.